NASA/TM-2008-215123

An Approach to Assess Delamination Propagation Simulation Capabilities in Commercial Finite Element Codes

Ronald Krueger
National Institute of Aerospace, Hampton, Virginia

April 2008

The NASA STI Program Office . . . in Profile

Since its founding, NASA has been dedicated to the advancement of aeronautics and space science. The NASA Scientific and Technical Information (STI) Program Office plays a key part in helping NASA maintain this important role.

The NASA STI Program Office is operated by Langley Research Center, the lead center for NASA's scientific and technical information. The NASA STI Program Office provides access to the NASA STI Database, the largest collection of aeronautical and space science STI in the world. The Program Office is also NASA's institutional mechanism for disseminating the results of its research and development activities. These results are published by NASA in the NASA STI Report Series, which includes the following report types:

- TECHNICAL PUBLICATION. Reports of completed research or a major significant phase of research that present the results of NASA programs and include extensive data or theoretical analysis. Includes compilations of significant scientific and technical data and information deemed to be of continuing reference value. NASA counterpart of peer-reviewed formal professional papers, but having less stringent limitations on manuscript length and extent of graphic presentations.

- TECHNICAL MEMORANDUM. Scientific and technical findings that are preliminary or of specialized interest, e.g., quick release reports, working papers, and bibliographies that contain minimal annotation. Does not contain extensive analysis.

- CONTRACTOR REPORT. Scientific and technical findings by NASA-sponsored contractors and grantees.

- CONFERENCE PUBLICATION. Collected papers from scientific and technical conferences, symposia, seminars, or other meetings sponsored or co-sponsored by NASA.

- SPECIAL PUBLICATION. Scientific, technical, or historical information from NASA programs, projects, and missions, often concerned with subjects having substantial public interest.

- TECHNICAL TRANSLATION. English-language translations of foreign scientific and technical material pertinent to NASA's mission.

Specialized services that complement the STI Program Office's diverse offerings include creating custom thesauri, building customized databases, organizing and publishing research results ... even providing videos.

For more information about the NASA STI Program Office, see the following:

- Access the NASA STI Program Home Page at ***http://www.sti.nasa.gov***

- E-mail your question via the Internet to help@sti.nasa.gov

- Fax your question to the NASA STI Help Desk at (301) 621-0134

- Phone the NASA STI Help Desk at (301) 621-0390

- Write to:
  NASA STI Help Desk
  NASA Center for AeroSpace Information
  7115 Standard Drive
  Hanover, MD 21076-1320

NASA/TM-2008-215123

An Approach to Assess Delamination Propagation Simulation Capabilities in Commercial Finite Element Codes

Ronald Krueger
National Institute of Aerospace, Hampton, Virginia

National Aeronautics and
Space Administration

Langley Research Center
Hampton, Virginia 23681-2199

April 2008

Available from:

NASA Center for AeroSpace Information (CASI)
7115 Standard Drive
Hanover, MD 21076-1320
(301) 621-0390

National Technical Information Service (NTIS)
5285 Port Royal Road
Springfield, VA 22161-2171
(703) 605-6000

AN APPROACH TO ASSESS DELAMINATION PROPAGATION SIMULATION CAPABILITIES IN COMMERCIAL FINITE ELEMENT CODES

Ronald Krueger[1]

ABSTRACT

An approach for assessing the delamination propagation simulation capabilities in commercial finite element codes is presented and demonstrated. For this investigation, the Double Cantilever Beam (DCB) specimen and the Single Leg Bending (SLB) specimen were chosen for full three-dimensional finite element simulations. First, benchmark results were created for both specimens. Second, starting from an initially straight front, the delamination was allowed to propagate. The load-displacement relationship and the total strain energy obtained from the propagation analysis results and the benchmark results were compared and good agreements could be achieved by selecting the appropriate input parameters. Selecting the appropriate input parameters, however, was not straightforward and often required an iterative procedure. Qualitatively, the delamination front computed for the DCB specimen did not take the shape of a curved front as expected. However, the analysis of the SLB specimen yielded a curved front as was expected from the distribution of the energy release rate and the failure index across the width of the specimen. Overall, the results are encouraging but further assessment on a structural level is required.

1. INTRODUCTION

One of the most common failure modes for composite structures is delamination [1-4]. The remote loadings applied to composite components are typically resolved into interlaminar tension and shear stresses at discontinuities that create mixed-mode I, II and III delaminations. To characterize the onset and propagation of these delaminations, the use of fracture mechanics has become common practice over the past two decades [1, 5, 6]. The total strain energy release rate, G_T, the mode I component due to interlaminar tension, G_I, the mode II component due to interlaminar sliding shear, G_{II}, and the mode III component, G_{III}, due to interlaminar scissoring shear, as shown in Figure 1, need to be calculated. In order to predict delamination onset or propagation for two-dimensional problems, these calculated G components are compared to interlaminar fracture toughness properties measured over a range from pure mode I loading to pure mode II loading [7-9]. A quasi static mixed-mode fracture criterion is determined by plotting the interlaminar fracture toughness, G_c , versus the mixed-mode ratio, G_{II}/G_T, determined from data generated using pure mode I Double Cantilever Beam (DCB) (G_{II}/G_T=0), pure mode II End-Notched Flexure (ENF) (G_{II}/G_T=1), and Mixed-Mode Bending (MMB) tests of varying ratios, as shown in Figure 2a for T300/914C and Figure 2b for C12K/R6376 [10, 11]. A curve fit of these data is performed to determine a mathematical relationship between G_c and G_{II}/G_T. [12, 13]. Failure is expected when, for a given mixed-mode ratio G_{II}/G_T, the calculated total energy release rate, G_T, exceeds the interlaminar fracture toughness, G_c. An interaction criterion incorporating the scissoring shear (mode III), was recently proposed by Reeder [14]. The edge-cracked torsion test (ECT) to measure G_{IIIc} is being considered for standardization [15, 16].

[1] National Institute of Aerospace (NIA), 100 Exploration Way, Hampton, VA 23666, resident at Durability, Damage Tolerance and Reliability Branch, NASA Langley Research Center, MS 188E, Hampton, VA, 23681.

The virtual crack closure technique (VCCT) is widely used for computing energy release rates based on results from continuum (2D) and solid (3D) finite element analyses and to supply the mode separation required when using the mixed-mode fracture criterion [17, 18]. The virtual crack closure technique has been used mainly by scientists in universities, research institutions and government laboratories and is usually implemented in their own specialized codes or used in post-processing routines in conjunction with general purpose finite element codes. An increased interest in using a fracture mechanics based approach to assess the damage tolerance of composite structures in the design phase and during certification has also renewed the interest in the virtual crack closure technique. The VCCT technique was recently implemented into the commercial finite element codes ABAQUS®[1], NASTRAN®[2] and Marc™[3] [19-21]. The implementation into the commercial finite element code SAMCEF™[4] [22] is a mix of VCCT and the Virtual Crack Extension Method suggested by Parks [23]. As new approaches for analyzing composite delamination are incorporated in finite element codes, the need for comparison and benchmarking becomes important.

The objective of this study was to create an approach, independent of the analysis software used, which allows the assessment of delamination propagation simulation capabilities in commercial finite element codes. For this investigation, the Double Cantilever Beam (DCB) specimen with a unidirectional and a multi-directional layup and the Single Leg Bending (SLB) specimen with a multi-directional layup (as shown in Figure 3) were chosen for full three-dimensional finite element simulations. These specimen configurations were chosen, since they are simple and a number of combined experimental and numerical studies had been performed previously where the critical strain energy release rates were evaluated [24-27]. To avoid unnecessary complications, experimental anomalies such as fiber bridging were not addressed. Comparisons with test results will follow later in another report. First, benchmark results were created using models simulating specimens with different delamination lengths. For each delamination length modeled, the load and displacement at the load point were monitored. The mixed-mode strain energy release rate components were calculated along the delamination front across the width of the specimen. A failure index was calculated by correlating the results with the mixed-mode failure criterion of the graphite/epoxy material. It was assumed that the delamination propagated when the failure index reached unity. Thus, critical loads and critical displacements for delamination onset were calculated for each delamination length modeled. These critical load/displacement results were used as a benchmark. The computed total strain energy was also used as a benchmark. Second, starting from an initially straight front, the delamination was allowed to propagate based on the algorithms implemented into the commercial finite element software. The approach was demonstrated for the commercial finite element code ABAQUS® with focus on their implementation of the Virtual Crack Closure Technique (VCCT) [19]. VCCT control parameters were varied to study the effect on the computed load-displacement behavior during propagation. It was assumed that the computed load-displacement relationship should closely match the benchmark results established earlier. As a qualitative assessment, the shape of the computed delamination fronts was also compared to photographs of failed specimens.

[1] ABAQUS® is manufactured by Dassault Systèmes Simulia Corp. (DSS), Providence, RI, USA
[2] NASTRAN® is a registered trademark of NASA and manufactured by MSC.Software Corp., Santa Ana, CA, USA
[3] Marc™ and Mentat™ are manufactured by MSC.Software Corp., Santa Ana, CA, USA
[4] SAMCEF™ is manufactured by Samtech, Liège, Belgium

2. SPECIMEN DESCRIPTION

For the current numerical investigation, the Double Cantilever Beam (DCB) and the Single Leg Bending (SLB) specimens, as shown in Figure 3, were chosen. The DCB specimen is used to determine the mode I interlaminar fracture toughness, G_{IC} (G_{II}/G_T=0) [7]. The SLB specimen was introduced for the determination of fracture toughness as a function of mixed-mode I/II ratio [26, 28]. This test may be performed in a standard three-point-bending fixture such as that used for the ENF test. By varying the relative thickness of the delaminated regions (t_1 and t_2), a different mixed-mode ratio may be achieved. This type of specimen was chosen to study mode separation. Previously, a number of combined experimental and numerical studies of these specimens had been performed and the critical strain energy release rates were evaluated [24-27].

In general, mode I, mode II and mixed-mode tests are performed on unidirectionally reinforced laminates, which means that delamination propagation occurs at a [0/0] interface and crack propagation is parallel to the fibers. For the current study, a DCB specimen made of T300/1076 graphite/epoxy with a unidirectional layup, $[0]_{24}$, was modeled. Although this unidirectional layup is desired for standard test methods to generate fracture toughness data, delamination propagation between layers of the same orientation will rarely occur in real structures. Previously, combined experimental and numerical studies on specimens with multi-directional layups were performed where the critical strain energy release rates of various interfaces were evaluated under mode I, mode II and mixed-mode conditions [25, 26]. Therefore, a DCB-specimen made of C12K/R6376 graphite/epoxy with a multi-directional layup was selected. The stacking sequence $[\pm 30/0/\text{-}30/0/30/0_4/30/0/\text{-}30/0/\text{-}30/30/_{\uparrow}\text{-}30/30/0/30/0/\text{ -}30/0_4/\text{-}30/0/30/0/\pm 30]$ was designated D±30, where the arrow ($_{\uparrow}$) denotes the location of the delamination. Additionally, a SLB specimen with D±30 layup was also modeled. The material properties are given in Table I.

3. METHODOLOGY

3.1 Fracture Criteria

Linear elastic fracture mechanics has proven useful for characterizing the onset and propagation of delaminations in composite laminates [5, 6]. When using fracture mechanics, the total strain energy release rate, G_T, is calculated along the delamination front. The term, G_T, consists of three individual components, as shown in Figure 1. The first component, G_I, arises due to interlaminar tension. The second component, G_{II}, arises due to interlaminar sliding shear (shear stresses parallel to the plane of delamination and perpendicular to the delamination front). The third component, G_{III}, arises due to interlaminar scissoring shear (shear stresses parallel to the plane of delamination and parallel to the delamination front). The calculated G_I, G_{II}, and G_{III} components are then compared to interlaminar fracture toughness values in order to predict delamination onset and propagation. The interlaminar fracture toughness values are determined experimentally over a range of mode mixity from pure mode I loading to pure mode II loading [7-9].

A quasi static mixed-mode fracture criterion is determined by plotting the interlaminar fracture toughness, G_c, versus the mixed-mode ratio, G_{II}/G_T. The fracture criteria is generated experimentally using pure Mode I (G_{II}/G_T=0) Double Cantilever Beam (DCB) tests [7], pure Mode II (G_{II}/G_T=1) End-Notched Flexure (ENF) tests [9], and Mixed Mode Bending (MMB) tests of varying ratios of G_I and G_{II} [8]. Typical examples are presented in Figure 2 for T300/914C and C12K/R6376 carbon epoxy materials. A 2D fracture criterion was suggested by Benzeggah and Kenane [13] using a simple mathematical relationship between G_c and G_{II}/G_T

$$G_c = G_{Ic} + \left(G_{IIc} - G_{Ic}\right) \cdot \left(\frac{G_{II}}{G_T}\right)^{\eta}. \quad (1)$$

In this expression, G_{Ic} and G_{IIc} are the experimentally-determined fracture toughness data for mode I and II as shown in Figure 2. The factor η was determined by a curve fit using the Levenberg-Marquardt algorithm in KaleidaGraph™ graphing and data analysis software [29]. Fracture initiation is expected when, for a given mixed-mode ratio G_{II}/G_T, the calculated total energy release rate, G_T, exceeds the interlaminar fracture toughness, G_c and therefore the failure index G_T/G_c is equal or greater than unity

$$\frac{G_T}{G_c} \geq 1. \quad (2)$$

For three-dimensional analysis, which yields results for the scissoring mode G_{III}, a modified definition is introduced where G_S denotes the sum of the in-plane shearing components $G_{II}+G_{III}$ [30]. This modification becomes necessary if a mixed-mode failure criterion, which accounts for all three modes, is not available. For analyses where $G_{III}=0$, this definition is equal to the commonly used definition of the mixed-mode ratio, G_{II}/G_T mentioned above. To determine failure along the delamination front, the critical energy release rate G_c is calculated using equation (1) with $G_{II} = G_S$ at each point along the delamination front. Subsequently, the failure index G_T/G_c is determined as above. The modified interaction criterion is an integral part of the VCCT for ABAQUS® analysis software and may be selected by the user [19].

Recently, Reeder [14] suggested an interaction criterion that is based on the 2D fracture criterion suggested by Benzeggah and Kenane [13] but incorporates the mode III scissoring shear

$$G_c = G_{Ic} + \left(G_{IIc} - G_{Ic}\right) \cdot \left(\frac{G_{II} + G_{III}}{G_T}\right)^{\eta} + \left(G_{IIIc} - G_{IIc}\right) \cdot \frac{G_{III}}{G_{II} + G_{III}} \cdot \left(\frac{G_{II} + G_{III}}{G_T}\right)^{\eta} \quad (3)$$

which is also an integral part of the VCCT for ABAQUS® analysis software and may be selected by the user [19].

Although several specimens have been suggested for the measurement of the mode III interlaminar fracture toughness property [15, 31, 32] a standard does not yet exist. Currently, the edge-cracked torsion test (ECT) is being considered for standardization as a pure mode III test [15, 16].

3.2 Virtual Crack Closure Technique (VCCT)

3.2.1 Background

A variety of methods are used in the literature to compute the strain energy release rate based on results obtained from finite element analysis. For delaminations in laminated composite materials where the failure is highly dependent on the mixed-mode ratio (as shown in Figure 2), the virtual crack closure technique (VCCT) [17, 18] has been most widely used for computing energy release rates. VCCT calculations using continuum (2D) and solid (3D) finite element analyses provide the mode separation required when using the mixed-mode fracture criterion.

The mode I, and mode II components of the strain energy release rate, G_I, G_{II} are computed using VCCT as shown in Figure 4a for a 2D four-node element. The terms F'_{xi}, F'_{yi} are the forces at the crack tip at nodal point i and u'_ℓ , v'_ℓ and u'_{ℓ^*} , v'_{ℓ^*} are the displacements at the corresponding nodal points ℓ and ℓ^* behind the crack tip. Note that G_{III} is identical to zero in the 2D case. For geometrically nonlinear analysis where large deformations may occur, both forces and displacements obtained in the global coordinate system need to be transformed into a local coordinate system (x', y') which originates at the crack tip as shown in Figure 4a. The local crack tip system defines the tangential (x', or mode II) and normal (y', or mode I) coordinate directions at the crack tip in the deformed configuration. The extension to 3D is straight forward as shown in Figure 4b and the total energy release rate G_T is calculated from the individual mode components as $G_T = G_I + G_{II} + G_{III}$. For the two-dimensional case shown in Figure 4a, $G_{III} = 0$.

3.2.2 VCCT for ABAQUS®

Currently, VCCT for ABAQUS® is an add-on capability to ABAQUS®/Standard Versions 6.5, 6.6 and 6.7 that provides a specific implementation of the virtual crack closure technique within ABAQUS®. The implementation of VCCT enables ABAQUS® to solve delamination and debonding problems in composite materials. The implementation is compatible with all the features in ABAQUS® such as large-scale nonlinear, models of composite structures including continuum shells, composite materials, cohesive elements, buckling, and contact. The plane of delamination in three-dimensional analyses is modeled using the existing ABAQUS®/Standard crack propagation capability based on the contact pair capability [19]. Additional element definitions are not required, and the underlying finite element mesh and model does not have to be modified [19].

Beyond simple calculations of the mixed-mode strain energy release rates along the delamination front, which was studied previously [27], the implementation also offers a crack propagation capability in ABAQUS®. It is implied that the energy release rate at the crack tip is calculated at the end of a converged increment. Once the energy release rate exceeds the critical strain energy release rate (including the user-specified mixed-mode criteria as shown in Figure 2), the node at the crack tip is released in the following increment, which allows the crack to propagate. To avoid sudden loss of stability when the crack tip is propagated, the force at the crack tip before advance is released gradually during succeeding increments in such a way that the force is brought to zero no later than the time at which the next node along the crack path begins to open [19].

In addition to the mixed-mode fracture criterion, VCCT for ABAQUS® requires additional input for the propagation analysis. If a user specified release tolerance is exceeded in an increment $(G - G_c)/G_c >$ *release tolerance*, a cutback operation is performed which reduces the time increment. In the new smaller increment, the strain energy release rates are recalculated and compared to the user specified release tolerance. The cutback reduces the degree of overshoot and improves the accuracy of the local solution [19]. A release tolerance of 0.2 is suggested in the handbook [19].

To help overcome convergence issues during the propagation analysis, ABAQUS® provides:

- *contact stabilization* which is applied across only selected contact pairs and used to control the motion of two contact pairs while they approach each other in multi-body contact. The damping is applied when bonded contact pairs debond and move away from each other [19]
- *automatic or static stabilization* which is applied to the motion of the entire model and is commonly used in models that exhibit statically unstable behavior such as buckling [19]

- *viscous regularization* which is applied only to nodes on contact pairs that have just debonded. The viscous regularization damping causes the tangent stiffness matrix of the softening material to be positive for sufficiently small time increments. Viscous regularization damping in VCCT for ABAQUS® is similar to the viscous regularization damping provided for cohesive elements and the concrete material model in ABAQUS®/Standard [19].

Setting the value of the input parameters correctly is often an iterative procedure, which will be discussed later.

4. FINITE ELEMENT MODELING

Typical three-dimensional finite element models of Double Cantilever Beam (DCB) and Single Leg Bending (SLB) specimens are shown in Figures 5 to 10. Along the length, all models were divided into different sections with different mesh refinement. A refined mesh of length d=5 mm with 20 elements was used for the DCB specimen as shown in the detail of Figure 5a. This section length had been selected in previous studies [24, 27] and was also used during the current investigation. Across the width, the model was divided into a center section and a refined edge section, j, to capture local edge effects and steep gradients. These sections appear as dark areas in the full view of the specimen as shown in Figure 5a. The specimen was modeled with solid brick elements C3D8I which had yielded excellent results in a previous study [27]. The DCB specimen with unidirectional layup, $[0]_{24}$, was modeled with six elements through the specimen thickness ($2h$) as shown in the detail of Figure 5a. This model was used to calculate mode I energy release rates and create the benchmark results discussed later. For all the analyses performed, the nonlinear solution option in ABAQUS®/Standard was used. For propagation analyses using VCCT for ABAQUS®, the model with a uniform mesh across the width, as shown in Figure 5b, was used to avoid potential problems at the transition between the coarse and very fine mesh near the edges of the specimen.

For the analysis with VCCT for ABAQUS®, the plane of delamination was modeled as a discrete discontinuity in the center of the specimen. To create the discrete discontinuity, each model was created from separate meshes for the upper and lower part of the specimens with identical nodal point coordinates in the plane of delamination [19]. Two surfaces (top and bottom surface) were created on the meshes as shown in Figure 5. Additionally, a node set was created to identify the intact (bonded nodes) region. Two coarser meshes with a reduced number of elements in width and length directions were also generated as shown in Figures 6a and b.

Three models of the DCB specimen were generated with continuum shell elements SC8R as shown in Figures 7a to c. The continuum shell elements in ABAQUS® are used to model an entire three-dimensional body, unlike conventional shells which discretize a reference surface. The SC8R elements have displacement degrees of freedom only, use linear interpolation, and allow finite membrane deformation and large rotations and, therefore, are suitable for nonlinear geometric analysis. The continuum shell elements are based on first-order layer-wise composite theory and include the effects of transverse shear deformation and thickness change [33]. In the x-y plane, the models have the same fidelity as the models made of solid brick elements C3D8I shown in Figures 5b, 6a and 6b. In the z-direction, only one element was used to model the thickness of the specimen. These less refined models were used to study the effect on performance (CPU time), computed load/displacement behavior and delamination front shape in comparison with the more refined model discussed above.

For the DCB specimen with multi-directional layup, D±30, a model with a uniform mesh across the width was used as shown in Figure 8. The DCB specimen was modeled with solid brick elements C3D8I which had yielded excellent results in a previous study [27]. Two plies on each side of the delamination were modeled individually using one element for each ply as shown in the detail of Figure 8. Since the delamination occurs at an interface between materials with dissimilar properties, care must be exercised in interpreting the values for G_I and G_{II} obtained using the virtual crack closure technique. For interfacial delaminations between two differing orthotropic solids, the observed oscillatory singularity at the crack tip becomes an issue for small element lengths [34, 35]. Hence, a value of crack tip element length, Δa, was chosen (approximately three ply thicknesses) in the range over which the strain energy release rate components exhibit a reduced sensitivity to the value of Δa. The adjacent four plies were modeled by one element with material properties smeared using the rule of mixtures [36, 37]. Smearing appeared suitable to reduce the model size, however, it did not calculate the full A-B-D stiffness matrix contributions of the plies. The adjacent element extended over the four 0˚ plies. The six outermost plies were modeled by one element with smeared material properties.

For the SLB specimen with multi-directional layup, D±30, a model with a uniform mesh across the width was used as shown in Figure 9. The SLB specimen was modeled with solid brick elements C3D8I which had yielded excellent results in a previous study [27]. For modeling convenience, the upper and lower arms were modeled similar to the model of the DCB specimen. To model the test correctly, only the upper arm was supported in the analysis as shown in Figure 9. An additional mesh with a longer refined center section was generated as shown in Figure 10. The refined model was used to study the effect on computed load/displacement behavior and delamination front shape in comparison with the model discussed above.

5. ANALYSIS

First, models simulating specimens with different delamination lengths were analyzed. For each delamination length modeled, the load and displacement at the load point were monitored. The mixed-mode strain energy release rate components were calculated along the delamination front across the width of the specimen. A failure index was calculated by correlating the results with the mixed-mode failure criterion of the graphite/epoxy material. It was assumed that the delamination propagated when the failure index reached a value of unity. Thus, critical loads and critical displacements for delamination onset were calculated for each delamination length modeled. These critical load/displacement results were used as a benchmark. Second, starting from an initially straight front, the delamination was allowed to propagate based on the algorithm implemented into VCCT for ABAQUS®. Input parameters were varied to study the effect on the computed load-displacement behavior during propagation. It was assumed that the computed load-displacement relationship should closely match the benchmark results established earlier.

The total strain energy in the model was calculated from the computed load/displacement behavior. The results were compared with the values computed internally by ABAQUS®. The total strain energy was also compared to the damping energies associated with the different stabilization techniques in ABAQUS®. Input parameters were varied to study the ratio between the damping energies and the total strain energy. It was assumed that input parameters which produced results with the smallest damping energies corresponded to results which also matched the benchmark results best.

As a qualitative assessment, the shape of the computed delamination fronts were also compared to photographs of failed specimens.

5.1 Creating a Benchmark Solution for a DCB specimen with unidirectional layup

The computed mode I strain energy release rate values were plotted versus the normalized width, y/B, of the specimen as shown in Figure 11. The results were obtained from models shown in Figure 5a for seven different delamination lengths a. An opening displacement $\delta/2$=1.0 mm was applied to each arm of the model. Qualitatively, the mode I strain energy release rate is fairly constant in the center part of the specimen and drops progressively towards the edges. This distribution will cause the initial straight front to grow into a curved front as explained in detail in the literature [38-41]. As expected, the mode II and mode III strain energy release rates were computed to be nearly zero and hence are not shown. Computed mode I strain energy release rates decreased with increasing delamination length a.

The failure index G_T/G_c was computed based on a mode I fracture toughness G_{Ic}=170.3 J/m^2 for T300/914C (see Figure 2a). The failure index was plotted versus the normalized width, y/B, of the specimen as shown in Figure 12. For all delamination lengths modeled, except for a=40 mm, the failure index in the center of the specimen (y/B=0) is above unity ($G_T/G_c \geq 1$).

For all delamination lengths modeled, the reaction loads P at the location of the applied displacement were calculated and plotted versus the applied opening displacement $\delta/2$ as shown in Figure 13. The critical load, P_{crit}, when the failure index in the center of the specimen (y/B=0) reaches unity (G_T/G_c=1), can be calculated based on the relationship between load P and the energy release rate G [42].

$$G = \frac{P^2}{2} \cdot \frac{\partial C_P}{\partial A} \tag{4}$$

In equation (4), C_P is the compliance of the specimen and ∂A is the increase in surface area corresponding to an incremental increase in load or displacement at fracture. The critical load P_{crit} and critical displacement $\delta_{crit}/2$ were calculated for each delamination length modeled

$$\frac{G_T}{G_c} = \frac{P^2}{P_{crit}^2} \quad \Rightarrow \quad P_{crit} = P\sqrt{\frac{G_c}{G_T}}, \quad \delta_{crit} = \delta\sqrt{\frac{G_c}{G_T}} \tag{5}$$

and the results were included in the load/displacement plots as shown in Figure 14 (solid red circles). The results indicate that, with increasing delamination length, less load is required to extend the delamination. This means that the DCB specimen exhibits unstable delamination propagation under load control. Therefore, prescribed opening displacements $\delta/2$ were applied in the analysis instead of nodal point loads P to avoid problems with numerical stability of the analysis. It was assumed that the critical load/displacement results can be used as a benchmark. For the delamination propagation, therefore, the load/displacement results obtained from the model of a DCB specimen with an initially straight delamination of a=30 mm length should correspond to the critical load/displacement path (solid red line) in Figure 14.

5.2 Delamination Propagation in a DCB Specimen with Unidirectional Layup Using VCCT for ABAQUS®

5.2.1 Computed load/displacement behavior for different input parameters

The propagation analysis was performed in two steps using the model shown in Figure 5b for a delamination length 30 mm. In the first step, a prescribed displacement (δ/2= 0.74 mm) was applied in two increments which equaled nearly the critical tip opening (δ_{crit}/2= 0.75 mm) determined in the analysis above for a delamination length of a=30 mm. Dividing the first step into just two increments was possible, since the load-displacement behavior of the specimen up to failure was linear as shown in Figure 14. In the second step, the total prescribed displacement was increased (δ/2= 2.8 mm). Automatic incrementation was used with a small increment size at the beginning (10^{-4} of the total increment) and a very small minimum allowed increment (10^{-18} of the total increment) to reduce the risk of numerical instability and early termination of the analysis. The analysis was limited to 1000 increments. Initially, analyses were performed without stabilization or viscous regularization. Release tolerance values between 0.2 and 0.6 were used. Using these parameters, the analysis terminated early prior to advancing the delamination.

In Figures 15 to 20, the computed resultant force (load P) at the tip of the DCB specimen is plotted versus the applied crack tip opening (δ/2) for different input parameters which are listed in Table II. For the results shown, the analysis terminated when the 1000 increment limit set for the analysis was reached. Several analyses terminated early because of convergence problems. To overcome the convergence problems, the methods implemented in ABAQUS® were used individually to study the effects. For the results plotted in Figure 15, global stabilization was added to the analysis. For a stabilization factor of $2x10^{-5}$, the stiffness changed to almost infinity once the critical load was reached causing the load to increase sharply (plotted in blue). The load increased until a point was reached where the delamination propagation started and the load gradually decreased following a saw tooth curve with local rising and declining segments. The gradual load decrease followed the same trend as the benchmark curve (in grey) but is shifted toward higher loads. For a stabilization factor of $2x10^{-6}$ (in green), the same saw tooth pattern was observed but the average curve was in good agreement with the benchmark result. For a stabilization factor of $2x10^{-7}$ (in red), the average was lower than before but was in good agreement with the benchmark result until termination after 550 increments due to convergence problems. The results obtained for a stabilization factor of $2x10^{-8}$ (in black for a release tolerance of 0.2) were on top of the previous result. The rate of convergence appeared to be slower since only δ/2= 1.14 mm was applied for 1000 increments compared to δ/2= 1.24 mm for a stabilization factor of $2x10^{-6}$ and the same release tolerance (0.2). Changing the release tolerance also appeared to influence the convergence as shown in Table II. For a release tolerance of 0.02, the analysis terminated after 1000 increments for δ/2= 1.04 mm. For a release tolerance of 0.002, the analysis terminated due to convergence problems after 451 increments. Changing the release tolerance, however, appeared to have no effect on the overall load/displacement behavior or the magnitude of the saw tooth pattern.

An adaptive automatic stabilization scheme was implemented into ABAQUS® version 6.7 which does not require the input of a fixed stabilization factor mentioned above. The adaptive automatic stabilization scheme allows ABAQUS® to automatically increase the damping factor if required or reduce the value if the instabilities subside. The result obtained for adaptive automatic stabilization and a release tolerance value of 0.2 is plotted in Figure 16. Initially the computed load overshot the benchmark result. For increasing propagation, however, the average curve was in good agreement with the benchmark result.

The results obtained for the coarse meshes shown in Figures 6a (plotted in red) and 6b (plotted in blue) are shown in Figure 17. A stabilization factor of $2x10^{-8}$ and a release tolerance of 0.002 was used for the coarse meshes. One result obtained for the fine mesh with the same stabilization factor and a release tolerance of 0.2 (in black) was added to the plot as a reference result. Changing the mesh size significantly influenced the magnitude of the saw tooth pattern. Larger elements yielded an increased saw tooth in spite of the fact a release tolerance two orders of magnitude smaller than the reference result was chosen.

For the results plotted in Figure 18, contact stabilization was added to the analysis. For all combinations of stabilization factors and release tolerances, a saw tooth pattern was observed, where the peak values were in good agreement with the benchmark result. The saw tooth curve is slightly lower. Decreasing the stabilization factors appeared to cause a slower rate of convergence which is either seen by smaller $\delta/2$ for the same number of analysis increments or early termination of the analysis as shown in Table II. Changing the release tolerance also appeared to influence the convergence. However, it appeared to have no effect on the overall load/displacement behavior or the magnitude of the saw tooth pattern.

The results obtained for models made of continuum shell elements (shown in Figure 7) are shown in Figure 19. A stabilization factor of $1x10^{-7}$ and a release tolerance of 0.2 was used for the fine mesh where three continuum shell elements were used over the thickness of one arm as shown in Figure 5b (in green). The release tolerance was lowered to a value of 0.002 for the fine mesh shown in Figure 7a where only one element was used over the thickness of one arm (in black). The initial stiffness of the shell model is slightly reduced. The propagation results, however, are in good agreement. It seems that the element type used to model the specimen has no effect on the observed saw tooth behavior. A stabilization factor of $1x10^{-7}$ and a release tolerance of 0.2 were used for the models with coarser meshes. The results obtained for the models in Figure 7b (plotted in red) and 7c (plotted in blue) indicate that changing the mesh size, significantly influenced the magnitude of the saw tooth pattern. As observed before, larger elements yielded an increased saw tooth pattern.

Viscous regularization was added to the analysis to overcome convergence problems. Convergence could not be achieved over a wide range of viscosity coefficients when a release tolerance value of 0.2 was used as suggested in reference [19]. Subsequently, the release tolerance value was increased. The results where convergence was achieved are plotted in Figure 20. For all combinations of the viscosity coefficient and release tolerance, a saw tooth pattern was obtained, where the peak values were in good agreement with the benchmark result. The average results are somewhat lower than the benchmark result. Compared to results obtained from analyses with global and contact stabilization, the results obtained with viscous regularization appear to have a better rate of convergence since a higher opening displacement ($\delta/2$= 1.48 mm) was applied during the analysis for the same number of total increments (1000). Decreasing the viscosity coefficient appeared to cause a slower rate of convergence which was seen by smaller $\delta/2$ values for the same number of analysis increments as visible in the plots. Lowering the release tolerance also appeared to influence the convergence which was either seen by smaller $\delta/2$ for the same number of analysis increments as visible in the plots or early termination of the analysis as shown in Table II. Changing the release tolerance, however, appeared to have no effect on the overall load/displacement behavior or the magnitude of the saw tooth pattern.

In summary, good agreement between analysis results and the benchmark could be achieved for different release tolerance values in combination with global or contact stabilization or viscous regularization. Selecting the appropriate input parameters, however, was not straightforward and

often required several iterations where the parameters had to be changed. All results had a saw tooth pattern which appears to depend on the mesh size at the front.

5.2.2 Computed delamination lengths for DCB specimen with unidirectional layup

An alternate way to plot the benchmark is shown in Figures 21 and 22 where the delamination length a is plotted versus the applied opening displacement $\delta/2$ (Figure 21) and the computed load P (Figure 22). This way of presenting the results is shown since it may be of advantage for large structures where local delamination propagation may have little effect on the global stiffness of the structure and may therefore not be visible in a global load/displacement plot.

For the examples plotted in Figure 23 and 24, global stabilization was used in the analysis. For a stabilization factor of $2x10^{-6}$ (in green), a saw tooth pattern was observed when the delamination length a was plotted versus the applied opening displacement $\delta/2$ (Figure 23). The average, however, was in good agreement with the benchmark result. For a stabilization factor of $2x10^{-7}$ (in red), the average appeared to be in better agreement with the benchmark result until termination after 550 increments due to convergence problems. For a stabilization factor of $2x10^{-8}$ (in black for a release tolerance of 0.2), the computed results were on top of the previous result. When the delamination length a is plotted versus the computed load P, the saw tooth pattern is more pronounced as shown in Figure 24 for the same stabilization factors as above. The average results are in good agreement with the benchmark result.

5.2.3 Computed total strain energy and damping energies for DCB specimen with unidirectional layup

The total strain energy U of the DCB is calculated from the external load P and the crack opening displacement δ as shown in Figure 3 such that

$$U = \frac{P \cdot \delta}{2} \tag{6}$$

The calculation is illustrated in Figure 25 using the load/displacement benchmark curve discussed above. The areas under the load/displacement curve correspond to the energies U_a calculated for one arm of the DCB specimen for different loads P and at different delamination lengths a. The total strain energies *ALLSE* obtained from ABAQUS® are plotted in Figure 26 versus the applied opening displacement $\delta/2$ for models of the DCB specimen with different delamination length a. The quadratic relationship between the total strain energy and the opening displacement

$$U = \frac{P \cdot \delta}{2} \quad \text{and} \quad P = C \cdot \delta \Rightarrow \frac{\delta^2 \cdot C}{2} \tag{7}$$

is clearly visible for constant compliance C (constant delamination length a). For comparison, the total strain energies U for a model with a=40 mm were calculated using the applied opening displacement and the computed load (equation 7). The results were included in Figure 26 (solid brown triangles) and show an excellent agreement with the curve fit through internally computed results from ABAQUS® (*ALLSE*).

It was assumed that the energies calculated for the critical load/displacement curve can be used as a benchmark with respect to the total strain energy. For the delamination propagation,

therefore, the results obtained from the model of a DCB specimen with an initially straight delamination of a=30 mm length should follow the benchmark path (in red) in Figure 26.

In the VCCT for ABAQUS® manual, it is suggested to monitor the energy absorbed by damping: *ALLSD* for contact or global stabilization, *ALLVD* for viscous damping [19]. The amount of damping energy in the models is compared to the total strain energy in the model (*ALLSE*). Ideally, the value of the damping energy should be a small fraction of the total energy. In Figures 27 to 32, the computed damping energies and the total strain energy in the model of the DCB specimen are plotted versus the applied crack tip opening (δ/2) for different input parameters which correspond to the results shown in Figures 15 to 20.

For the results plotted in Figure 27, global stabilization was added to the analysis and the analysis results shown correspond to the load/displacement results shown in Figure 15. For a stabilization factor of $2x10^{-5}$, the calculated total strain (plotted in blue) exceeds the benchmark result. For the other stabilization factors of $2x10^{-6}$, $2x10^{-7}$, $2x10^{-8}$ (plotted in green, red and black) the calculated total strain energies plotted are almost identical and fall slightly below the benchmark result. A saw tooth pattern is observed for all the results. For different input parameters, significantly different stabilization energies were computed. Below the critical point, the stabilization energy was basically zero. Once delamination propagation starts, the stabilization energy was required to avoid numerical problems. The lowest stabilization energies were observed for stabilization factors of $2x10^{-6}$, $2x10^{-7}$, $2x10^{-8}$ in combination with a release tolerance of 0.2 (plotted in green, red and black). The results were almost identical and reached about 20% of the total strain energy in the model. Lowering the release tolerance to 0.02 (plotted in light blue) and 0.002 (plotted in violet) for a stabilization factor of $2x10^{-8}$ appears to increase the stabilization energy to about 25% in the example shown. The results obtained for a stabilization factor of $2x10^{-5}$ and a release tolerance of 0.2 lie in the middle.

The result obtained for adaptive automatic stabilization and a release tolerance value of 0.2 is plotted in Figure 28. The analysis results shown correspond to the load/displacement results shown in Figure 16. The calculated total strain energy, for which a saw tooth pattern is observed, falls slightly below the benchmark result. For applied displacements below the critical point, the stabilization energy was basically zero. Once delamination propagation starts, the stabilization energy was required to avoid numerical problems and reached about 25% of the total strain energy in the model.

The results obtained for the coarse meshes shown in Figures 6a (plotted in red) and 6b (plotted in blue) are shown in Figure 29. The analysis results shown correspond to the load/displacement results shown in Figure 17. A stabilization factor of $2x10^{-8}$ and a release tolerance of 0.002 was used for the coarse meshes. One result obtained for the fine mesh with the same stabilization factor and a release tolerance of 0.2 (in black) was added to the plot as a reference result. Changing the mesh size significantly influenced the magnitude of the saw tooth pattern, the peak values, however, were in good agreement with the benchmark total strain energy. Larger elements yielded an increased saw tooth pattern in spite of the fact a release tolerance two orders of magnitude smaller than the reference result was chosen. The lowest stabilization energy (about 20% of the total strain energy) was observed for the reference result with a stabilization factor of $2x10^{-8}$ in combination with a release tolerance of 0.2. Lowering the release tolerance to 0.002 and increasing the element size appears to increase the stabilization energy to more than 50% in the example shown.

For the results plotted in Figure 30, contact stabilization was added to the analysis. These results correspond to the load/displacement results shown in Figure 18. For all combinations of

stabilization factors and release tolerances, a saw tooth pattern was observed, where the peak values were in good agreement with the benchmark total strain energy. The lowest stabilization energies were observed for stabilization factors of $1x10^{-5}$, $1x10^{-6}$, $1x10^{-7}$ in combination with a release tolerance of 0.2 (plotted in red, blue and light blue). The stabilization energy results were almost identical and reached more than 20% of the total strain energy in the model. Lowering the release tolerance to 0.02 (plotted in orange) and 0.002 (plotted in green) for a stabilization factor of $1x10^{-7}$ appears to increase the stabilization energy to more than 30% in the example shown. The stabilization energy followed the same path for a release tolerance of 0.002 for stabilization factors of $1x10^{-7}$ and $1x10^{-3}$.

The results obtained for models made of continuum shell elements SC8R (shown in Figure 7) are shown in Figure 31. The analysis results shown correspond to the load/displacement results shown in Figure 19. A stabilization factor of $1x10^{-7}$ and a release tolerance of 0.2 were used for the fine mesh where three continuum shell elements were used over the thickness of one arm as shown in Figure 5b (in green). The release tolerance was lowered to a value of 0.002 for the fine mesh shown in Figure 7a where only one element was used over the thickness of one arm. The calculated total strain energies plotted are almost identical and fall slightly below the benchmark result. Changing the mesh size for a stabilization factor of $1x10^{-7}$ and a release tolerance of 0.2 significantly influenced the magnitude of the saw tooth pattern, the peak values, however, were in good agreement with the benchmark total strain energy. Larger elements yielded an increased saw tooth pattern. The lowest stabilization energy (about 20% of the total strain energy) was observed for the fine mesh shown in Figure 5b, a stabilization factor of $1x10^{-7}$ and a release tolerance value of 0.2 (plotted in green). Larger elements yielded an increased saw tooth pattern (plotted in red and blue) but also increased the stabilization energy required to more than 35%. Lowering the release tolerance to a values of 0.002 (plotted in black) also lead to an increase in stabilization energy.

For all combinations of the viscosity coefficient and release tolerance, a saw tooth pattern was obtained, where the peak values were in good agreement with the benchmark total strain energy as shown in Figure 32. The analysis results shown correspond to the load/displacement results shown in Figure 20. The lowest stabilization energies were observed for stabilization factors of $1x10^{-4}$, $1x10^{-5}$, in combination with a release tolerance of 0.5 (plotted in red and green). The results were almost identical and reached only about 5% of the total strain energy in the model. Lowering the release tolerance to 0.3 for viscosity coefficients of $1x10^{-4}$, $1x10^{-5}$ (plotted in blue and black) appears to increase the stabilization energy to more than 15% in the example shown.

In summary, good agreement between analysis results and the total strain energy benchmark could be achieved for different release tolerance values in combination with global or contact stabilization or viscous regularization. All results had a saw tooth pattern and the magnitude of which appears to depend on the mesh size at the delamination front. Larger elements yielded an increased saw tooth pattern. Stabilization energies of about 20%-25% of the total stain energy were observed when release tolerance values of 0.5 and 0.2 were used. Lowering the release tolerance to values of 0.02 or 0.002 resulted in an increase in stabilization energy. The lowest stabilization energies (about 5% of the total strain energy in the model) were observed for viscosity coefficients of $1x10^{-4}$, $1x10^{-5}$, in combination with a release tolerance of 0.5. In spite of the variations in stabilization energy, all the load/displacement results were in good agreement with the benchmark as shown earlier in Figures 15 to 20. It is therefore uncertain if the amount of stabilization energy absorbed can be used as a measure to determine the quality of the analysis results.

5.2.4 Computed delamination front shape

Besides matching the load displacement behavior of benchmark results, a delamination propagation analysis should also yield a delamination front shape that is representative of the actual failure. An example of delamination front shapes observed by opening a tested DCB specimen are shown in Figure 33a [43]. From the initial straight delamination front which is formed by the edge of the Teflon insert, the delamination develops into a curved thumbnail shaped front. The front remains thumbnail shaped if the test is continued and the delamination continues to grow. Delamination propagation computed using the model with a uniform mesh across the width (Figure 5b) is shown in Figure 33b at the end of the analysis after 1000 increments. Plotted on the bottom surface (defined in Figure 5b) are the contours of the bond state, where the delaminated section appears in red and the intact (bonded) section in blue. The transition between the colors indicates the location of the delamination front. The initial straight front was included for clarification. The first propagation was observed in the center of the specimen as expected from the distribution of the energy release rate (Figure 11) and the failure index (Figure 12). The front propagated across the width of the specimen until a new straight front was reached. Subsequently, the propagation starts again in the center. During the analysis, the front never developed into the expected curved thumbnail front, and the analysis terminated with a straight front as shown in Figure 33b. This result is somewhat unsatisfactory but may be explained by the fact that the failure index in this particular example is nearly constant across about 80% of the width of the specimen as shown in Figure 12. An even finer mesh may be required to capture the lagging propagation near the edge.

5.3 Creating a Benchmark Solution for a DCB specimen with multi-directional layup

The analysis outlined in Section 4.1 were repeated for a DCB specimen with multi-directional layup. First, the mode I strain energy release rate values were computed which are plotted versus the normalized width, y/B, of the specimen as shown in Figure 34. The results were obtained from models shown in Figure 8 for ten different delamination lengths a. An opening displacement $\delta/2$=1.0 mm was applied to each arm of the model. Qualitatively, the mode I strain energy release rate is fairly constant in the center part of the specimen and drops progressively towards the edges. Compared to the DCB with unidirectional layup, the constant center section is smaller, and the drop towards the edges occurs earlier for specimens with the multi-directional layup. These effects are caused by increased anticlastic bending in the more compliant specimens with the multi-directional layup [24, 25]. Computed mode I strain energy release rates decreased with increasing delamination length a.

The failure index G_T/G_c was computed next, based on a mode I fracture toughness G_{Ic}=340.5 J/m^2 for C12K/R6376 (see Figure 2b). The failure index was plotted versus the normalized width, y/B, of the specimen as shown in Figure 35. For all delamination lengths modeled, except for a=40 mm, the failure index in the center of the specimen (y/B=0) is above unity ($G_T/G_c \geq 1$).

For all delamination lengths modeled, the reaction loads P at the location of the applied displacement were calculated and plotted versus the applied opening displacement $\delta/2$ as shown in Figure 36. The critical load P_{crit} and critical displacement $\delta_{crit}/2$ were calculated for each delamination length modeled using equation (5), and the results were included in the load/displacement plots as shown in Figure 37 (solid red circles). As before, it was assumed that the critical load/displacement results can be used as a benchmark. For the delamination propagation,

therefore, the load/displacement results obtained from the model of a DCB specimen with an initially straight delamination of a=30 mm length should correspond to the critical load/displacement path (solid red line) in Figure 37.

5.4 Delamination Propagation in a DCB specimen with multi-directional layup

5.4.1 Computed load/displacement behavior for different input parameters

The propagation analysis was performed in two steps using the model shown in Figure 8 for a delamination length 31 mm. In the first step, a prescribed displacement (δ/2= 0.7 mm) was applied in two increments. Dividing the first step into just two increments was possible, since the load-displacement behavior of the specimen up to failure was linear as shown in Figure 37. In the second step, the total prescribed displacement was increased (δ/2= 2.8 mm). Automatic incrementation was used with a small increment size at the beginning (10^{-4} of the total increment) and a very small minimum allowed increment (10^{-18} of the total increment) to reduce the risk of numerical instability and early termination of the analysis. The analysis was limited to 1000 increments.

In Figure 38, the computed resultant force (load P) at the tip of the DCB specimen is plotted versus the applied crack tip opening (δ/2) for different input parameters. For the results shown, the analysis terminated when the 1000 increment limit set for the analysis was reached. To overcome the convergence problems, global stabilization, contact stabilization and viscous regularization were used with input parameters for which good results had been obtained for the analysis of the unidirectional DCB specimen. Viscous regularization was added to the analysis with a viscosity coefficient of $1x10^{-5}$ and a release tolerance of 0.3 (plotted in green). The analysis using contact stabilization was performed with a stabilization a factor of $1x10^{-7}$ and a release tolerance of 0.002 (plotted in blue). For global stabilization, a factor of $2x10^{-7}$ was used in combination with a release tolerance value of 0.2 (plotted in red). For all different input parameters, which are also listed in Table II, converged solutions were obtained, and the analyses reached the predetermined 1000 increment limit. All results had a saw tooth pattern, where the average values were in good agreement with the benchmark result. Compared to results obtained from analyses with global stabilization (in red) and contact stabilization (in blue), the results obtained with viscous regularization (in green) appear to have a better rate of convergence. For the same number of total increments (1000), the analysis continued to a higher opening displacement (δ/2= 1.24 mm).

5.4.2 Computed total strain energy and damping energies for DCB specimen with multi-directional layup

As discussed earlier for the DCB specimen with unidirectional layup, it is assumed that the plot of the total strain energy versus the applied crack tip opening displacement (δ/2) can be used as a benchmark result. The benchmark result obtained from ABAQUS® analyses from models of the multi-directional DCB specimen is plotted (in grey) in Figure 39. For the delamination propagation, the results obtained from the model of a DCB specimen with an initially straight delamination of a=31 mm length are expected to follow the path of the benchmark.

In Figure 39, the total strain energy in the model of the DCB specimen and the computed damping energies are plotted versus the applied crack tip opening (δ/2) for different input parameters which correspond to the results shown in Figure 38. For all the results plotted, a saw tooth pattern is observed. The calculated total strain energies are in good agreement with the

benchmark result. For a viscosity coefficient of $1x10^{-5}$ and a release tolerance of 0.3 (plotted in green), the total strain energy slightly exceeds the benchmark result. For the different input parameters, significantly different stabilization energies were computed. Below the critical point, the stabilization energy was basically zero for all results. Once delamination propagation starts, the stabilization energy was required to avoid numerical problems. The lowest stabilization energies were observed for a viscosity coefficient of $1x10^{-5}$ and a release tolerance of 0.3 (plotted in green) and reached about 11% of the total strain energy in the model. Lowering the release tolerance to 0.2 (plotted in red) for a global stabilization factor of $2x10^{-7}$ and 0.002 (plotted in blue) for a contact stabilization factor of $1x10^{-7}$ appears to increase the stabilization energy to about 20% in the example shown. In spite of the variations in stabilization energy, all the load/displacement results were in good agreement with the benchmark. It is therefore uncertain if the amount of stabilization energy absorbed can be used as a measure to determine the quality of the analysis results.

5.4.3 Computed delamination front shape for a DCB specimen with multi-directional layup

An initial straight delamination front develops into a curved thumbnail shaped front which was shown for an opened tested DCB specimen in Figure 33a. The front remains thumbnail shaped if the test is continued and the delamination continues to grow. The thumbnail shaped front is caused by the anticlastic bending of the arms which is more prevalent in the more compliant arms of a multi-directional specimen [44]. Delamination propagation computed using the model with a uniform mesh across the width (Figure 8) is shown in Figure 40 at the end of the analysis after 1000 increments. Plotted on the bottom surface (defined in Figure 8) are the contours of the bond state, where the delaminated section appears in red, and the intact (bonded) section in blue. The transition between the colors indicates the location of the delamination front. The initial straight delamination front was included for clarification. The first propagation was observed in the center of the specimen as expected from the distribution of the energy release rate (Figure 34) and the failure index (Figure 35). During the analysis, the front developed into the expected curved thumbnail front. Compared to results obtained from analyses with contact stabilization (Figure 40a), the results obtained with viscous regularization (Figure 40b) appear to have a better rate of convergence since for the same limit of 1000 increments the front grew further into the specimen. Compared to the straight fronts obtained from the models of the unidirectional DCB specimen (shown in Figure 33b), the current results are encouraging. It remains however somewhat unclear what degree of mesh refinement is required to accurately capture the delamination front shape.

5.5 Creating a Benchmark Solution for a SLB specimens

The computed total strain energy release rate values were plotted versus the normalized width, y/B, of the SLB specimen as shown in Figure 41. The results were obtained from geometrically nonlinear analysis of models shown in Figure 9 for twelve different delamination lengths a. An arbitrary center deflection w=2.8 mm was applied as shown in Figure 3. Qualitatively, the total energy release rate is fairly constant in the center part of the specimen and drops towards the edges. Peaks in the distribution are observed at the edges. Computed total strain energy release rates decreased with increasing delamination length a.

The sum of the shear components $G_S = G_{II}+G_{III}$ and the mixed-mode ratio G_S/G_T were also calculated for each nodal point along the delamination front across the width of the specimen. The mixed-mode ratio G_S/G_T was plotted versus the normalized width, y/B, of the specimen as shown in

Figure 42. Qualitatively, the mixed-mode ratio is fairly constant in the center part of the specimen progressively increasing towards the edges. Using the mixed-mode failure criterion for C12K/R6376 (see Figure 2b), the failure index G_T/G_c was computed for each node along the delamination front and plotted versus the normalized width, y/B, of the specimen as shown in Figure 43. For the center deflection applied, the failure index G_T/G_c in the center is well below unity. The failure index is almost constant in the center of the specimen, drops towards the edges and increases again in the immediate vicinity of the edge. To reach G_T/G_c=1 in the center of the specimen (y/B=0), a critical center deflection, w_{crit}, and corresponding critical load P_{crit}, were calculated using equation (5) for all delamination lengths modeled.

For all delamination lengths modeled, the reaction load P at the location of the applied deflection were calculated and plotted versus the applied center deflection, w, as shown in Figure 44. The calculated critical center deflection, w_{crit}, and corresponding critical load values, P_{crit}, were added to the plots as shown in Figure 45 (solid red circles). The results indicated that, with increasing delamination length, less load is required to extend the delamination. At the same time also, the values of the critical center deflection decreased. This means that the SLB specimen exhibits unstable delamination propagation under load as well as displacement control (dashed red line). From these critical load/displacement results, a benchmark solution can be created. To define the benchmark, it is assumed that prescribed center deflections are applied in the analysis instead of nodal point loads P to minimize problems with numerical stability of the analysis caused by the unstable propagation. Once the critical center deflection is reached and delamination propagation starts, the applied displacement must be held constant over several increments while the delamination front is advanced during these increments. Once the stable path is reached, the applied center deflection is increased again incrementally. For the simulated delamination propagation, therefore, the load/displacement results obtained from the model of a SLB specimen with an initially straight delamination length of a=34 mm should correspond to the benchmark load/displacement path (solid red line) as shown in Figure 45.

5.6 Delamination Propagation in a SLB Specimen using VCCT for ABAQUS®

5.6.1 Computed load/displacement behavior for different input parameters

The propagation analysis was performed in two steps using the models shown in Figures 8 and 9. In the first step, a central deflection (w= 3.1 mm) was applied in two increments which equaled nearly the critical center deflection (w_{crit}= 3.23 mm) determined in the analysis above. Dividing the first step into just two increments was possible, since the load-displacement behavior of the specimen up to failure was linear as shown in Figure 45. In the second step, the total prescribed displacement was increased (w= 5.0 mm). Automatic time incrementation was used with a small initial time increment size (10^{-3}) and a very small minimum allowed time increment (10^{-17}) to reduce the risk of numerical instability and early termination of the analysis. The analysis was limited to 1000 increments.

In Figures 46 to 50, the computed resultant force (load P) at the center of the SLB specimen is plotted versus the center deflection (w) for different input parameters which are listed in Table II. The analysis terminated before the total prescribed center deflection was applied. For the results shown, the analysis terminated when the 1000 increment limit set for the analysis was reached. Several analyses terminated early because of convergence problems. The results computed when global stabilization was used are plotted in Figure 46. For a stabilization factor of $2x10^{-5}$, the load increased suddenly at the beginning of the second load step (plotted in blue). Then, the load

continued to increase on a path with the same stiffness as the benchmark but offset to higher loads. The load continued to increase until a point was reached where delamination propagation started and the load decreased. The analysis was stopped by the user. For a stabilization factor of $2x10^{-6}$ (in green), the delamination propagation started at the critical center deflection. In the beginning, the load/displacement path followed the constant deflection branch of the benchmark result very well. At the transition between the constant deflection branch and the stable propagation branch of the benchmark result, the applied center deflection was about 2% higher compared to the benchmark. For the stable path, a saw tooth pattern was observed but the minimum is in good agreement with the benchmark result.

An adaptive automatic stabilization scheme was recently added to ABAQUS®/Standard in version 6.7. The adaptive automatic stabilization scheme does not require the input of a fixed stabilization factor mentioned above. The results obtained are plotted in Figure 47. For the default setting, the load increased suddenly at the beginning of the second load step (plotted in blue). Then, the load continued to increase on a path with the same stiffness as the benchmark but offset to higher loads. The load continued to increase until a point was reached where delamination propagation started and the load decreased. The analysis was stopped by the user. To obtain converged results, the stabilization factor at the beginning of the analysis was determined by the user and automatic stabilization adjusted the settings in the following increments. For an initial stabilization factor of $2x10^{-6}$ (in red), the delamination propagation started at the critical center deflection. In the beginning, the load/displacement path followed the constant deflection branch of the benchmark result very well but overshot and did not follow the stable path. When the initial stabilization factor was changed to $2x10^{-7}$ (in light blue) and $2x10^{-8}$ (in black), the same path was followed as before but the analysis terminated early. Increasing the release tolerance to 0.5 and 0.9 for selected initial stabilization factors $2x10^{-7}$ (in orange) and $2x10^{-6}$ (in green) did not lead to a converged solution. Further improvement of the automatic stabilization scheme is required before it can be used reliably.

The results computed when contact stabilization was used are plotted in Figure 48. For a small stabilization factor ($1x10^{-6}$) and a release tolerance (0.2) suggested in the handbook [19], the load dropped and delamination propagation started prior to reaching the critical point of the benchmark solution (plotted in blue). The load/displacement path then ran parallel to the constant deflection branch of the benchmark result but the analysis terminated early due to convergence problems. The stabilization factor and release tolerance had to be increased to avoid premature termination of the analysis. For a stabilization factor of $1x10^{-3}$ and release tolerance of 0.5 (in green), the load dropped at the critical point of the benchmark solution. First, the center deflection kept increasing with decreasing load. Later, the load/displacement path ran parallel to the constant deflection branch of the benchmark result. At the transition between the constant deflection branch and the stable propagation branch of the benchmark result, the applied center deflection was about 2% higher compared to the benchmark. For the stable path, a saw tooth pattern was observed where the average results were in good agreement with the benchmark result. The difference between the maximum and minimum values was much smaller than in the case where global stabilization was used (see Figure 46). The best results compared to the benchmark were obtained for even higher values of the stabilization factors of $1x10^{-4}$ and a release tolerance of 0.5 (in red).

When viscous regularization was used to help overcome convergence issues, a value of 0.2 was used initially for the release tolerance as suggested in the handbook [19]. Convergence could not be achieved which led to an increase in the release tolerance. The results are plotted in Figure 49. For a small viscosity coefficient of $1x10^{-4}$ and a release tolerance of 0.5 (in blue), the

load dropped at the critical point, but the center deflection kept increasing with decreasing load. Then, the analysis terminated early due to convergence problems. For an increased viscosity coefficient of $1x10^{-2}$ and a release tolerance of 0.5 (in red), the load dropped at the critical point and the load/displacement path started following the constant deflection branch of the benchmark result, but the analysis terminated early due to convergence problems. The viscosity coefficient and release tolerance had to be increased further to avoid premature termination of the analysis. For a viscosity coefficient of $1x10^{-1}$ and a release tolerance of 0.9 (in green), the load dropped at the critical point. First, the center deflection kept increasing with decreasing load. Later, the load/displacement path ran parallel to the constant deflection branch of the benchmark result. At the transition between the constant deflection branch and the stable propagation branch of the benchmark result, the applied center deflection is about 2.5% higher compared to the benchmark. For the stable path, a saw tooth pattern is observed where the average results are in good agreement with the benchmark result. The difference between the maximum and minimum values is much smaller compared to the cases where global or contact stabilization was used.

In Figure 50, the computed resultant force (load *P*) in the center of the SLB specimen is plotted versus the applied center deflection (*w*) for the model of the SLB specimen shown in Figure 10. For the results shown, the analysis terminated when the 1000 increment limit set for the analysis was reached. To overcome the convergence problems, global stabilization, contact stabilization and viscous regularization were used with input parameters for which good results had been obtained previously (FE model shown in Figure 9). For a viscosity coefficient of $1x10^{-1}$ and a release tolerance of 0.9 (in green), the load dropped at the critical point. First, the center deflection kept increasing with decreasing load. Later, the computed load/displacement path ran parallel to the constant deflection branch of the benchmark result. At the transition between the constant deflection branch and the stable propagation branch of the benchmark result, the applied center deflection was about 2.5% higher compared to the benchmark. For contact stabilization, a factor of $1x10^{-4}$ and a release tolerance of 0.5 were chosen (plotted in blue). The computed load started decreasing at the critical point of the benchmark solution. First, the center deflection kept increasing with decreasing load. Later, the computed path ran parallel to the constant deflection branch of the benchmark result. At the transition between the constant deflection branch and the stable propagation branch of the benchmark result, the applied center deflection was about 2% higher compared to the benchmark. For a stabilization factor of $2x10^{-6}$ (in red), the delamination propagation started at the critical center deflection. In the beginning, the load/displacement path followed the constant deflection branch of the benchmark result very well. At the transition between the constant deflection branch and the stable propagation branch of the benchmark result, the applied center deflection was about 2% higher compared to the benchmark. For all results, a saw tooth pattern was observed along the stable path, the average results however, were in good agreement with the benchmark result.

In summary, good agreement between analysis results and the benchmark could be achieved for different release tolerance values in combination with global or contact stabilization or viscous regularization. Selecting the appropriate input parameters, however, was not straightforward and often required several iterations in which the parameters had to be changed.

5.6.2 Computed delamination lengths for SLB specimen with multi-directional layup

An alternate way to plot the benchmark is shown in Figures 51 and 52 where the delamination length *a* is plotted versus the applied center deflection *w* (Figure 51) and the computed load *P* (Figure 52). This way of presenting the results is shown, since it may be of advantage for

large structures where local delamination propagation may have little effect on the global stiffness of the structure and may therefore not be visible in a global load/displacement plot.

For the examples plotted in Figures 53 and 54, global stabilization and contact stabilization was used in the analysis. For a global stabilization factor of $2x10^{-6}$ (in green), the delamination propagation started at the critical center deflection as shown in Figure 53. The plotted results followed the benchmark result very well including the transition between the constant deflection branch and the stable propagation branch of the benchmark result. For the stable path, a saw tooth pattern was observed where the maximum was in good agreement with the benchmark result. For a contact stabilization factor of $1x10^{-4}$ and a release tolerance of 0.5 (in red) the results also followed the benchmark result very well. When the delamination length a is plotted versus the computed load P, the saw tooth pattern becomes more visible as shown in Figure 54 for the same stabilization factors as above. The increased saw tooth pattern corresponds to the pattern observed in the load/displacement plot shown in Figures 46 and 48. In spite of the saw tooth pattern observed, the average results are in good agreement with the benchmark result.

5.6.3 Computed total strain energy and damping energies for SLB specimen with multi-directional layup

As discussed earlier for the DCB specimen, it is assumed that the total strain energy versus applied center deflection plot can also be used as a benchmark result. For models of the SLB specimen with different delamination length a, the total strain energies *ALLSE* obtained from ABAQUS® are plotted versus the applied center deflection, w, as shown in Figure 55. The calculated total strain energy values corresponding to the critical center deflection, w_{crit}, and critical load values, P_{crit}, at delamination onset (shown in Figure 45) were added to the plots (solid red circles). The results indicated that, with increasing delamination length, the total strain energy in the system decreases. Simultaneously, the values of the critical center deflection also decrease. This means that the SLB specimen exhibits unstable delamination propagation under load as well as displacement control. From these critical energy/displacement results, a benchmark solution can be created. To define the benchmark, it is assumed that prescribed center deflections are applied in the analysis instead of nodal point loads P to minimize problems with numerical stability of the analysis caused by the unstable propagation. Once the critical center deflection is reached and delamination propagation starts, the applied displacement must be held constant over several increments while the delamination front is advanced during these increments. Once the stable path is reached, the applied center deflection is increased again incrementally. For the simulated delamination propagation, therefore, the total strain energy/displacement results obtained from the model of a SLB specimen with an initially straight delamination length of a=34 mm should correspond to the critical total strain energy/displacement path (solid red line) as shown in Figure 55.

In Figure 56, the total strain energy in the model of the SLB specimen and the computed global stabilization energies are plotted versus the applied center deflection (w) for different input parameters which correspond to the results shown in Figure 46. For the two results plotted, a saw tooth pattern is observed. For a stabilization factor of $2x10^{-5}$ (in blue), the total strain energy first followed the benchmark result but continued to increase once the critical point was reached. The energy increased until a point was reached where delamination propagation started and the energy started decreasing. The analysis was stopped by the user. For a stabilization factor of $2x10^{-6}$ (in green), the delamination propagation started at the critical center deflection. In the beginning, the total strain energy/displacement path followed the constant deflection branch of the benchmark

result very well. At the transition between the constant deflection branch and the stable propagation branch of the benchmark result, the applied center deflection was about 2% higher compared to the benchmark. For the stable path, a saw tooth pattern was observed but the average energy is in good agreement with the benchmark result. The stabilization energy was basically zero for both results before delamination onset. Once delamination propagation starts, the stabilization energy was required to avoid numerical problems. For a stabilization factor of $2x10^{-6}$ (in green), the stabilization energy reached about 40% of the total strain energy in the model, the load/displacement results plotted in Figure 46 however were in good agreement with the benchmark.

In Figure 57, the total strain energy in the model of the SLB specimen and the computed stabilization energies are plotted versus the applied center deflection (w) for different input parameters which correspond to the results for automatic stabilization shown in Figure 47. For the default factor (in blue), the total strain energy first followed the benchmark result but continued to increase once the critical point was reached. The energy increased until a point was reached where delamination propagation started and the energy started decreasing. The analysis was stopped by the user. None of the other settings yielded a converged solution. The results up to the termination of the analysis are included for completeness. The stabilization energy was basically zero before delamination onset. Once delamination propagation starts, the stabilization energy was required to avoid numerical problems. Since none of the analyses reached the stable branch of the benchmark before termination, it is unclear how much stabilization energy would have been required. As mentioned above, further improvement of the automatic stabilization scheme is required before it can be used reliably.

The results computed when contact stabilization was used are plotted in Figure 58. The results correspond to the load/displacement plots shown in Figure 48. For a small stabilization factor ($1x10^{-6}$) and a release tolerance (0.2) suggested in the handbook [19], delamination propagation started prior to reaching the critical point of the benchmark solution (plotted in blue), and the energy dropped. The path then ran parallel to the constant deflection branch of the benchmark result but the analysis terminated early due to convergence problems. The stabilization factor and release tolerance were increased to avoid premature termination of the analysis. For a stabilization factor of $1x10^{-3}$ and release tolerance of 0.5 (in green), the energy started decreasing at the critical point of the benchmark solution. First, the center deflection kept increasing with decreasing total strain energy. Later, the computed path ran parallel to the constant deflection branch of the benchmark result. At the transition between the constant deflection branch and the stable propagation branch of the benchmark result, the applied center deflection was about 2% higher compared to the benchmark. For the stable path, a saw tooth pattern was observed where the average results were in good agreement with the benchmark result. The best results compared to the benchmark were obtained for even higher values of the stabilization factors of $1x10^{-4}$ and a release tolerance of 0.5 (in red). For both results, the stabilization energy reached about 45% of the total strain energy in the model, the load/displacement results plotted in Figure 48 however were in good agreement with the benchmark.

The results computed when viscous regularization was used are plotted in Figure 59. The results correspond to the load/displacement plots shown in Figure 49. For a small viscosity coefficient of $1x10^{-4}$ and a release tolerance of 0.5 (in blue), the calculated total strain energy started decreasing at the critical point, but simultaneously the center deflection kept increasing with decreasing energy. Then, the analysis was terminated early due to convergence problems. For an increased viscosity coefficient of $1x10^{-2}$ and a release tolerance of 0.5 (in red), the total strain energy dropped at the critical point and the computed path started following the constant deflection branch

of the benchmark result, but the analysis terminated early due to convergence problems. The viscosity coefficient and release tolerance had to be increased further to avoid premature termination of the analysis. For a viscosity coefficient of $1x10^{-1}$ and a release tolerance of 0.9 (in green), the total strain energy dropped at the critical point. First, the center deflection kept increasing with decreasing load. Later, the computed path ran parallel to the constant deflection branch of the benchmark result. At the transition between the constant deflection branch and the stable propagation branch of the benchmark result, the applied center deflection is about 2.5% higher compared to the benchmark. For the stable path, a saw tooth pattern was observed where the average results are in good agreement with the benchmark result. The stabilization energy reached about 34% of the total strain energy in the model, the load/displacement results plotted in Figure 49 however were in good agreement with the benchmark.

In Figure 60, the results obtained from the model of the SLB specimen shown in Figure 10 are plotted versus the applied center deflection, *w*, for different input parameters. The results correspond to the load/displacement plots shown in Figure 50. For a viscosity coefficient of $1x10^{-1}$ and a release tolerance of 0.9 (in green), the total strain energy dropped at the critical point. First, the center deflection kept increasing with decreasing load. Later, the computed path ran parallel to the constant deflection branch of the benchmark result. At the transition between the constant deflection branch and the stable propagation branch of the benchmark result, the applied center deflection is about 2.5% higher compared to the benchmark. For contact stabilization, a factor of $1x10^{-4}$ and release tolerance of 0.5 were chosen. The computed total strain energy (in blue) started decreasing at the critical point of the benchmark solution. First, the center deflection kept increasing with decreasing total strain energy. Later, the computed path ran parallel to the constant deflection branch of the benchmark result. At the transition between the constant deflection branch and the stable propagation branch of the benchmark result, the applied center deflection was about 2% higher compared to the benchmark. For a stabilization factor of $2x10^{-6}$ (in red), the delamination propagation started at the critical center deflection. In the beginning, the total strain energy/displacement path followed the constant deflection branch of the benchmark result very well. At the transition between the constant deflection branch and the stable propagation branch of the benchmark result, the applied center deflection was about 2% higher compared to the benchmark. For all results, a saw tooth pattern was observed along the stable path, the average energy however, was in good agreement with the benchmark result. The stabilization energy before delamination onset was basically zero for all results. Once delamination propagation started, the stabilization energy was required to avoid numerical problems. The stabilization energy reached about 40% of the total strain energy in the model, the load/displacement results plotted in Figure 50 however were in good agreement with the benchmark.

In summary, good agreement between analysis results and the total strain energy benchmark could be achieved for different release tolerance values in combination with global or contact stabilization or viscous regularization. All results had a saw tooth pattern the magnitude of which appears to depend on the mesh size at the front. Stabilization energies of about 34%-45% of the total stain energy were observed when release tolerance values of 0.9, 0.5 and 0.2 were used. In spite of the variations in stabilization energy, all the load/displacement results were in good agreement with the benchmark as discussed earlier and shown Figures 46 and 48-50. It is therefore uncertain if the amount of stabilization energy absorbed can be used as a measure to determine the quality of the analysis results.

5.6.4 Computed delamination front shape for a SLB specimen with multi-directional layup

Delamination propagation computed using the model with a uniform mesh across the width (Figure 9) is shown in Figures 61 and 62 after 76 and 1000 increments, respectively. Plotted on the bottom surface (defined in Figure 9) are the contours of the bond state variable. The bond state varies between 0.0 (fully bonded shown in dark blue) and 1.0 (fully disbonded shown in red) [19]. The transition between the colors indicates the location of the delamination front. The initial straight front was included for clarification. The first propagation is observed near the center and corresponds to the maximum in the distribution of the failure index (Figure 43). The front then propagated across the width. Further propagation created a curved front where the edges lag behind as shown in Figure 61. This result is in good agreement with expectations based on the distribution of the failure index shown in Figure 43. Once the delamination propagation extends into the coarser part of the mesh, the curved front cannot be represented as well as shown in Figure 62. Delamination propagation computed using the model with an extended finer mesh (Figure 10) is shown in Figure 63a and b after 476 and 1000 increments, respectively. During propagation through the fine section the curved front is clearly visible as shown in Figure 63a. As mentioned above the curved front cannot be represented as well once delamination propagation extends into the coarser part of the mesh as shown in Figure 63b. C-scans or x-ray photographs of tested specimens were not available for comparison.

6. SUMMARY AND CONCLUSIONS

An approach for assessing the delamination propagation simulation capabilities in commercial finite element codes is presented and demonstrated for the commercial finite element code ABAQUS® with focus on their implementation of the Virtual Crack Closure Technique (VCCT). For this investigation, the Double Cantilever Beam (DCB) specimen with a unidirectional and a multi-directional layup and the Single Leg Bending (SLB) specimen with a multi-directional layup were chosen for full three-dimensional finite element simulations. First, critical load/displacement results were defined for delamination onset which were used subsequently as benchmarks. Second, starting from an initially straight front, the delamination was allowed to propagate based on the algorithms implemented into VCCT for ABAQUS®. VCCT control parameters were varied to study the effect on the computed load-displacement behavior during propagation. It was assumed that for good results, the computed load-displacement relationship should correspond to the benchmark results. Third, as a qualitative assessment, the shape of the computed delamination fronts were also compared to photographs of failed specimens.

The results showed the following:

- Good agreement between the load-displacement relationship obtained from the propagation analysis results and the benchmark results could be achieved by selecting the appropriate input parameters. However, selecting the appropriate VCCT input parameters such as release tolerance, global or contact stabilization and viscous regularization, was not straightforward and often required an iterative procedure.
- The default setting for global stabilization yielded unsatisfactory results although the analysis converged.
- Analysis with automatic global stabilization yielded unsatisfactory results.
- Best results were obtained when contact stabilization and viscous regularization were used.
- Accurately computing the delamination front shape requires fine meshes.

- A coarse mesh could lead to an increased saw tooth behavior during propagation analysis.
- Good agreement between analysis results and the total strain energy benchmark could be achieved for different release tolerance values in combination with global or contact stabilization or viscous regularization.
- Load/displacement results were in good agreement with the benchmark for cases where the stabilization energies varied between 5% and 25% for the analysis of the DCB specimen and between 34% and 45% for the analysis of the SLB specimen. It is therefore uncertain if the amount of stabilization energy absorbed can be used as a measure to determine the quality of the analysis results.

Overall, the results are promising. In a real case scenario, however, where the results are unknown, obtaining the right solution will remain challenging. Further studies are required which should include different levels of mesh refinement, new stabilization options and the use of continuum shell elements to more efficiently model the specimens. Additionally, assessment of the propagation capabilities in more complex specimens and on a structural level is required.

ACKNOWLEDGEMENTS

This research was supported by the Aircraft Aging and Durability Project as part of NASA's Aviation Safety Program.

REFERENCES

[1] T.K. O'Brien, *Characterization of Delamination Onset and Growth in a Composite Laminate*, in Damage in Composite Materials, ASTM STP 775,: American Society for Testing and Materials, 1982, pp. 140-167.

[2] A.C. Garg, *Delamination - A Damage Mode in Composite Structures*, Engineering Fracture Mechanics, vol. 29, pp. 557-584, 1988.

[3] V.V. Bolotin, *Delaminations in Composite Structures: Its Origin, Buckling, Growth and Stability*, Composites Part B: Engineering, vol. 27B, pp. 129-145, 1996.

[4] T.E. Tay, *Characterization and Analysis of Delamination Fracture in Composites - An Overview of Developments from 1990 to 2001*, Applied Mechanics Reviews, vol. 56, pp. 1-32, 2003.

[5] R.H. Martin, *Incorporating Interlaminar Fracture Mechanics Into Design*, in International Conference on Designing Cost-Effective Composites: IMechE Conference Transactions, London, U.K., pp. 83-92, 1998.

[6] T.K. O'Brien, *Fracture Mechanics of Composite Delamination*, in ASM Handbook, Volume 21, Composites: ASM International, pp. 241-245, 2001.

[7] *ASTM D 5528-94a, Standard Test Method for Mode I Interlaminar Fracture Toughness of Unidirectional Fiber-Reinforced Polymer Matrix Composites*, in Annual Book of ASTM Standards, vol. 15.03: American Society for Testing and Materials, 2000.

[8] *ASTM D 6671-01, Standard Test Method for Mixed Mode I-Mode II Interlaminar Fracture Toughness of Unidirectional Fiber Reinforced Polymer Matrix Composites*, in Annual Book of ASTM Standards, vol. 15.03: American Society for Testing and Materials, 2000.

[9] B.D. Davidson, X. Sun, and A.J. Vinciquerra, *Influences of Friction, Geometric Nonlinearities, and Fixture Compliance on Experimentally Observed Toughnesses from Three and Four-point Bend End-notched Flexure Tests*, Journal of Composite Materials, vol. 41, pp. 1177-1196, 2007.

[10] M. König, R. Krüger, K. Kussmaul, M. v. Alberti, and M. Gädke, *Characterizing Static and Fatigue Interlaminar Fracture Behaviour of a First Generation Graphite/Epoxy Composite*, in Composite Materials: Testing and Design - (13th Vol.), ASTM STP 1242, S.J. Hooper, Ed.: American Society for Testing and Materials, pp. 60-81, 1997.

[11] B.D. Davidson and W. Zhao, *An Accurate Mixed-Mode Delamination Failure Criterion for Laminated Fibrous Composites Requiring Limited Experimental Input,* Journal of Composite Materials, vol. 41, pp. 679-702, 2007.

[12] T.K. O'Brien, *Composite Interlaminar Shear Fracture Toughness, G_{IIc}: Shear Measurement or Sheer Myth?*, in Composite Materials: Fatigue and Fracture, Seventh Volume, ASTM STP 1330, pp. 3-18, 1998.

[13] M.L. Benzeggagh and M. Kenane, *Measurement of Mixed-Mode Delamination Fracture Toughness of Unidirectional Glass/Epoxy Composites with Mixed-Mode Bending Apparatus*, Composites Science and Technology, vol. 56, pp. 439-449, 1996.

[14] J. Reeder, *3D Mixed-Mode Delamination Fracture Criteria - An Experimentalist's Perspective*. Proceedings of American Society for Composites, 21st Annual Technical Conference, Dearborn, Michigan, 2006.

[15] S.M. Lee, *An Edge Crack Torsion Method for Mode III Delamination Fracture Testing*, Journal of Composite Technology and Research, pp. 193-201, 1993.

[16] J.G. Ratcliffe, *Characterization of the Edge Crack Torsion (ECT) Test for Mode III Fracture Toughness Measurement of Laminated Composites*, NASA/TM-2004-213269, 2004.

[17] E.F. Rybicki and M.F. Kanninen, *A Finite Element Calculation of Stress Intensity Factors by a Modified Crack Closure Integral*, Engineering Fracture Mechanics, vol. 9, pp. 931-938, 1977.

[18] R. Krueger, *Virtual Crack Closure Technique: History, Approach and Applications*, Applied Mechanics Reviews, vol. 57, pp. 109-143, 2004.

[19] *VCCT for ABAQUS - Version 1.3-1, User's Manual*, ABAQUS®, 2007.

[20] *MSC Nastran 2007 r1, Implicit Nonlinear (SOL 600) User's Guide*. MSC Software, 2007.

[21] *Marc® and Mentat® 2007 r1, Release Guide*. MSC Software, 2007.

[22] M. Bruyneel, P. Morelle, and J.P. Delsemme, *Failure Analysis of Metallic and Composite Structures with SAMCEF*, in NAFEMS Seminar: Materials Modeling – FE Simulations of the Behavior of Modern Industrial Materials Including their Failure, Niedernhausen, Germany, 2006.

[23] D.M. Parks, *The Virtual Crack Extension Method for Nonlinear Material Behavior*, Computer Methods in Applied Mechanics and Engineering, vol. 12, pp. 353-364, 1977.

[24] R. Krüger, *Three Dimensional Finite Element Analysis of Multidirectional Composite DCB, SLB and ENF Specimens*, Institute for Statics and Dynamics of Aerospace Structures, University of Stuttgart, ISD-Report No. 94/2, 1994.

[25] B.D. Davidson, R. Krüger, and M. König, *Effect of Stacking Sequence on Energy Release Rate Distributions in Multidirectional DCB and ENF Specimens*, Engineering Fracture Mechanics, vol. 55, pp. 557-569, 1996.

[26] B.D. Davidson, R. Krüger, and M. König, *Three Dimensional Analysis of Center Delaminated Unidirectional and Multidirectional Single Leg Bending Specimens*, Composites Science and Technology, vol. 54, pp. 385-394, 1995.

[27] R. Krueger and D. Goetze, *Influence of Finite Element Software on Energy Release Rates Computed Using the Virtual Crack Closure Technique*, NIA Report No. 2006-06, NASA/CR-214523, 2006.

[28] A. Pieracci, B.D. Davidson, and V. Sundararaman, *Nonlinear Analyses of Homogeneous, Symmetrically Delaminated Single Leg Bending Specimens*, Journal of Composites Technology and Research, vol. 20, pp. 170-178, 1998.

[29] *KaleidaGraph: Data Analysis/Graphing Application for Macintosh and Windows Operating Systems*: Synergy Software, 1996.

[30] M. König, R. Krüger, and S. Rinderknecht, *Finite Element Analysis of Delamination Growth in a Multidirectional Composite ENF Specimen*, in Composite Materials: Theory and Practice, ASTM STP 1383, P. Grant and C.Q. Rousseau, Eds.: American Society for Testing and Materials, pp. 345-365, 2000.

[31] R.H. Martin, *Evaluation of the Split Cantilever Beam for Mode III Delamination Testing*, in Composite Materials: Fatigue and Fracture (Third Volume), ASTM STP 1110, pp. 243-266, 1991.

[32] P. Robinson and D.Q. Song, *A New Mode III Delamination Test for Composites*, Advanced Composites Letters, vol. 1, pp. 160-164, 1992.

[33] *ABAQUS 6.7, Analysis User's Manual, Volume IV: Elements*, ABAQUS 2007.

[34] I.S. Raju, J.H. Crews, and M.A. Aminpour, *Convergence of Strain Energy Release Rate Components for Edge-Delaminated Composite Laminates*, Engineering Fracture Mechanics, vol. 30, pp. 383-396, 1988.

[35] C.T. Sun and M.G. Manoharan, *Strain Energy Release Rates of an Interfacial Crack Between Two Orthotropic Solids*, Journal of Composite Materials, vol. 23, pp. 460-478, 1989.

[36] S.W. Tsai, *Theory of Composite Design*: Think Composites, 1992.

[37] S.W. Tsai and H.T. Hahn, *Introduction to Composite Materials*: Technomic Publishing Co., Inc., 1980.

[38] I.S. Raju, K.N. Shivakumar, and J.H. Crews, Jr., *Three-Dimensional Elastic Analysis of a Composite Double Cantilever Beam Specimen*, AIAA Journal, vol. 26, pp. 1493-1498, 1988.

[39] R. Krüger, M. König, and T. Schneider, *Computation of Local Energy Release Rates Along Straight and Curved Delamination Fronts of Unidirectionally Laminated DCB- and ENF - Specimens*, in Proceedings of the 34th AIAA/ASME/ASCE/AHS/ASC SSDM Conference, La Jolla, CA: American Institute of Aeronautics and Astronautics, Washington, pp. 1332-1342, 1993.

[40] B.D. Davidson and R.A. Schapery, *Effect of Finite Width on Deflection and Energy Release Rate of an Orthotropic Double Cantilever Specimen*, Journal of Composite Materials, vol. 22, pp. 640-656, 1988.

[41] B.D. Davidson, *An Analytical Investigation of Delamination Front Curvature in Double Cantilever Beam Specimens*, Journal of Composite Materials, vol. 24, pp. 1124-1137, 1990.

[42] D. Broek, *The Practical Use of Fracture Mechanics*: Kluwer Academic Publishers, 1991.

[43] U. Koser, *Experimentelle Ermittlung der Energiefreisetzungsrate an Matrix-Rissen im Faserverbundwerkstoff T300/976*, Diplomarbeit: Staatliche Materialprüfungsanstalt (MPA), University of Stuttgart, 1989.

[44] J.J. Polaha, B.D. Davidson, R.C. Hudson, and A. Pieracci, *Effects of Mode Ratio, Ply Orientation and Precracking on the Delamination Toughness of a Laminated Composite*, Journal of Reinforced Plastics and Composites, vol. 15, pp. 141-173, 1996.

TABLE 1. MATERIAL PROPERTIES.

T300/1076 Unidirectional Graphite/Epoxy Prepreg		
E_{11} = 139.4 GPa	E_{22} = 10.16 GPa	E_{33} = 10.16 GPa
ν_{12} = 0.30	ν_{13} = 0.30	ν_{23} = 0.436
G_{12} = 4.6 GPa	G_{13} = 4.6 GPa	G_{23} = 3.54 GPa
C12K/R6376 Unidirectional Graphite/Epoxy Prepreg		
E_{11} = 146.9 GPa	E_{22} = 10.6 GPa	E_{33} = 10.6 GPa
ν_{12} = 0.33	ν_{13} = 0.33	ν_{23} = 0.33
G_{12} = 5.45 GPa	G_{13} = 5.45 GPa	G_{23} = 3.99 GPa

The material properties are given with reference to the ply coordinate axes where index 11 denotes the ply principal axis that coincides with the direction of maximum in-plane Young's modulus (fiber direction). Index 22 denotes the direction transverse to the fiber in the plane of the lamina and index 33 denotes the direction perpendicular to the plane of the lamina.

TABLE II. INPUT PARAMETERS.

FE model	global stabilization	contact stabilization	viscous regularization	release tolerance	last increment
DCB-st3	$2\ 10^{-5}$			0.2	381
DCB-st4	$2\ 10^{-6}$			0.2	1002
DCB-st5	$2\ 10^{-7}$			0.2	550
DCB-st6	$2\ 10^{-8}$			0.2	1002
DCB-st7	$2\ 10^{-8}$			0.02	1002
DCB-st8	$2\ 10^{-8}$			0.002	451
DCB-ct1		$1\ 10^{-5}$		0.2	1002
DCB-ct2		$1\ 10^{-6}$		0.2	1002
DCB-ct3		$1\ 10^{-7}$		0.2	751
DCB-ct4		$1\ 10^{-7}$		0.02	1002
DCB-ct5		$1\ 10^{-7}$		0.002	1002
DCB-ct6		$1\ 10^{-3}$		0.002	911
DCB-vr1			$1\ 10^{-4}$	0.5	1002
DCB-vr2			$1\ 10^{-4}$	0.3	273
DCB-vr3			$1\ 10^{-5}$	0.5	1002
DCB-vr4			$1\ 10^{-5}$	0.3	1002
SLB-st1	$2\ 10^{-5}$			0.2	266
SLB-st2	$2\ 10^{-6}$			0.2	1002
SLB-ct1		$1\ 10^{-6}$		0.2	133
SLB-ct6		$1\ 10^{-5}$		0.5	811
SLB-ct8		$1\ 10^{-4}$		0.5	1002
SLB-vr1			$1\ 10^{-4}$	0.5	65
SLB-vr6			$1\ 10^{-2}$	0.5	88
SLB-vr12			$1\ 10^{-1}$	0.9	537

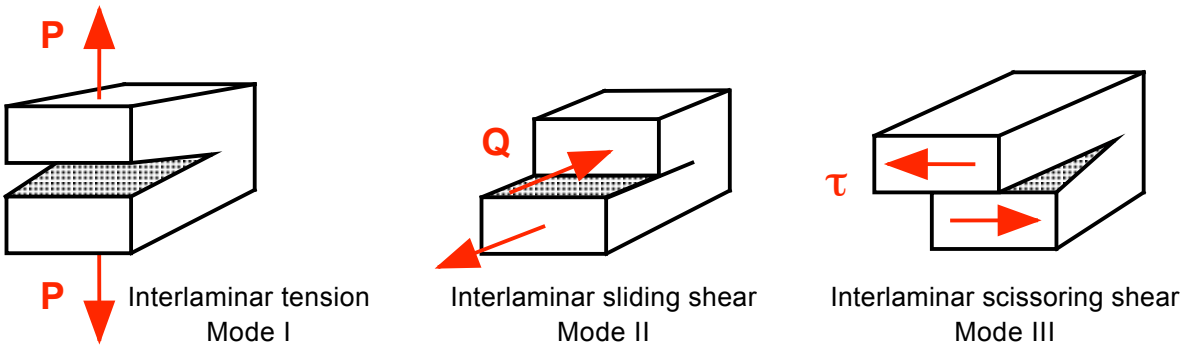

Figure 1. *Fracture Modes*.

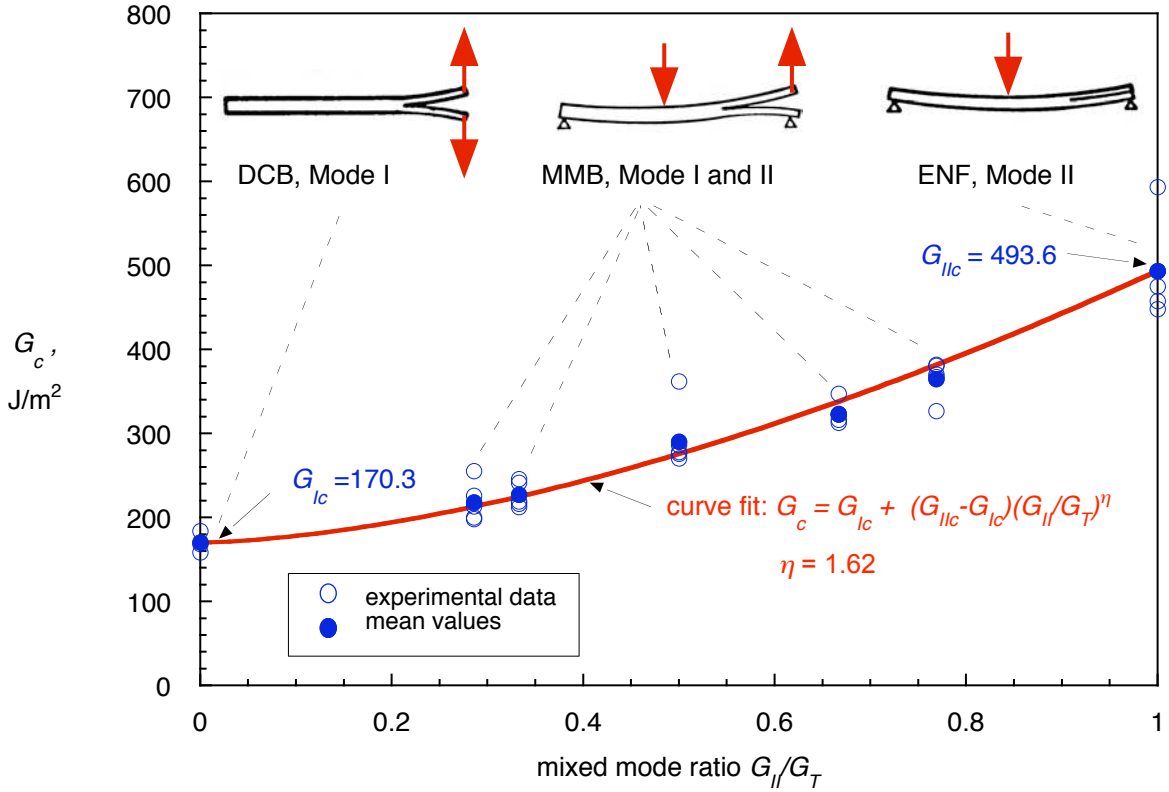

a. *T300/914C.*

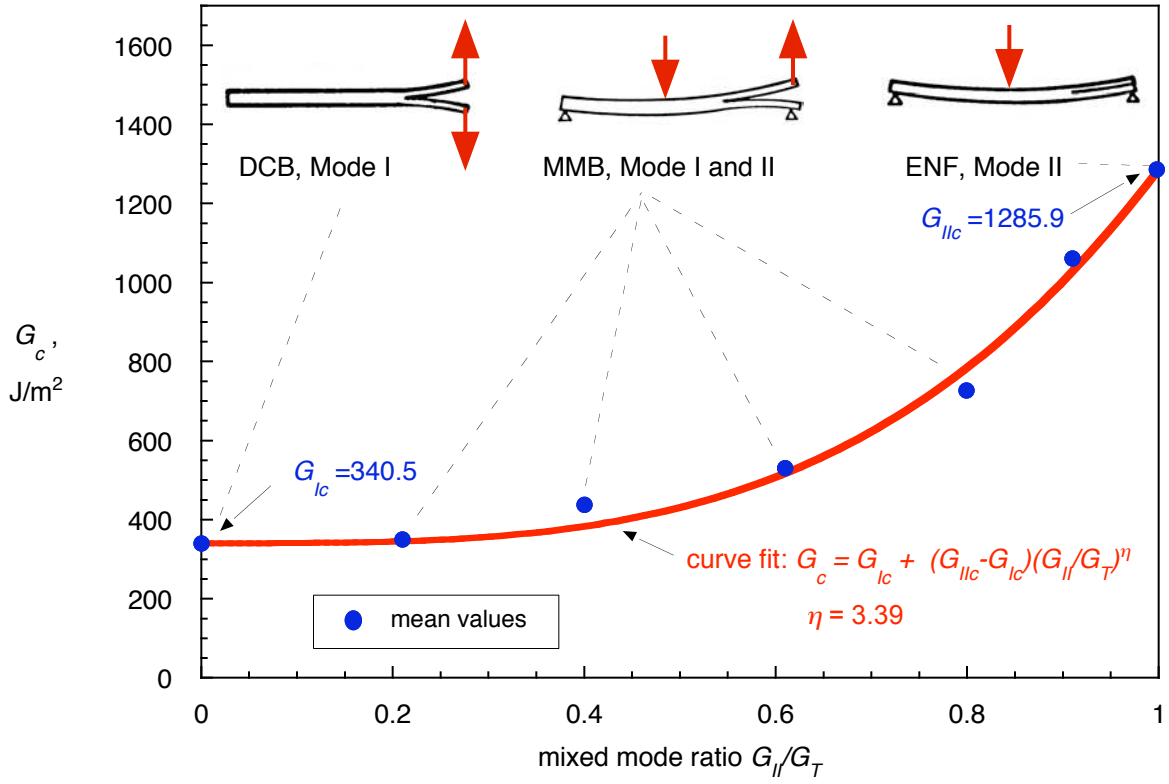

b. *C12K/R6376.*

Figure 2. *Mixed-mode fracture criterion for composite materials.*

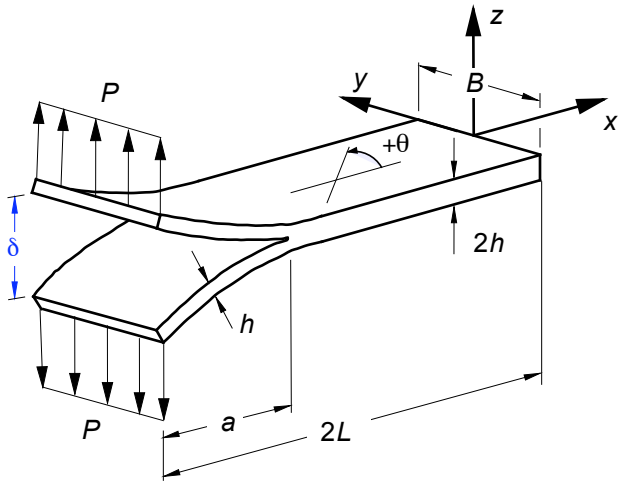

B	25.0 mm
2*h*	3.0 mm
2*L*	150.0 mm
a	30.0 mm

T300/914C $[0]_{24}$

D±30: C12K/R6376 [±30/0/-30/0/30/0_4/30/0/-30/0/-30/30/-30/30/0/30/0/ -30/0_4/-30/0/30/±30]

a. ***D**ouble **C**antilever **B**eam Specimen (DCB)*

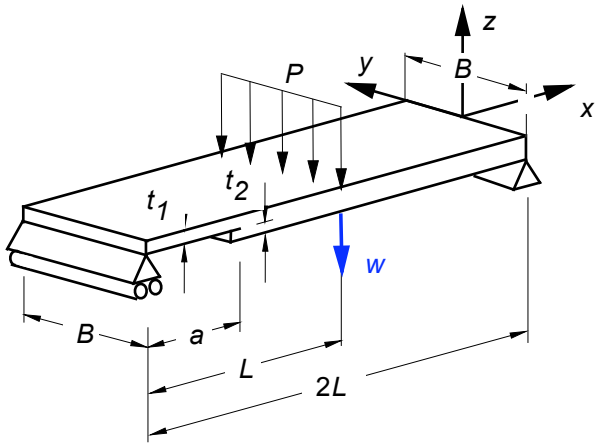

B	25.4 mm
t_1	2.032 mm
t_2	2.032 mm
2*L*	177.8 mm
a	34.29 mm

D±30: C12K/R6376 [±30/0/-30/0/30/0_4/30/0/-30/0/-30/30/-30/30/0/30/0/ -30/0_4/-30/0/30/±30]

b. ***S**ingle **L**eg **B**ending Specimen (SLB)*

Figure 3. *Specimen configurations*.

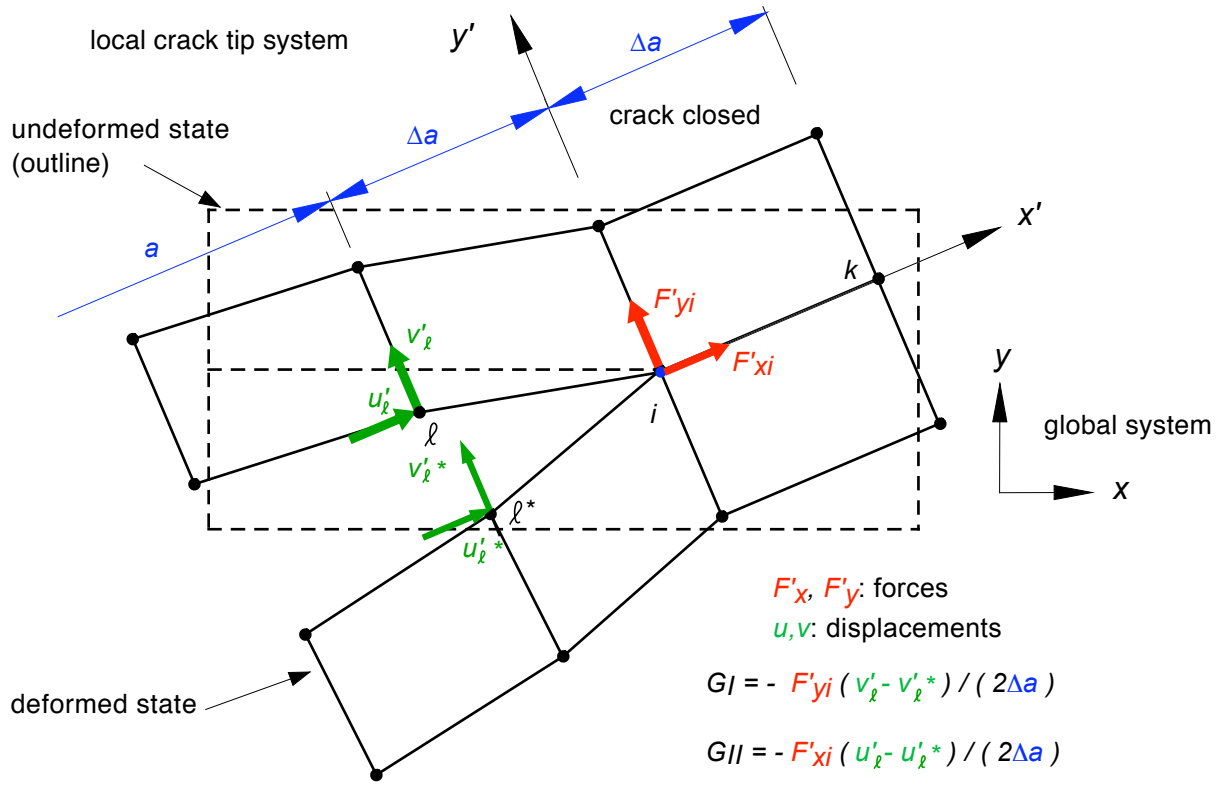

a. *VCCT for geometrically nonlinear analysis*

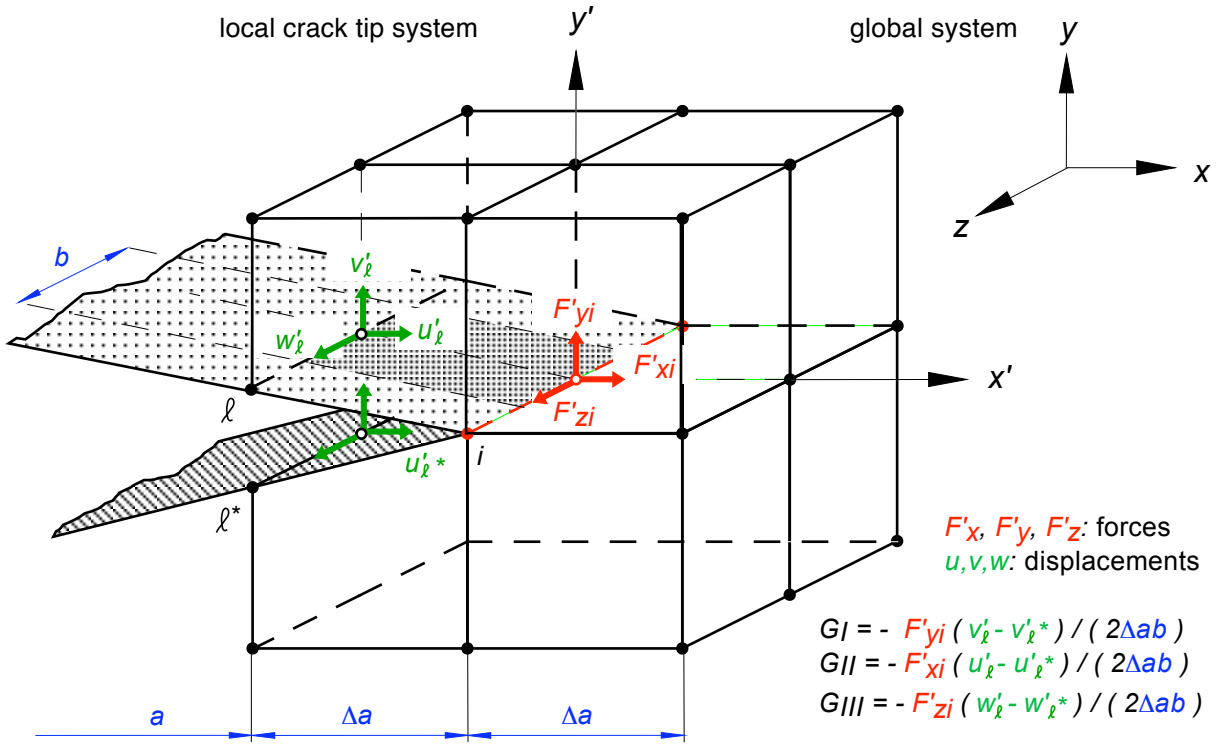

b. *VCCT for eight node solid elements*

Figure 4. *Virtual Crack Closure Technique (VCCT).*

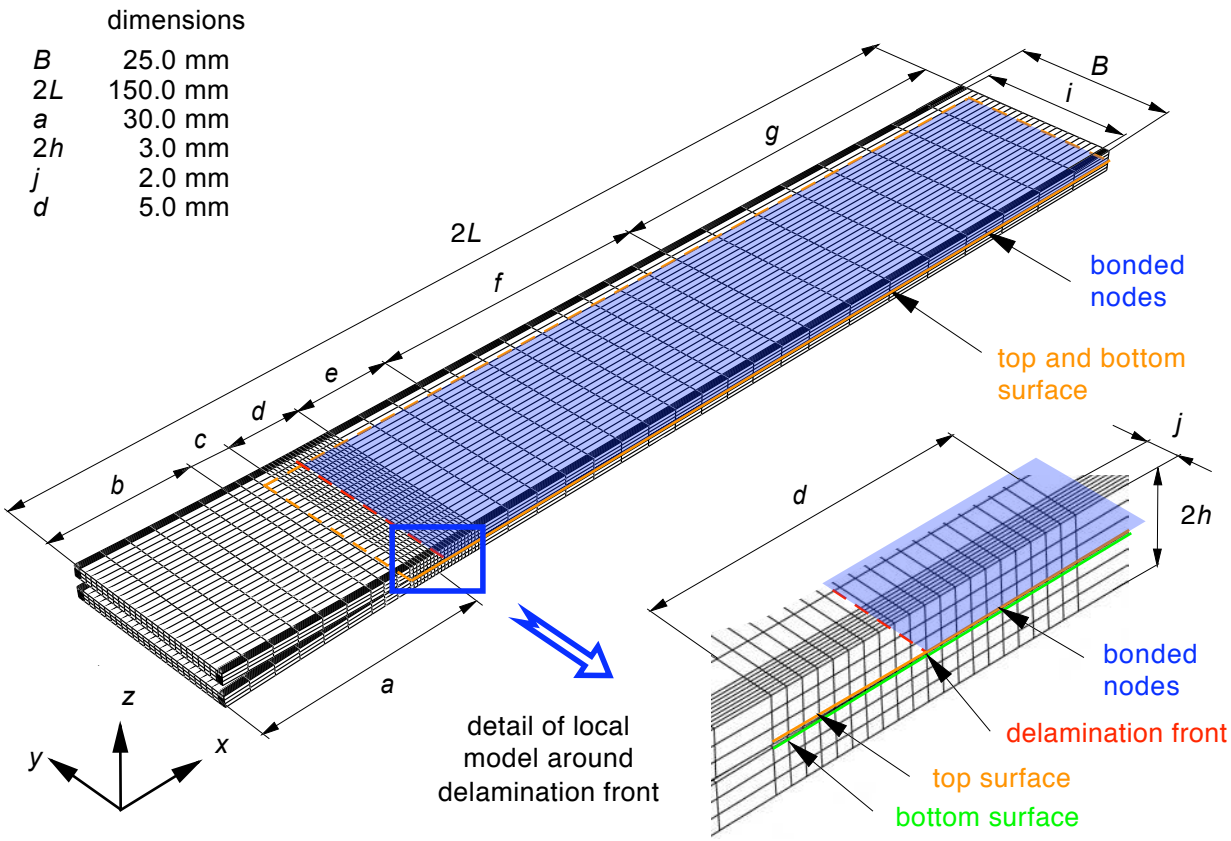

a. *Deformed model of DCB specimen with refined edges*

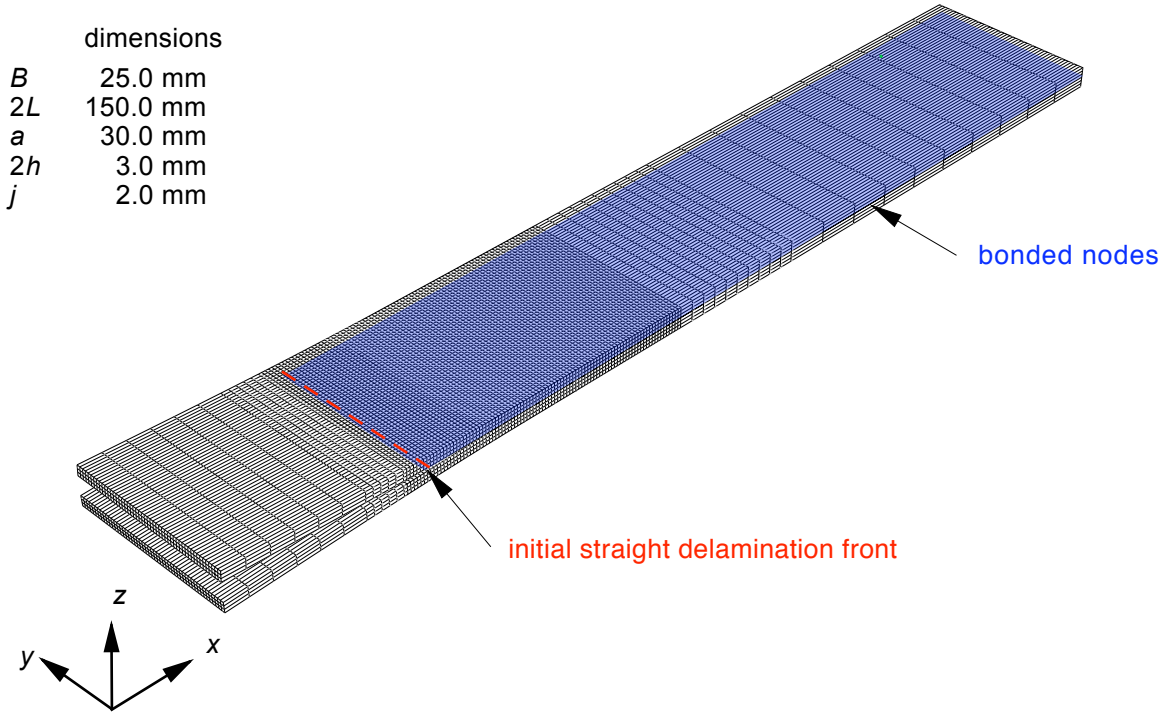

b. *Deformed model of a DCB specimen for VCCT for ABAQUS analysis*

Figure 5. *Full three-dimensional finite element models of a DCB specimen.*

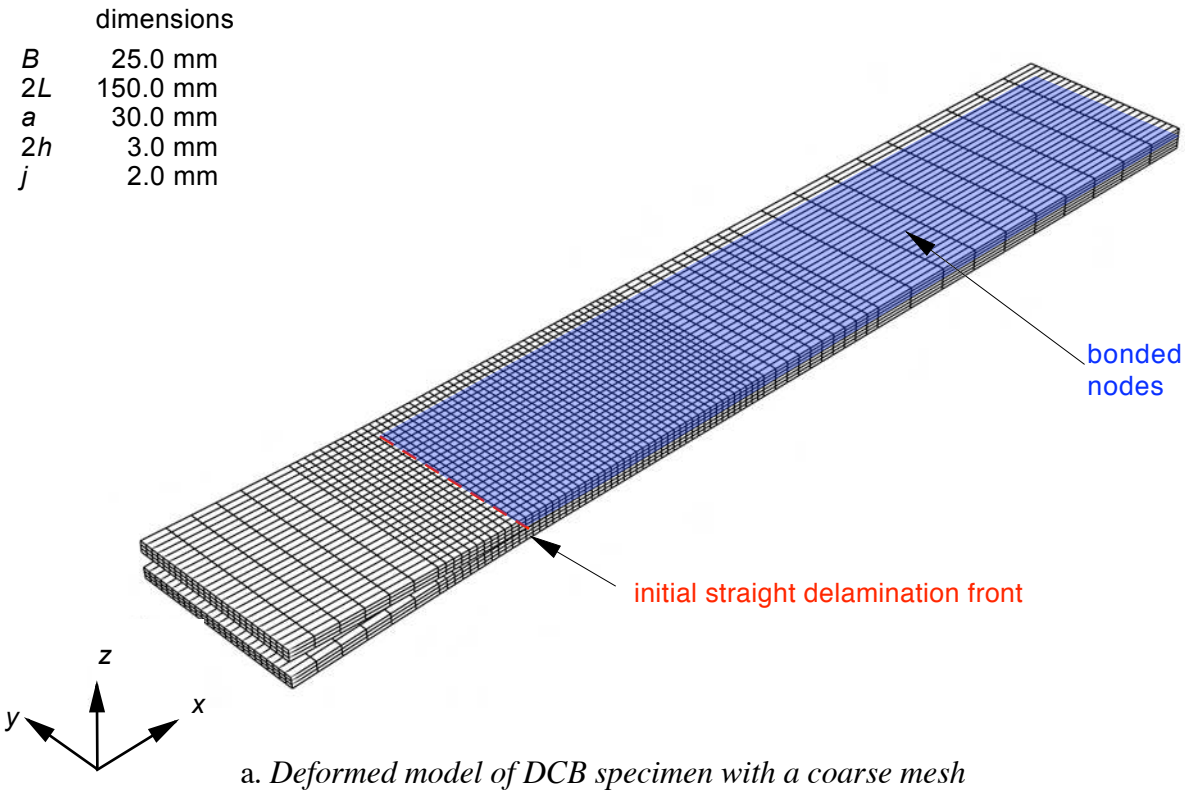

a. *Deformed model of DCB specimen with a coarse mesh*

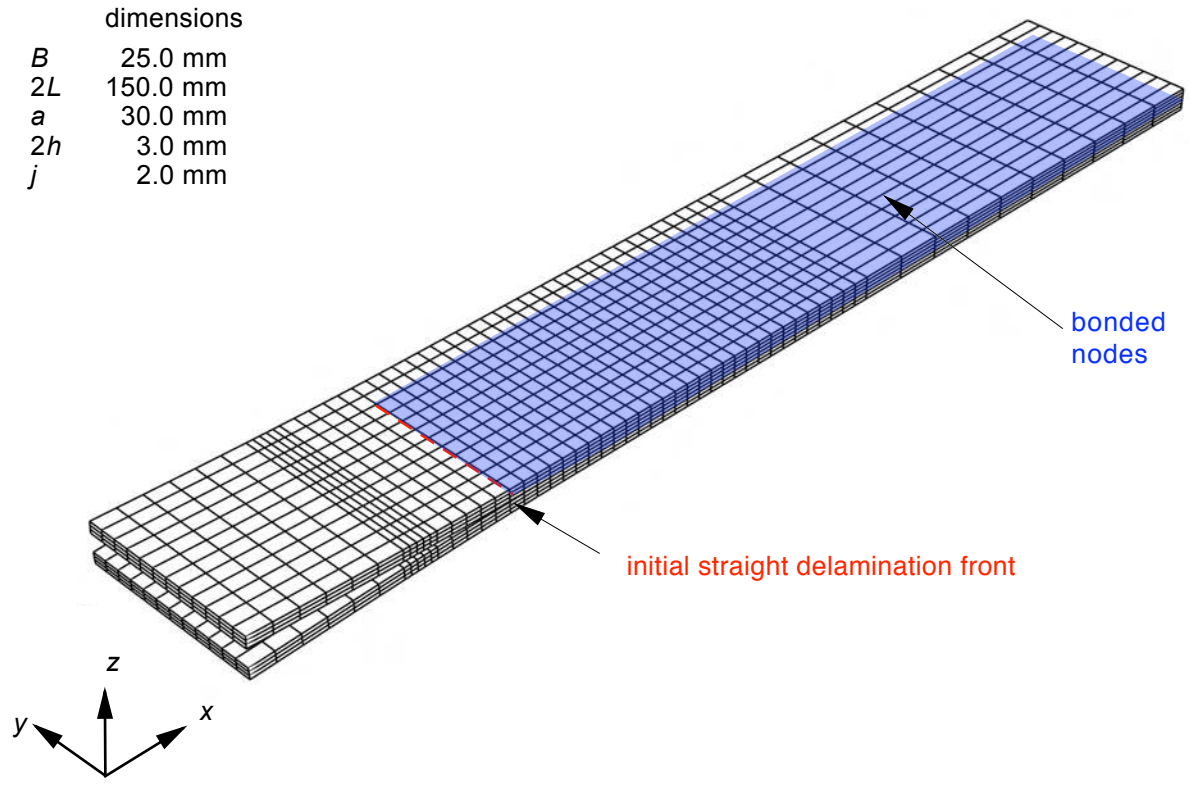

b. *Deformed model of a DCB specimen with a coarse mesh*

Figure 6. *Coarse full three-dimensional finite element models of a DCB specimen.*

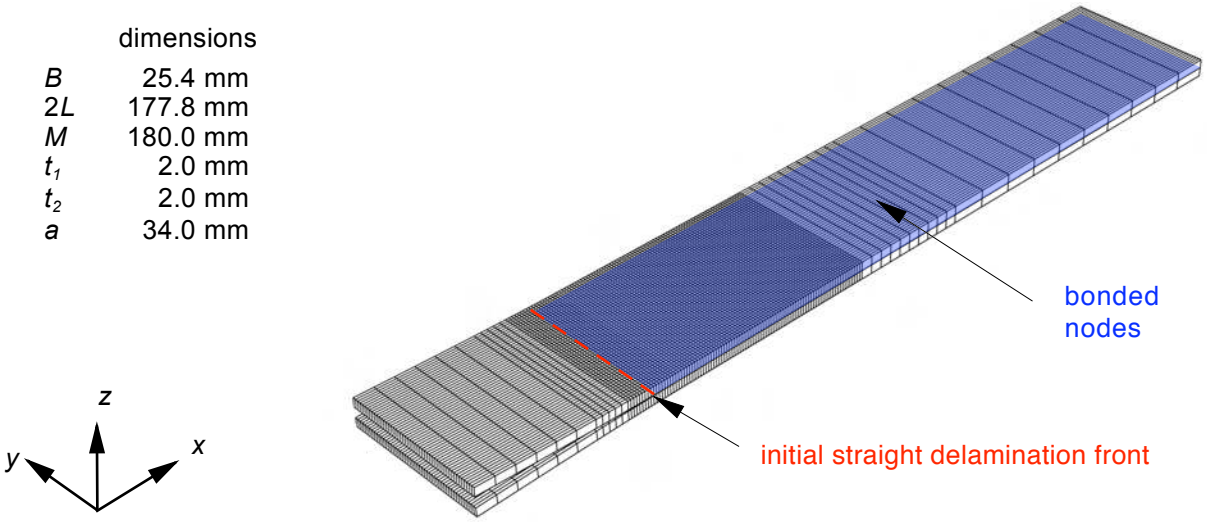

a. *Deformed model of DCB specimen with a fine mesh*

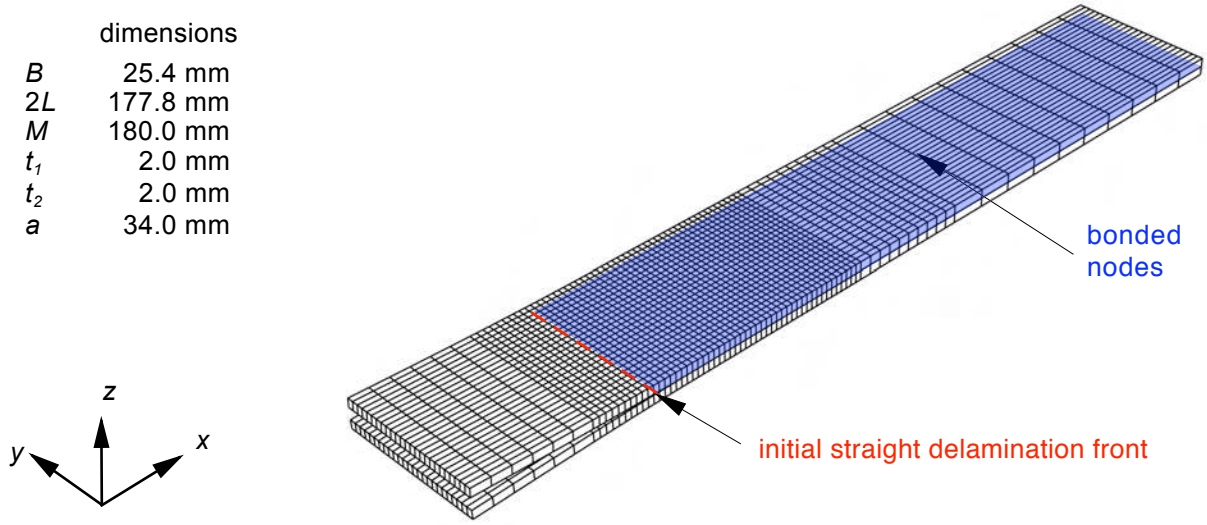

b. *Deformed model of a DCB specimen with a coarse mesh*

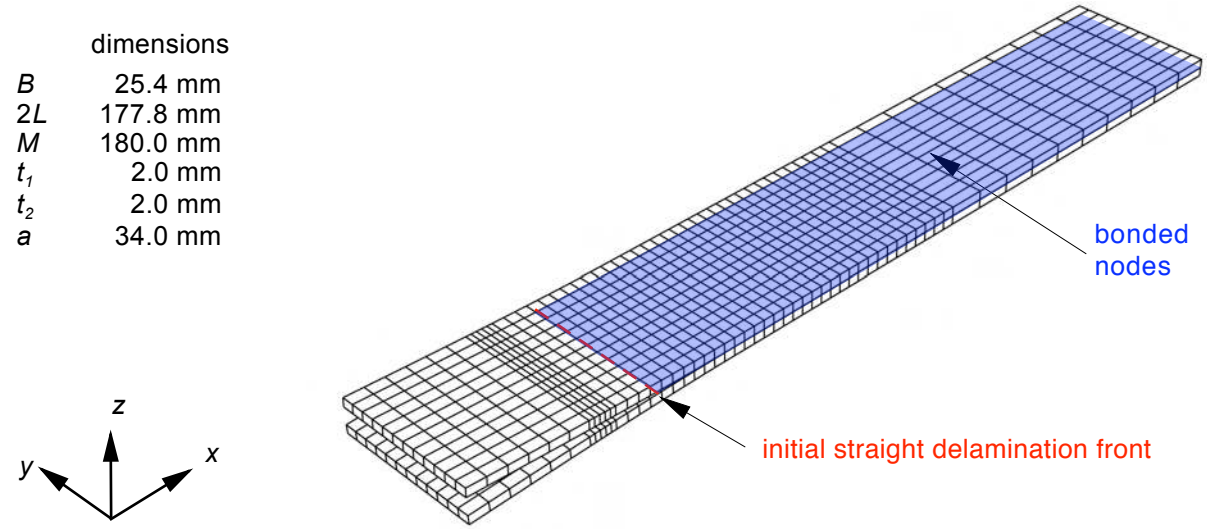

c. *Deformed model of a DCB specimen with a coarse mesh*

Figure 7. *Continuum-shell finite element models of a DCB specimen.*

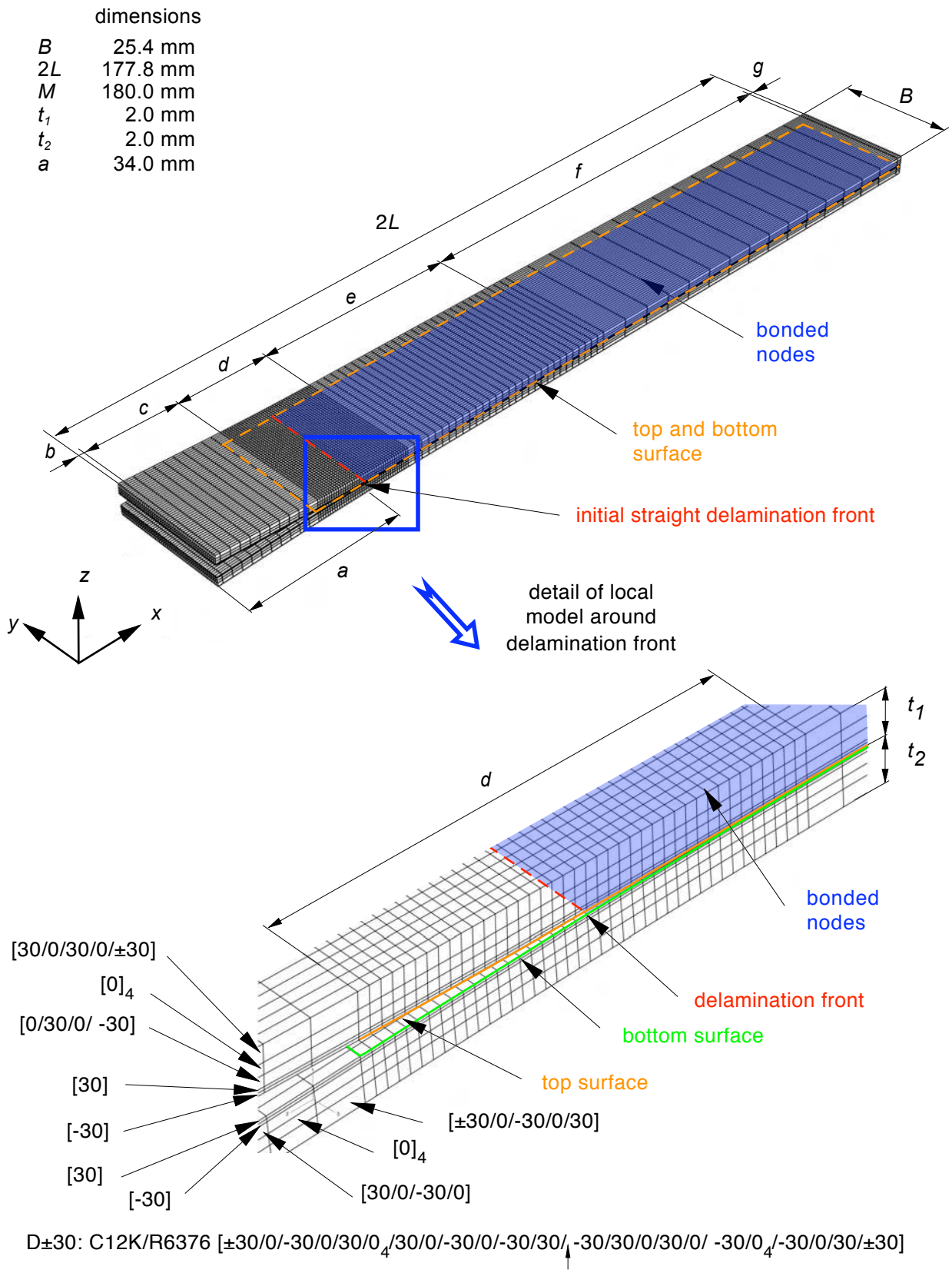

Figure 8. *Deformed model of DCB specimen and detail of region around delamination front.*

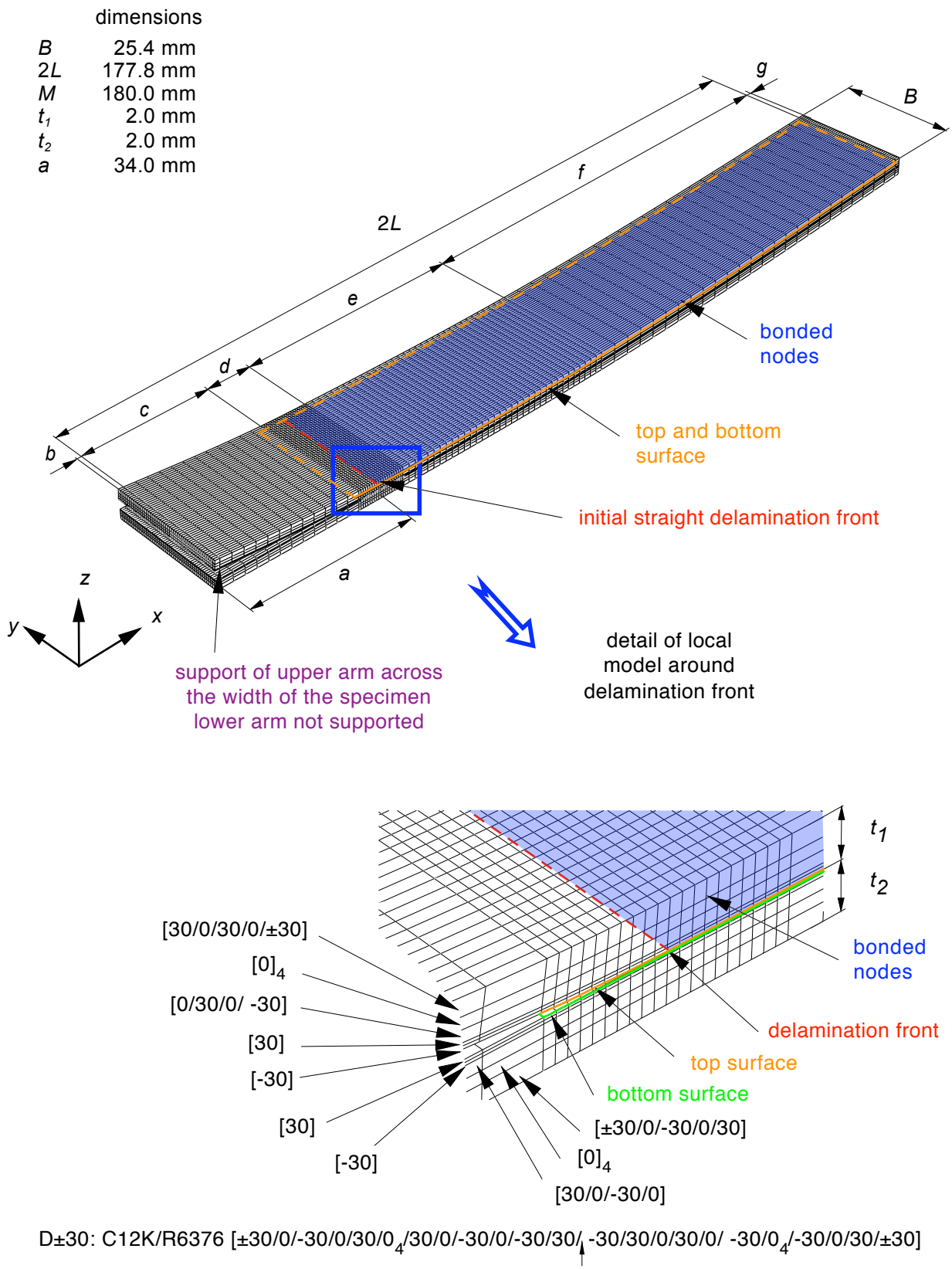

Figure 9. *Deformed model of SLB specimen and detail of region around delamination front.*

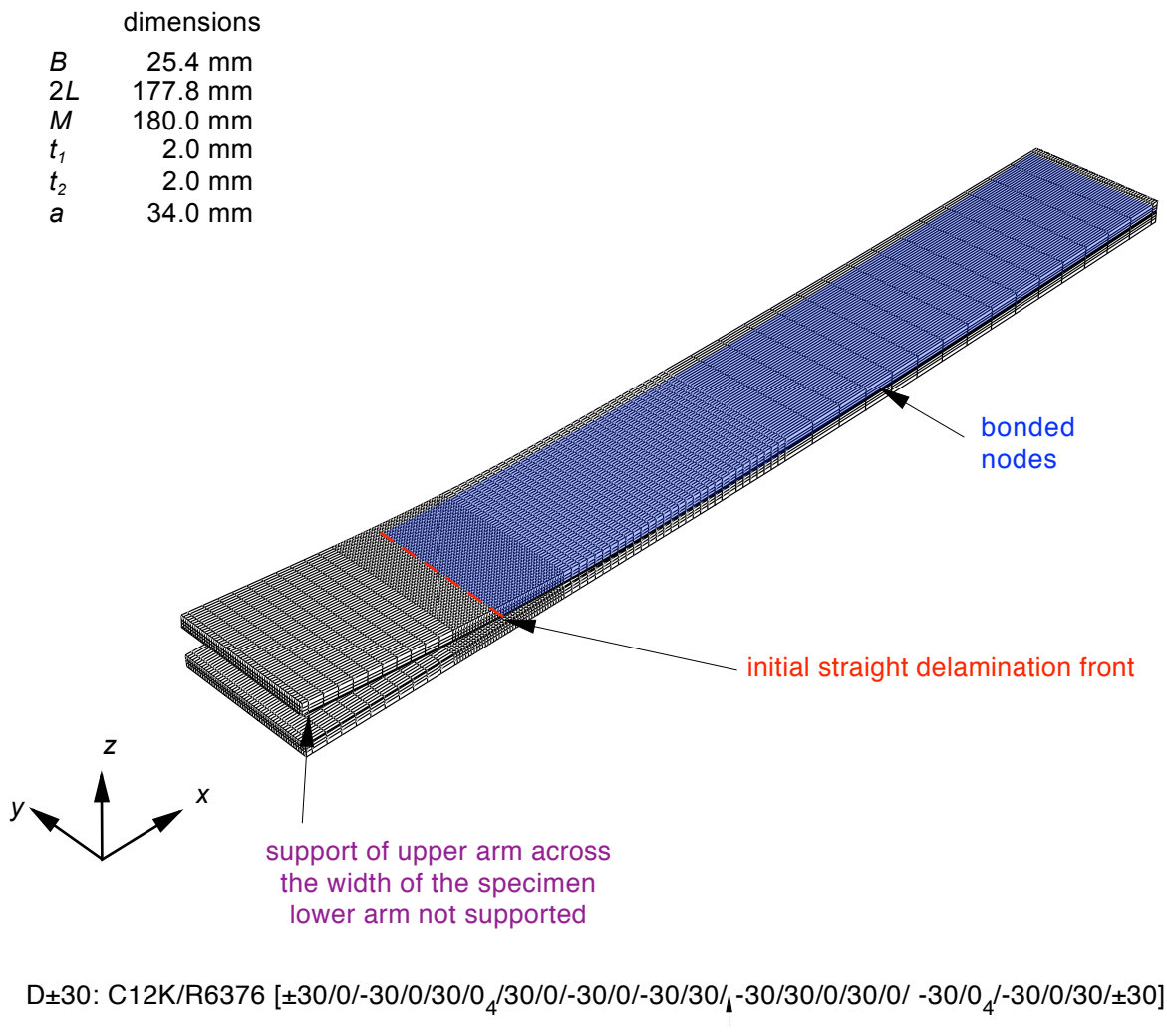

Figure 10. *Deformed model of SLB specimen with refined center section.*

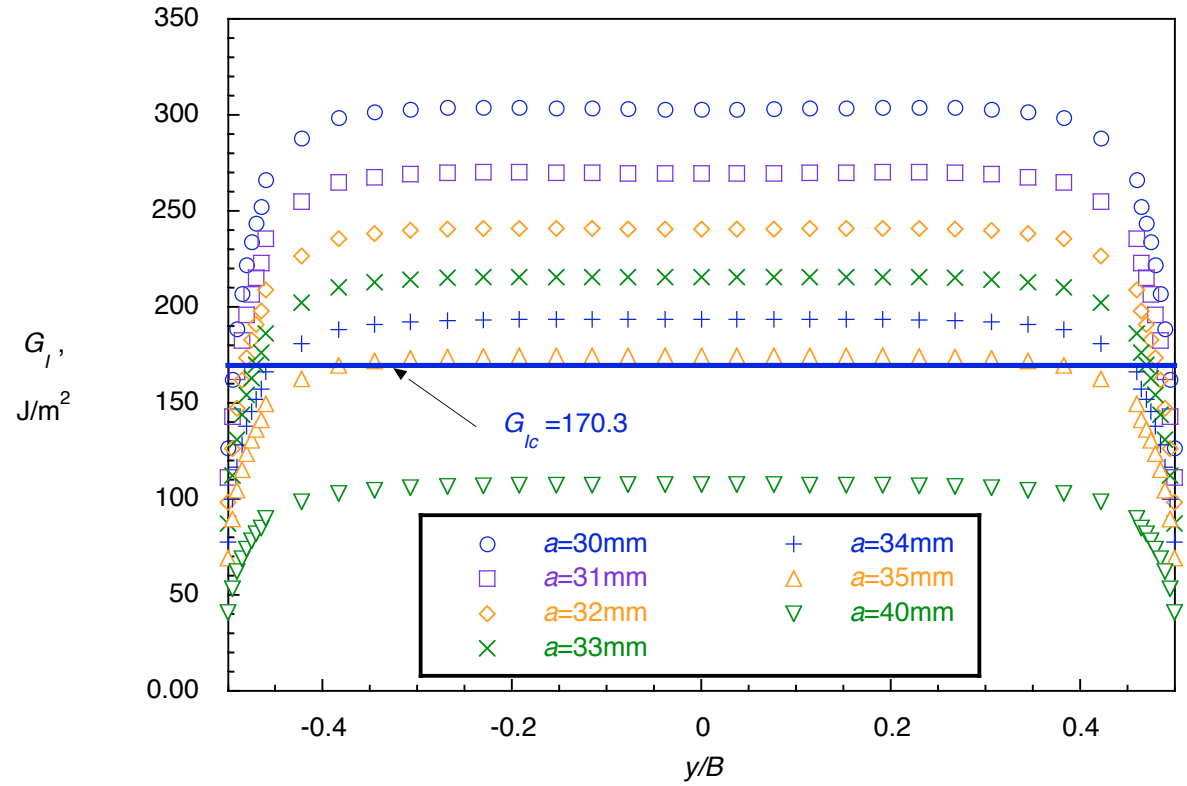

Figure 11. *Computed strain energy release rate distribution across the width of a DCB specimen (model Figure 5a).*

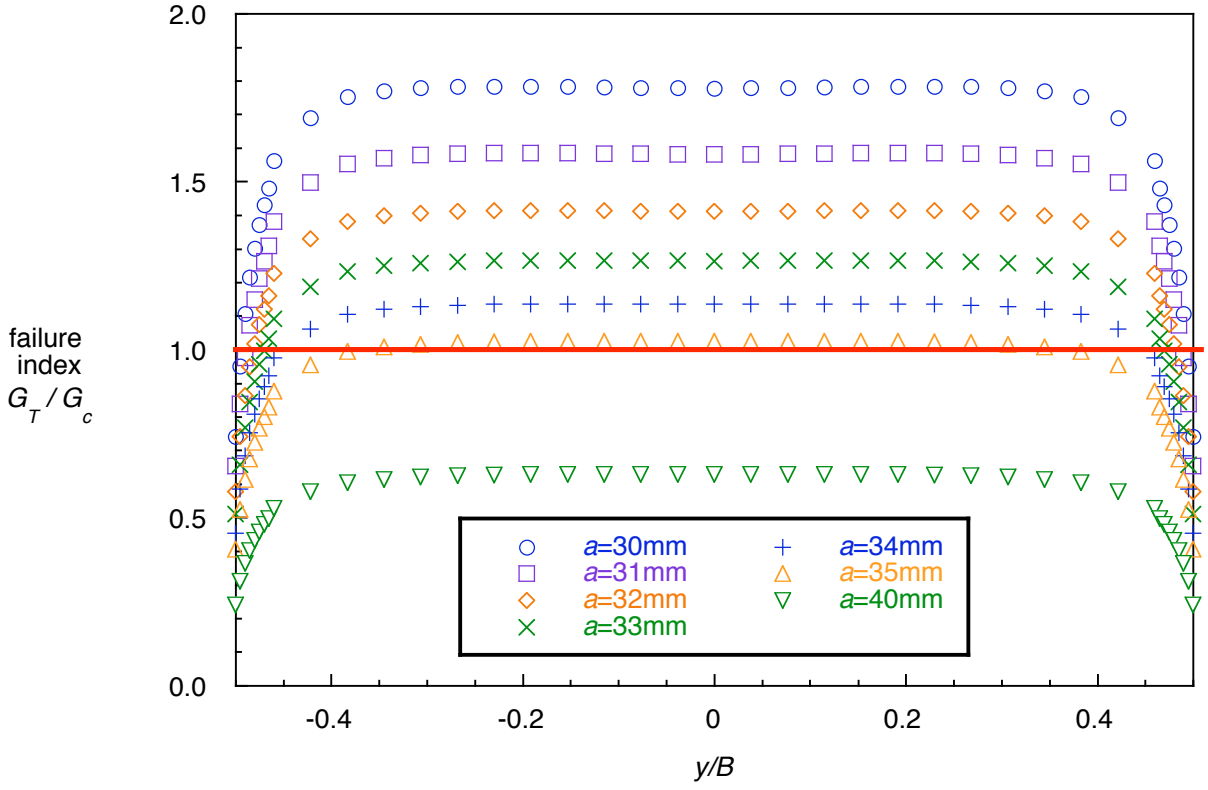

Figure 12. *Failure index distribution across the width of a DCB specimen (model Figure 5a).*

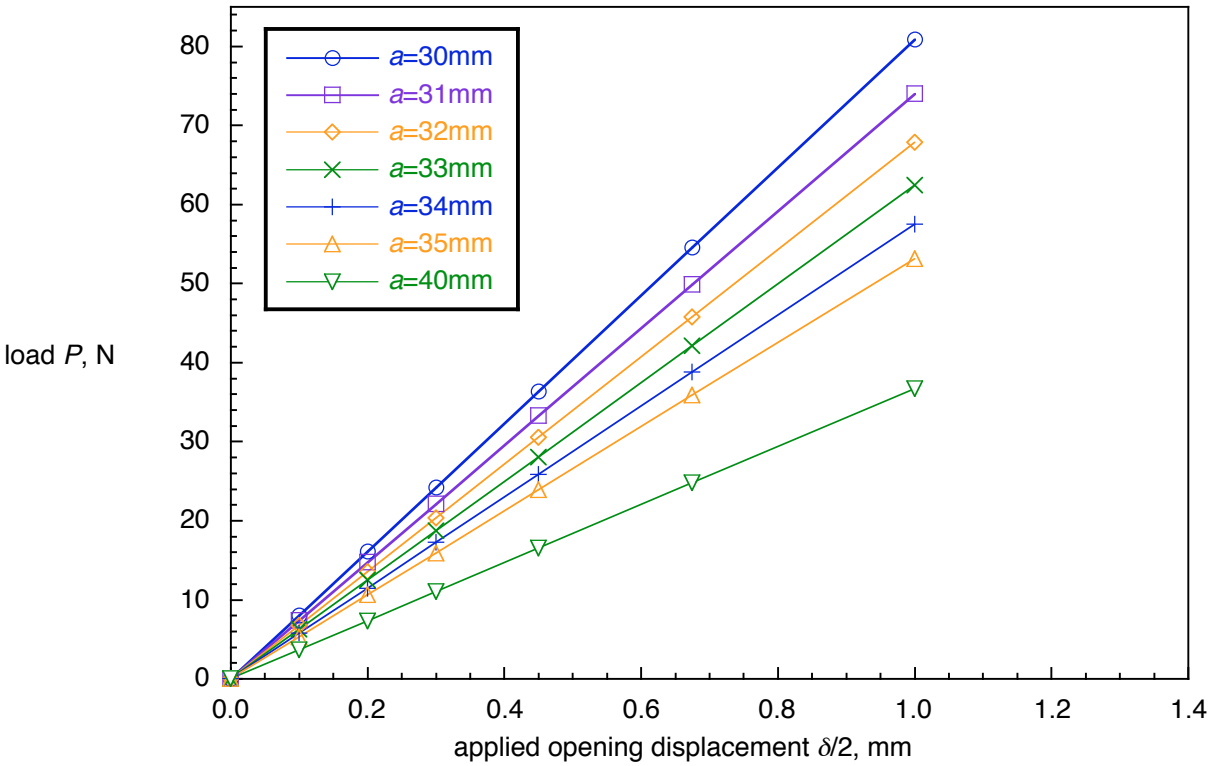

Figure 13. *Load-displacement behavior of DCB specimens with different delamination lengths a.*

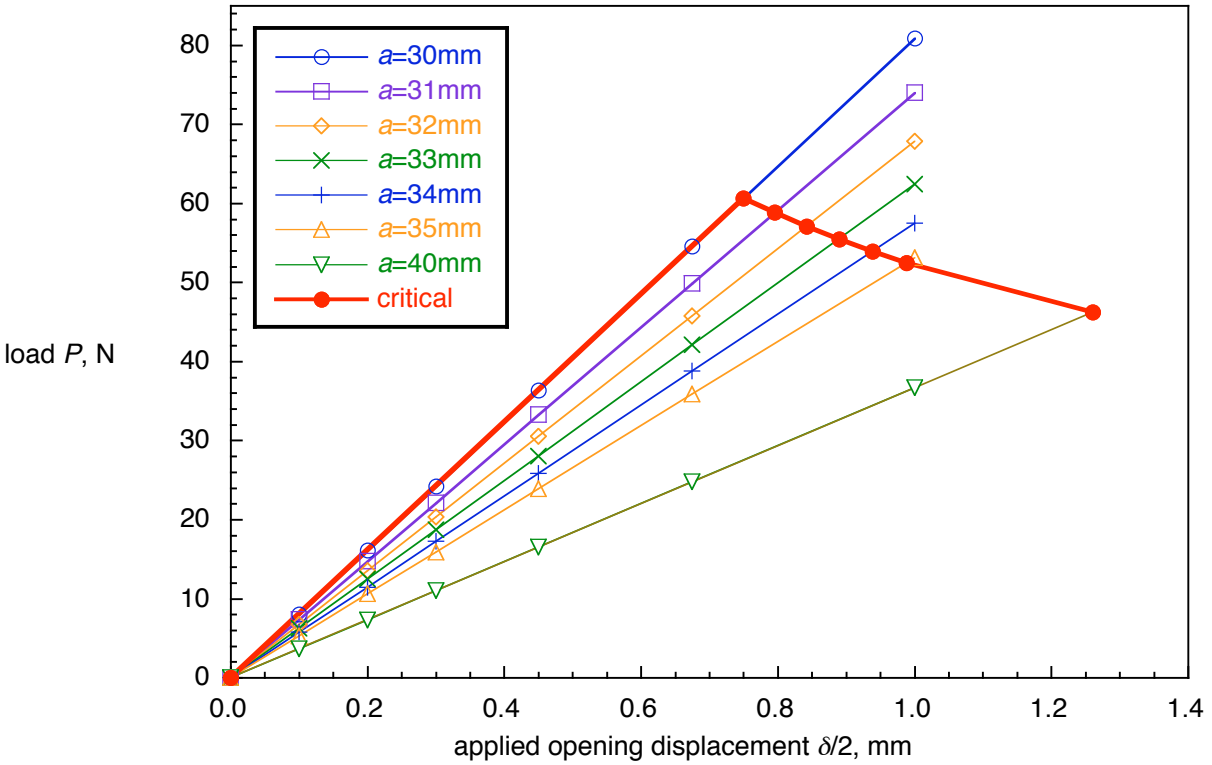

Figure 14. *Benchmark: Critical load-displacement behavior for a DCB specimen.*

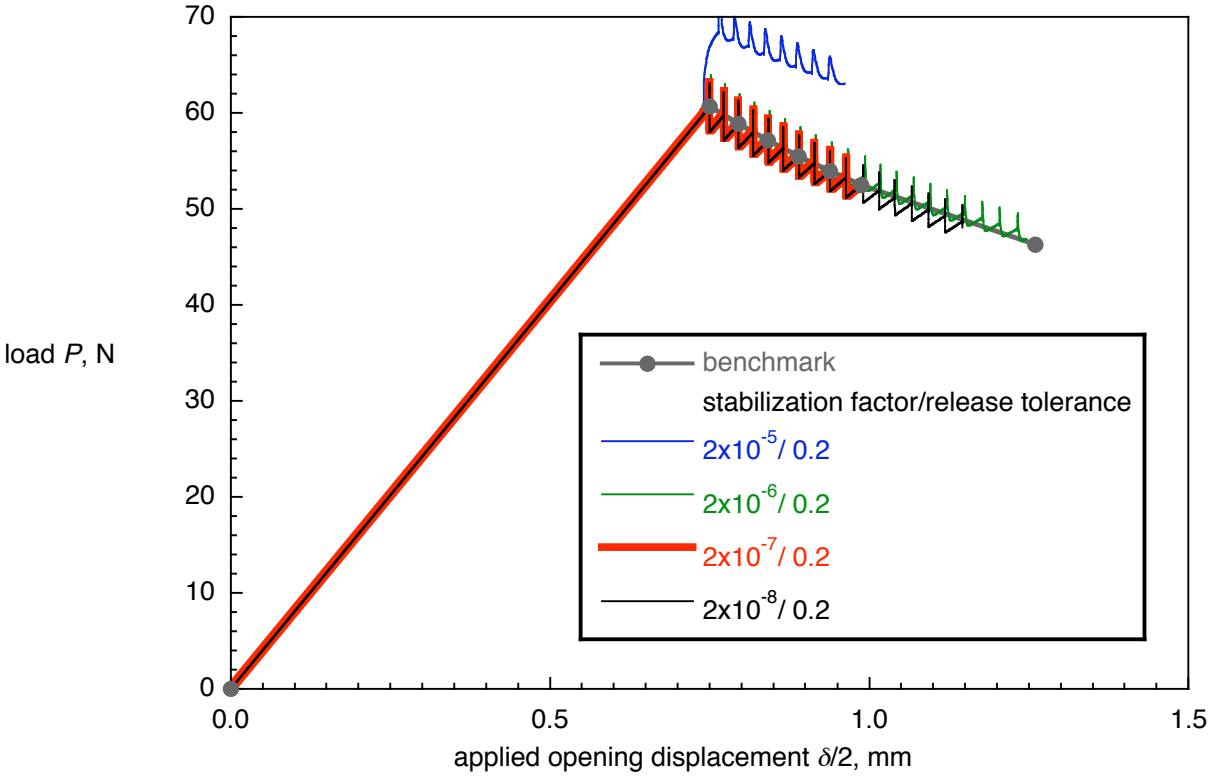

Figure 15. *VCCT for ABAQUS: Computed critical load-displacement behavior for DCB specimen obtained from results with global stabilization.*

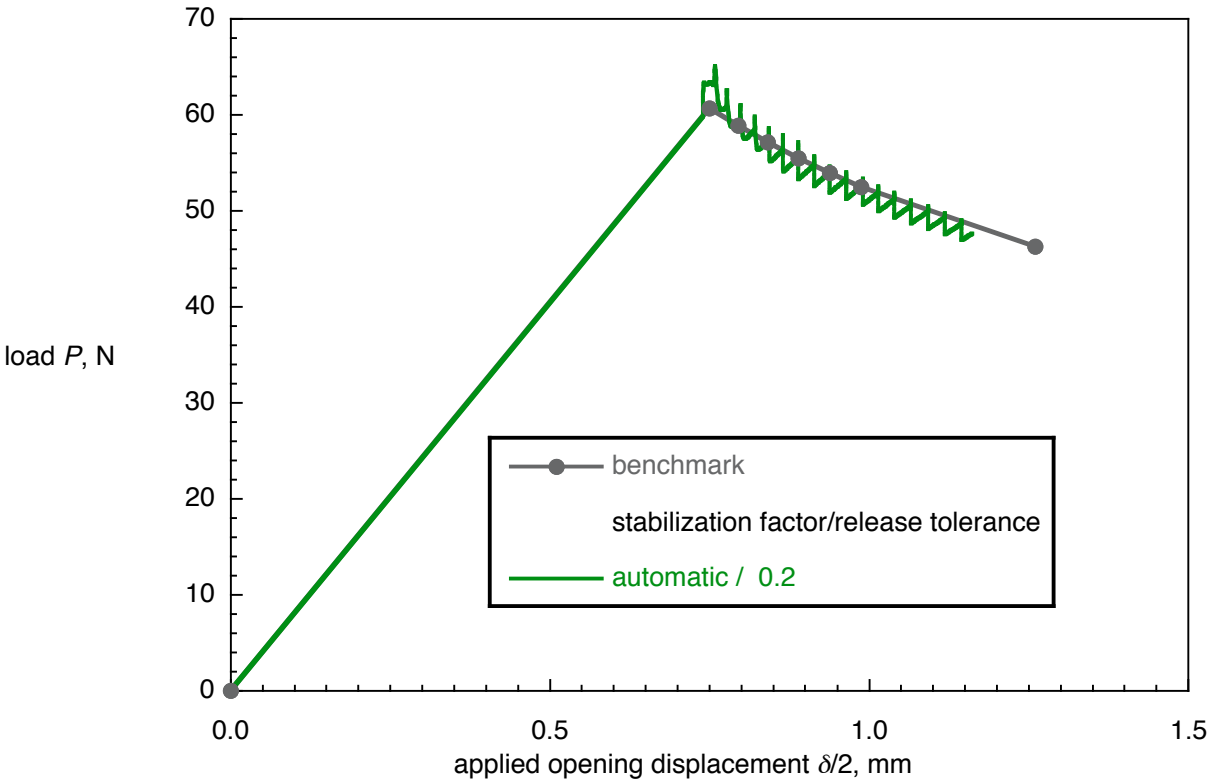

Figure 16. *VCCT for ABAQUS: Computed critical load-displacement behavior for DCB specimen obtained from results with automatic global stabilization.*

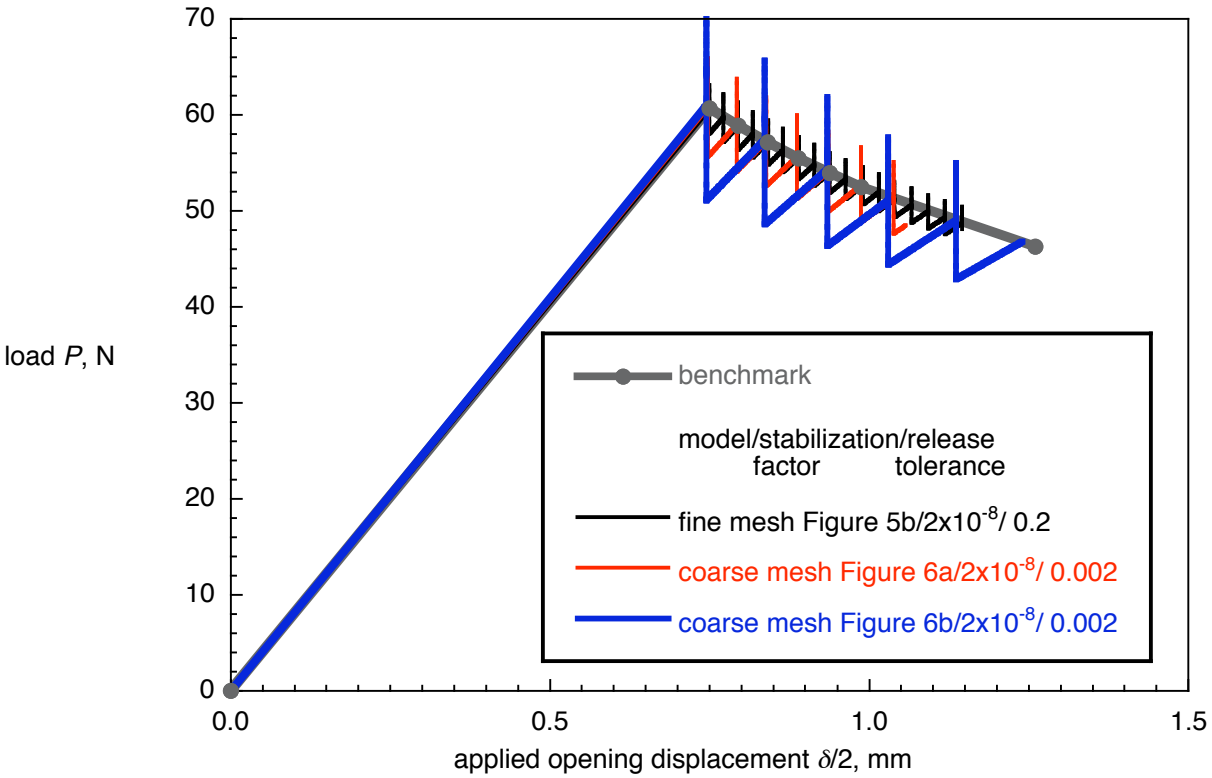

Figure 17. *VCCT for ABAQUS: Computed critical load-displacement behavior for DCB specimen obtained from results with global stabilization.*

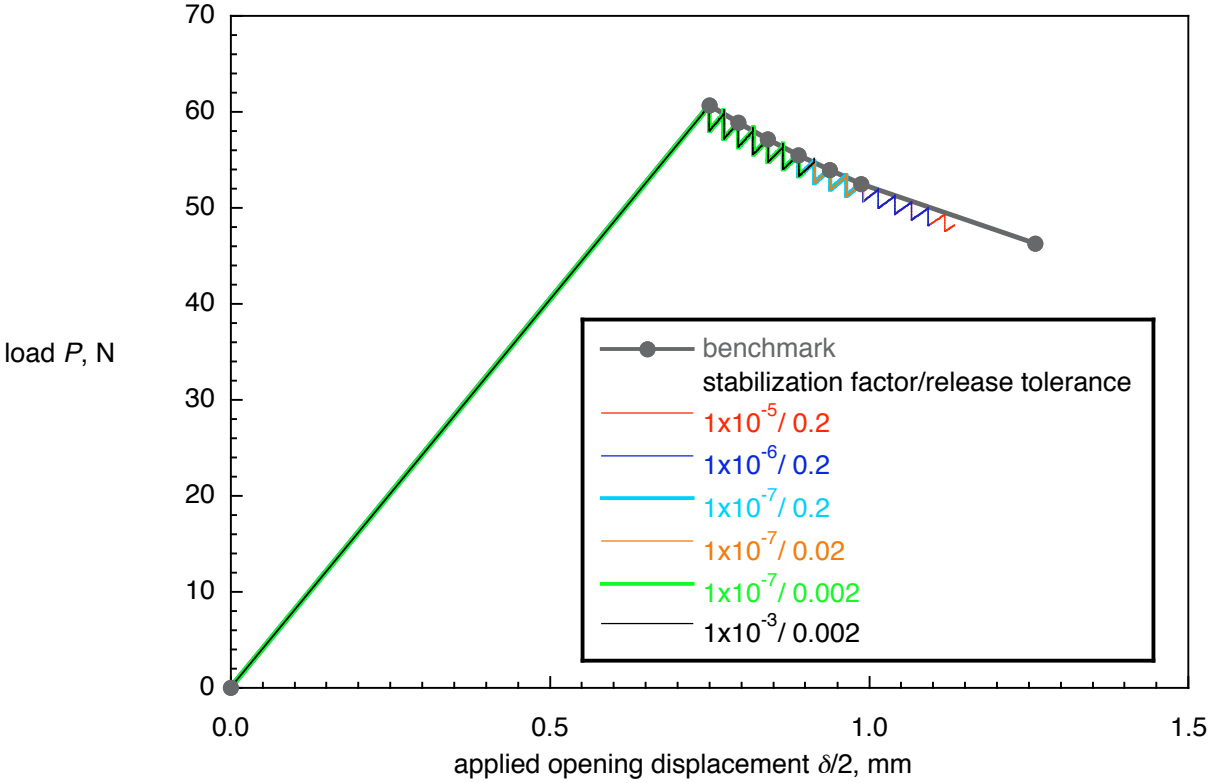

Figure 18. *Computed critical load-displacement behavior for DCB specimen obtained from results with contact stabilization.*

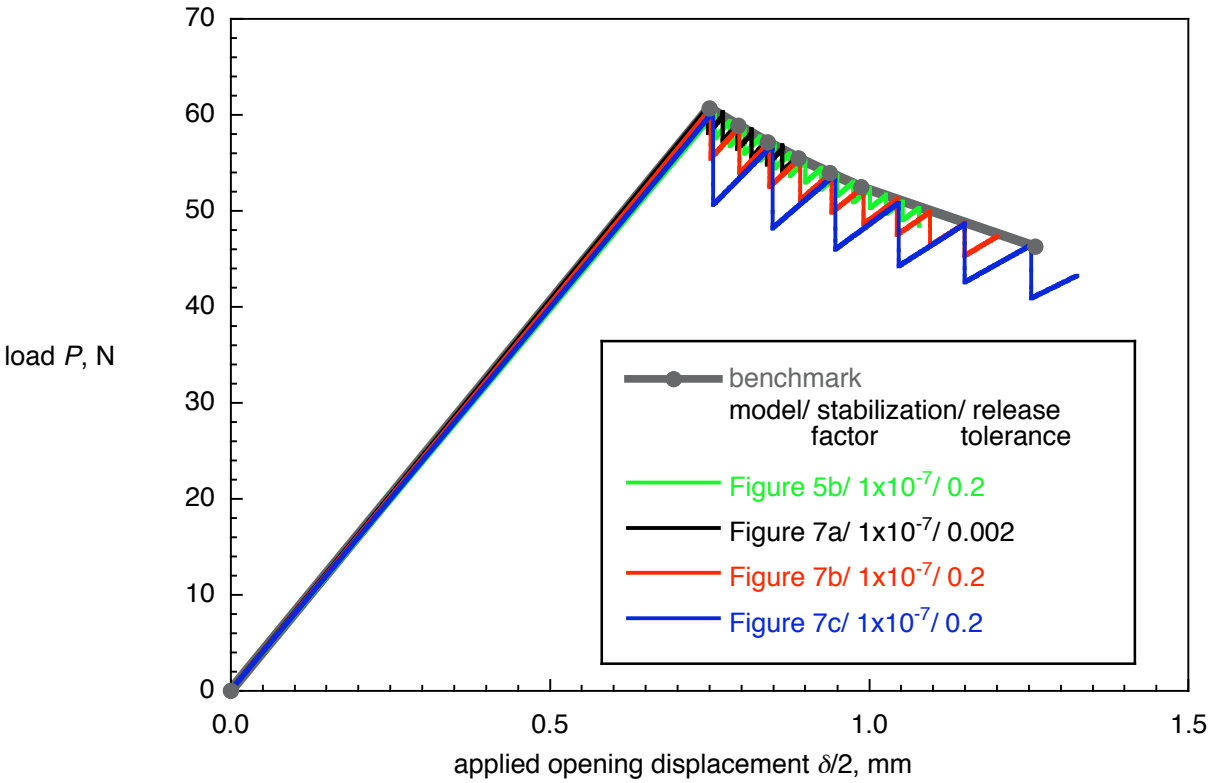

Figure 19. *VCCT for ABAQUS: Computed critical load-displacement behavior for DCB specimen obtained from results with contact stabilization.*

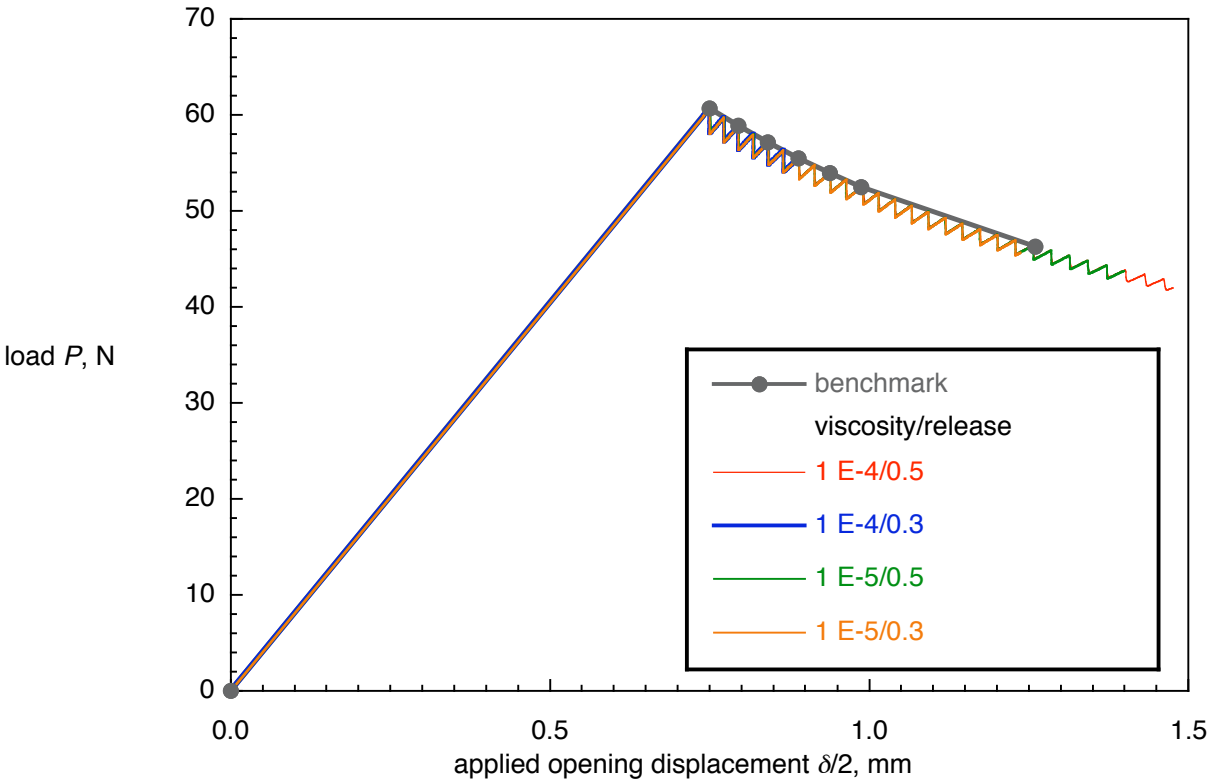

Figure 20. *Computed critical load-displacement behavior for DCB specimen obtained from results with viscous regularization.*

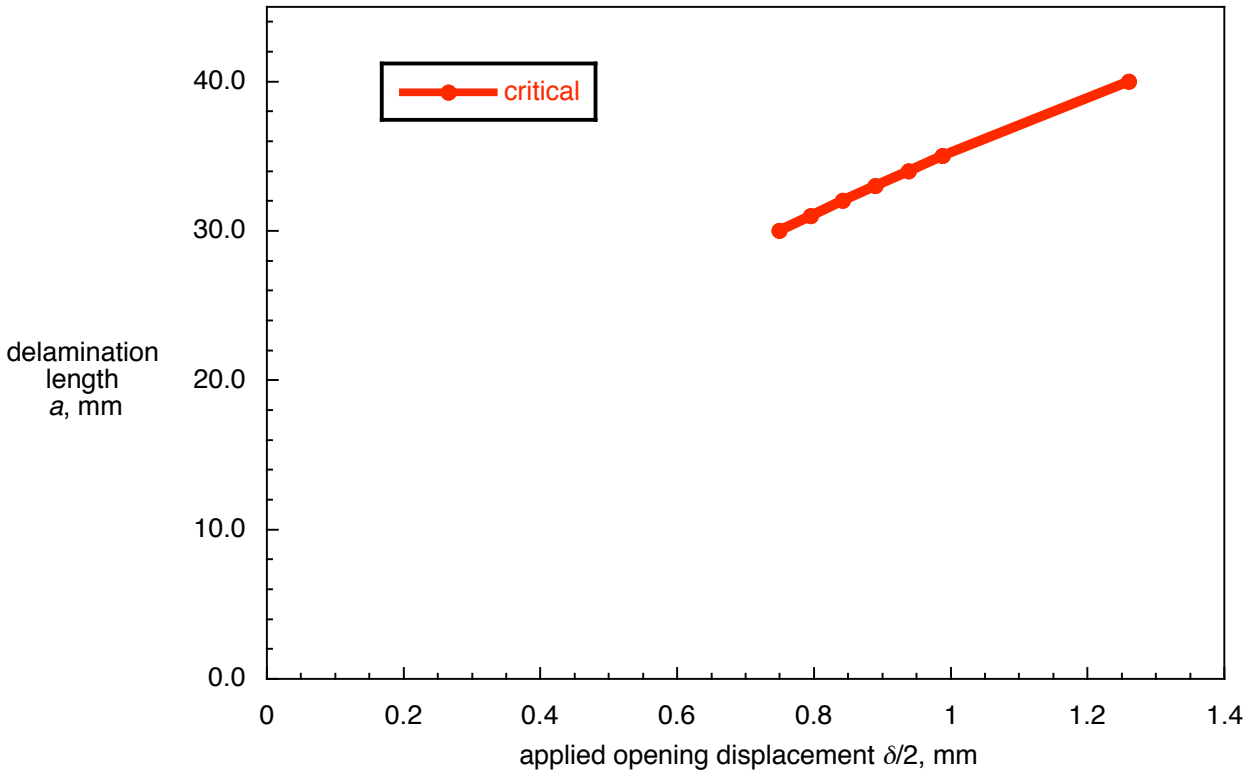

Figure 21. *Critical delamination length-displacement behavior for DCB specimen.*

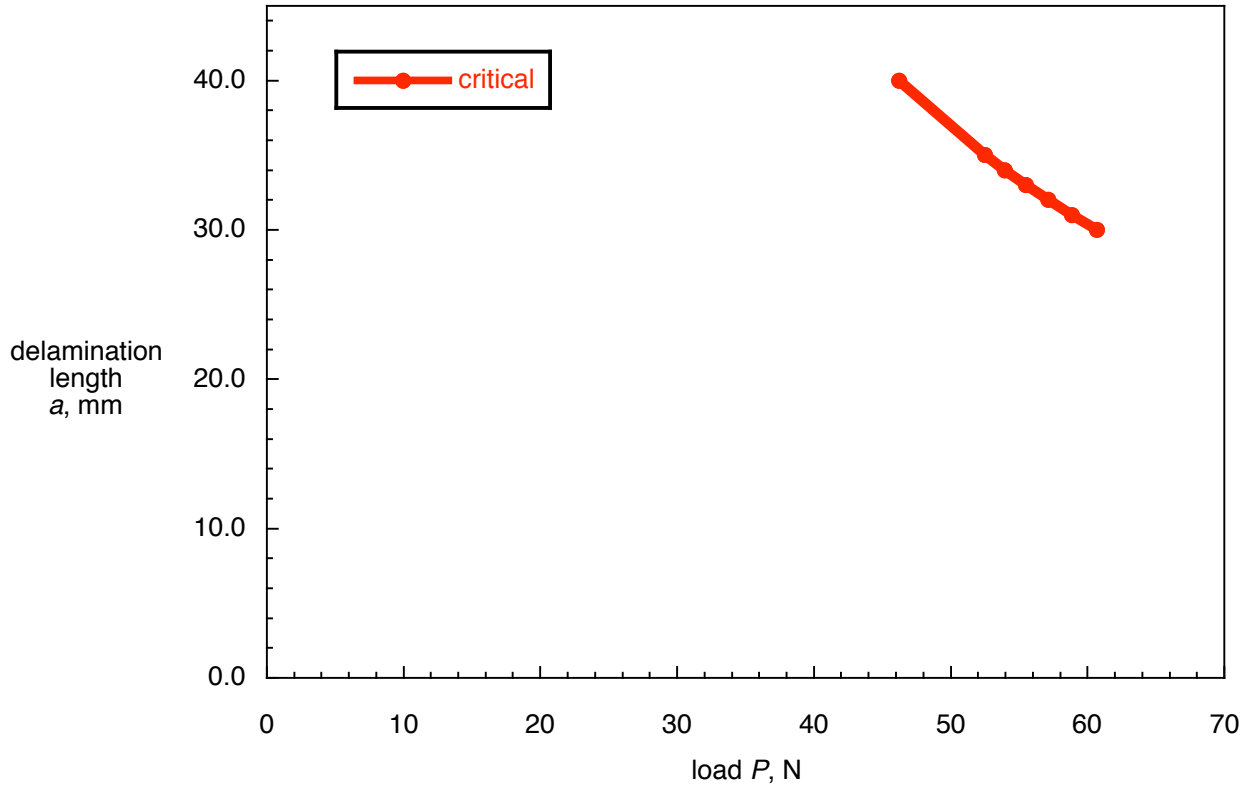

Figure 22. *Computed critical delamination length-load behavior for DCB specimen.*

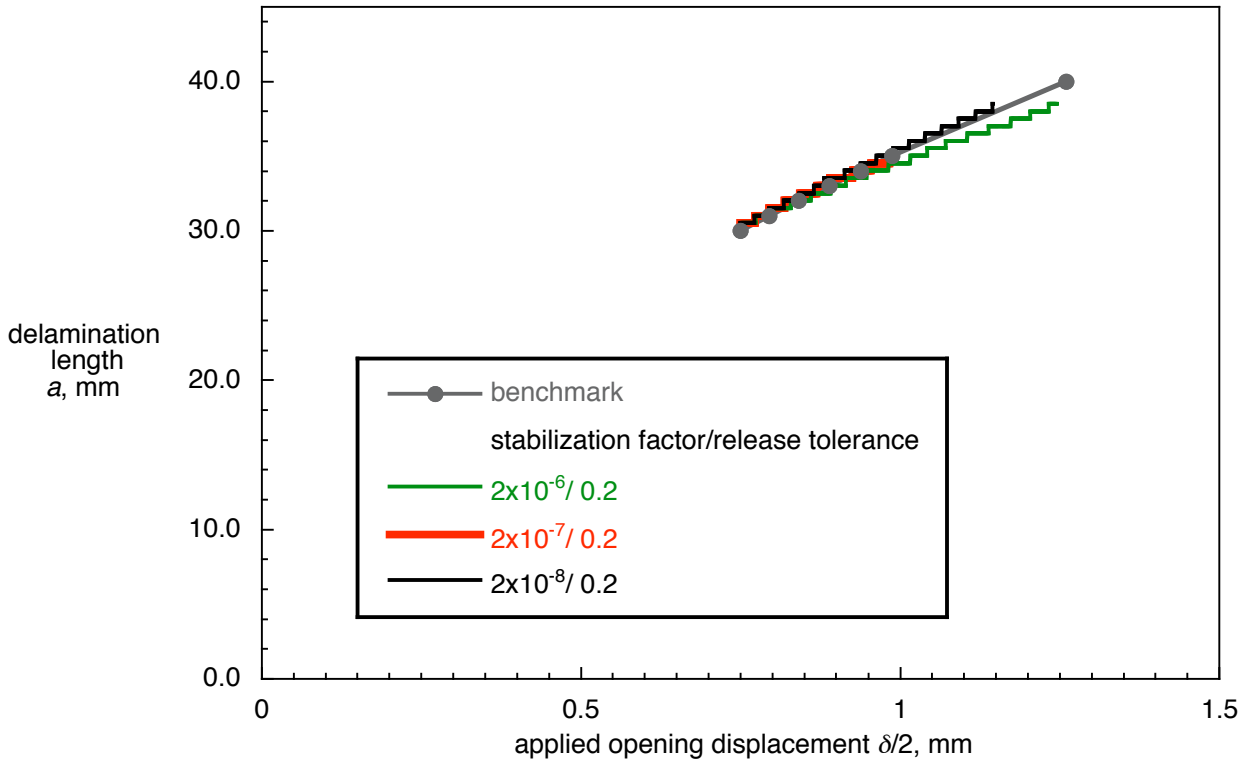

Figure 23. *Computed critical delamination length-displacement behavior for DCB specimen obtained from results with global stabilization.*

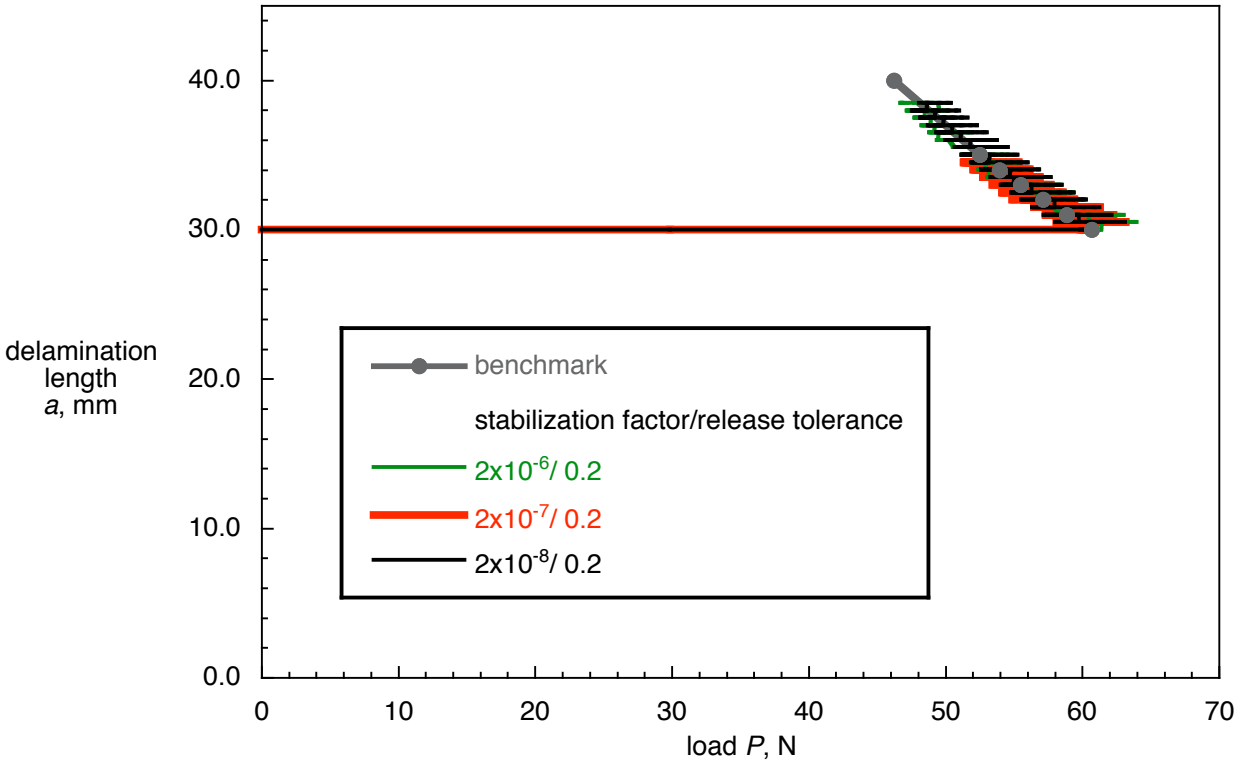

Figure 24. *Computed critical delamination length-load behavior for DCB specimen obtained from results with global stabilization.*

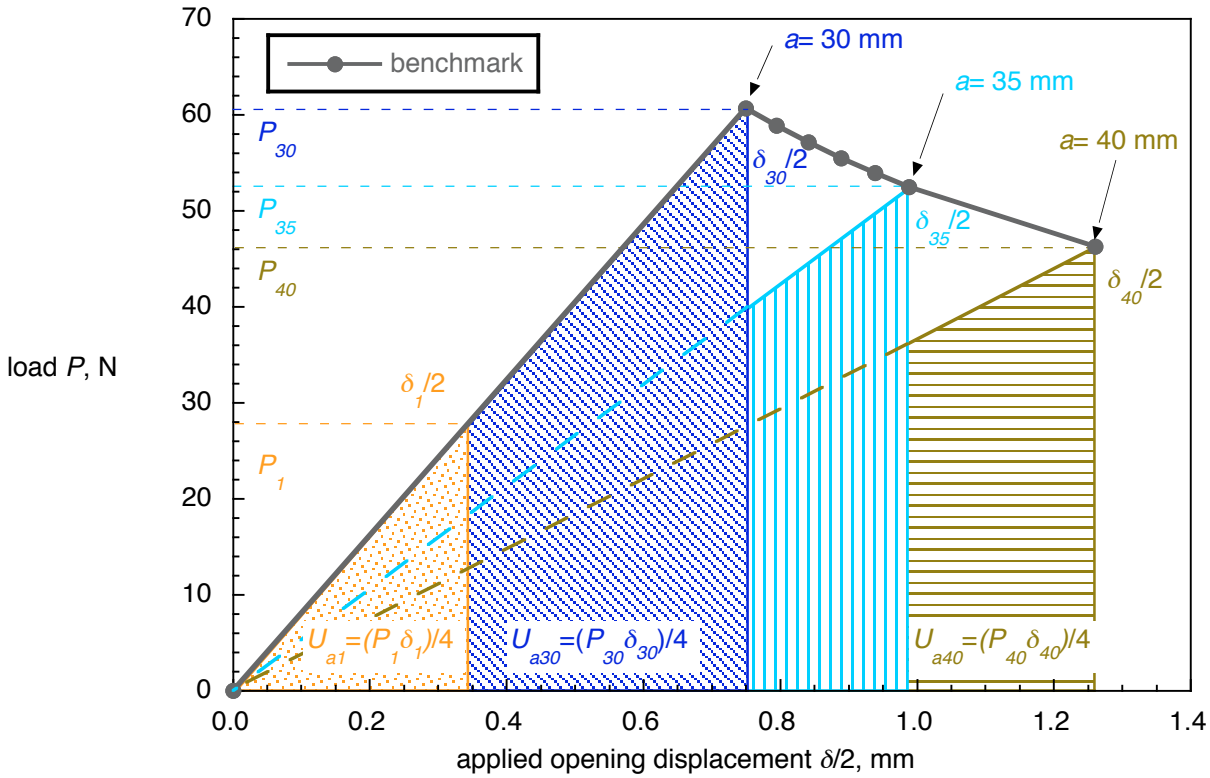

Figure 25. *Total energy calculation for DCB specimen.*

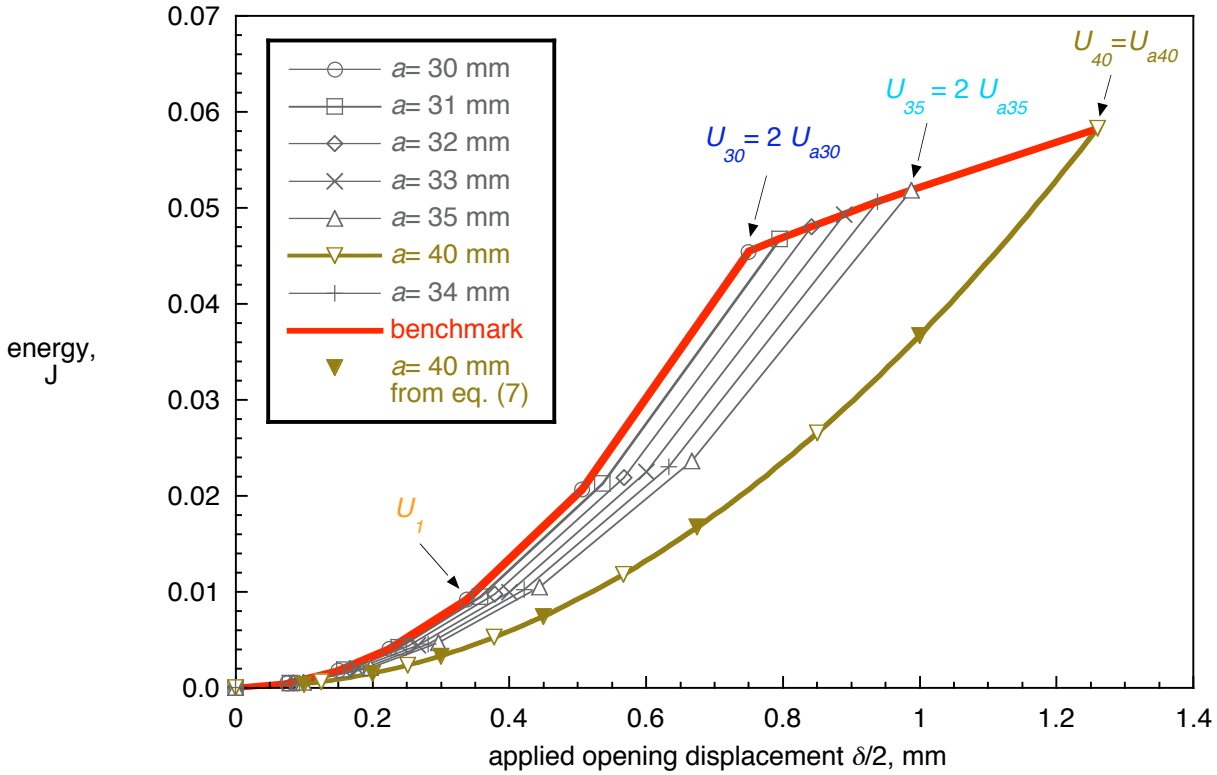

Figure 26. *Calculated total strain energy in the model for DCB specimen (model in Figure 7a).*

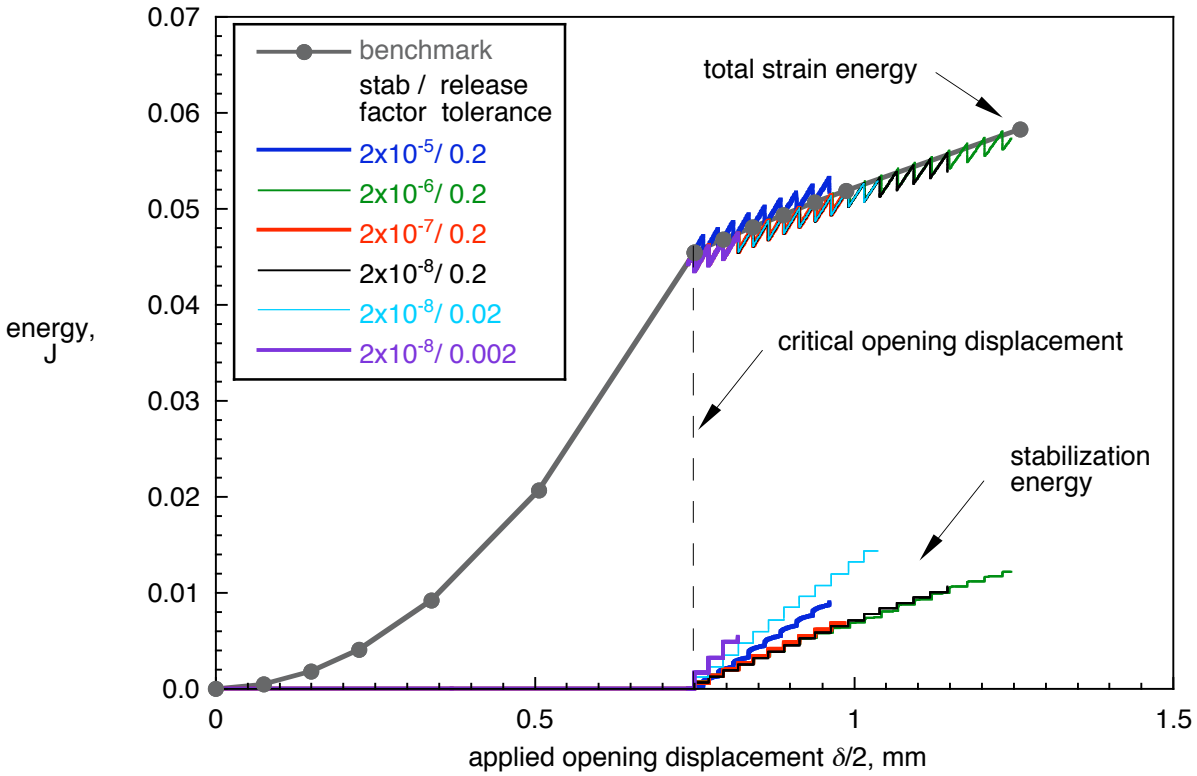

Figure 27. *Computed total strain energy and stabilization energy in the model of a DCB specimen obtained from results with global stabilization.*

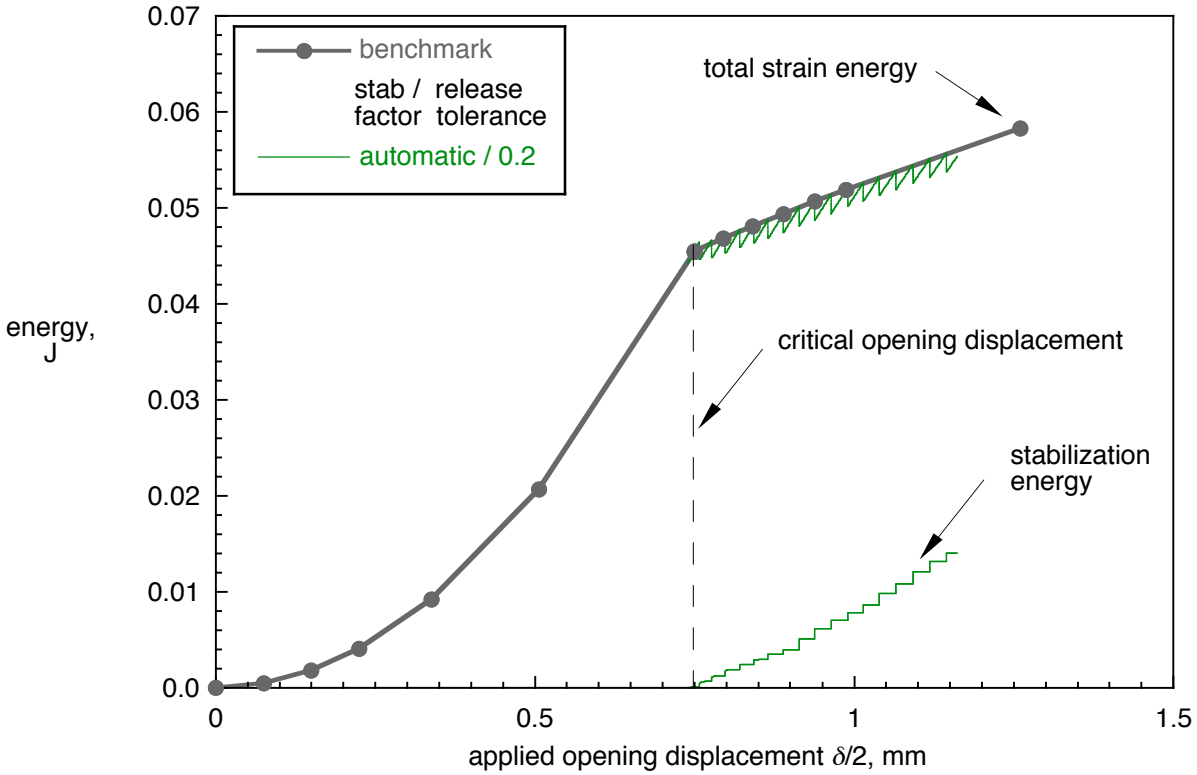

Figure 28. *Computed total strain energy and stabilization energy in the model of a DCB specimen obtained from results with automatic global stabilization.*

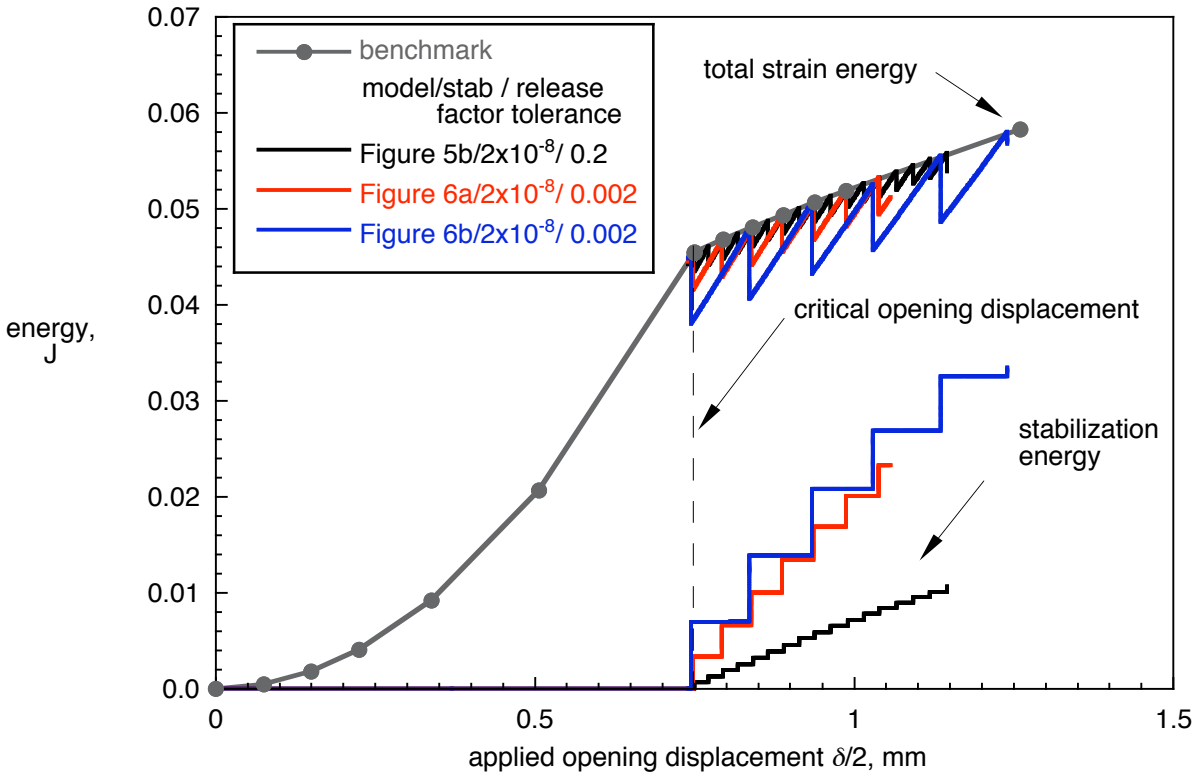

Figure 29. *Computed total strain energy and stabilization energy in the model of a DCB specimen obtained from results with global stabilization.*

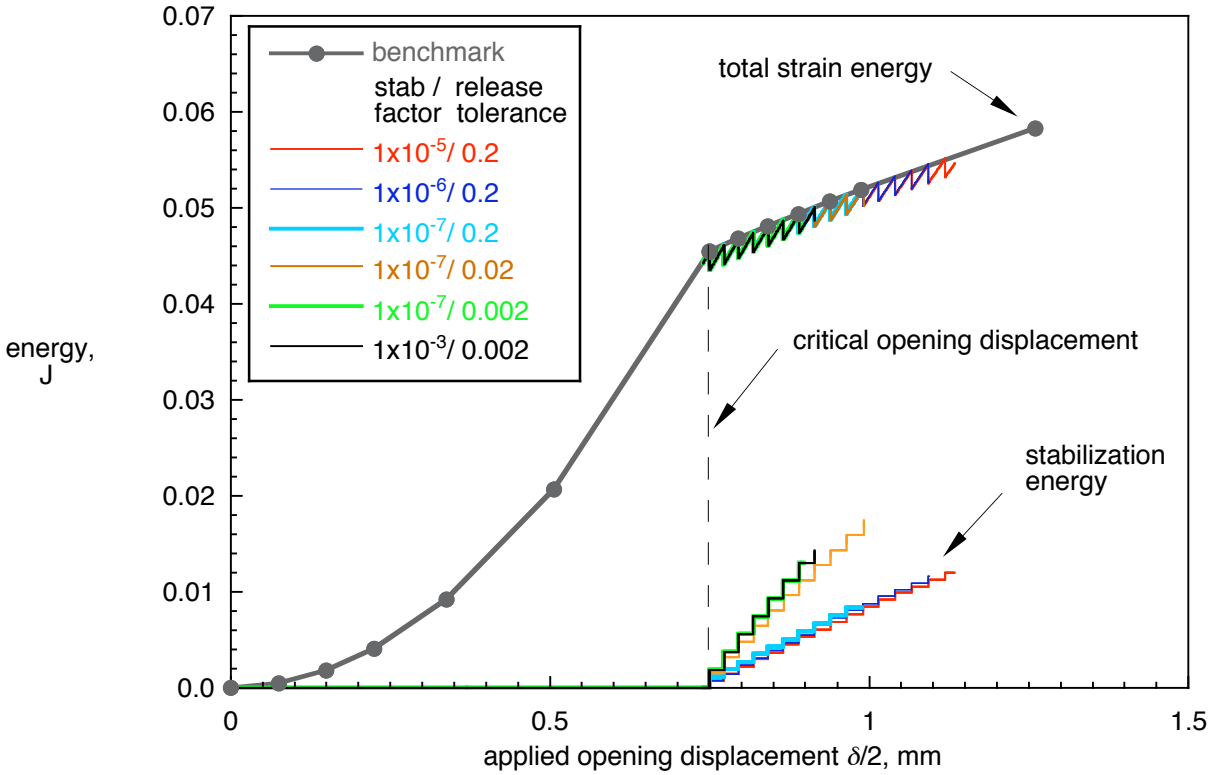

Figure 30. *Computed total strain energy and stabilization energy in the model of a DCB specimen obtained from results with contact stabilization.*

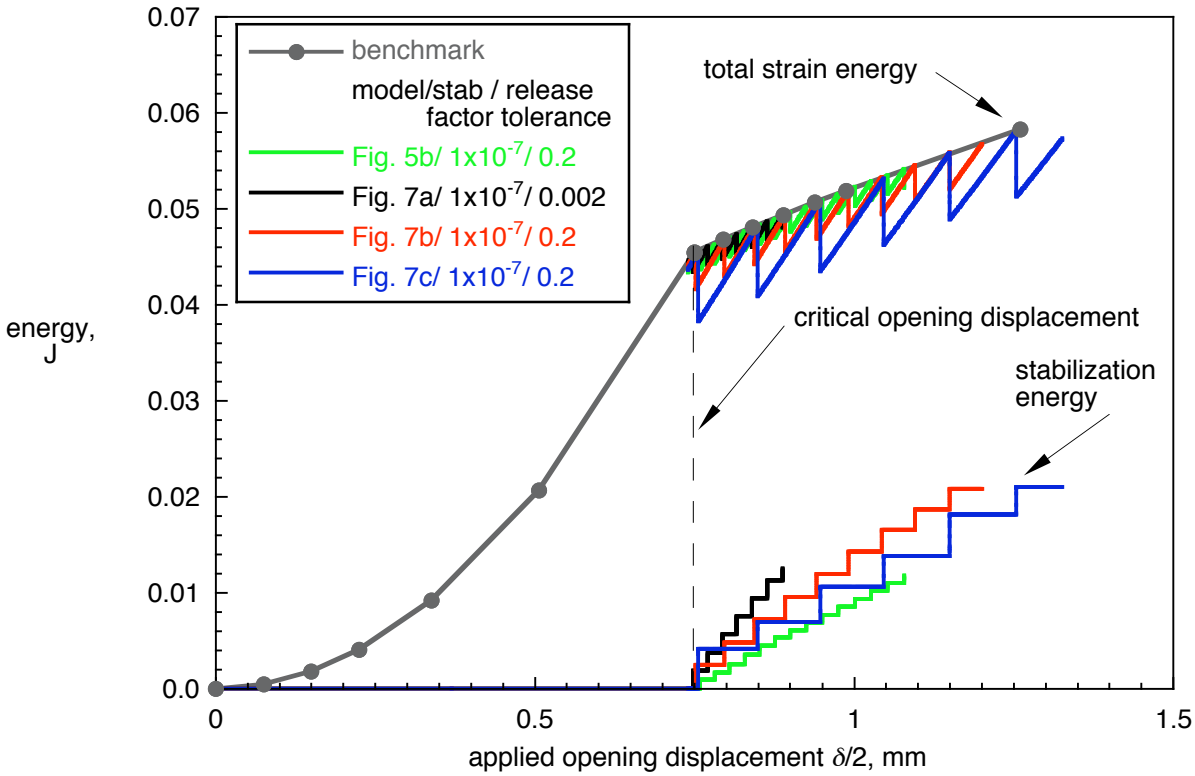

Figure 31. *Computed total strain energy and stabilization energy in the model of a DCB specimen obtained from results with contact stabilization.*

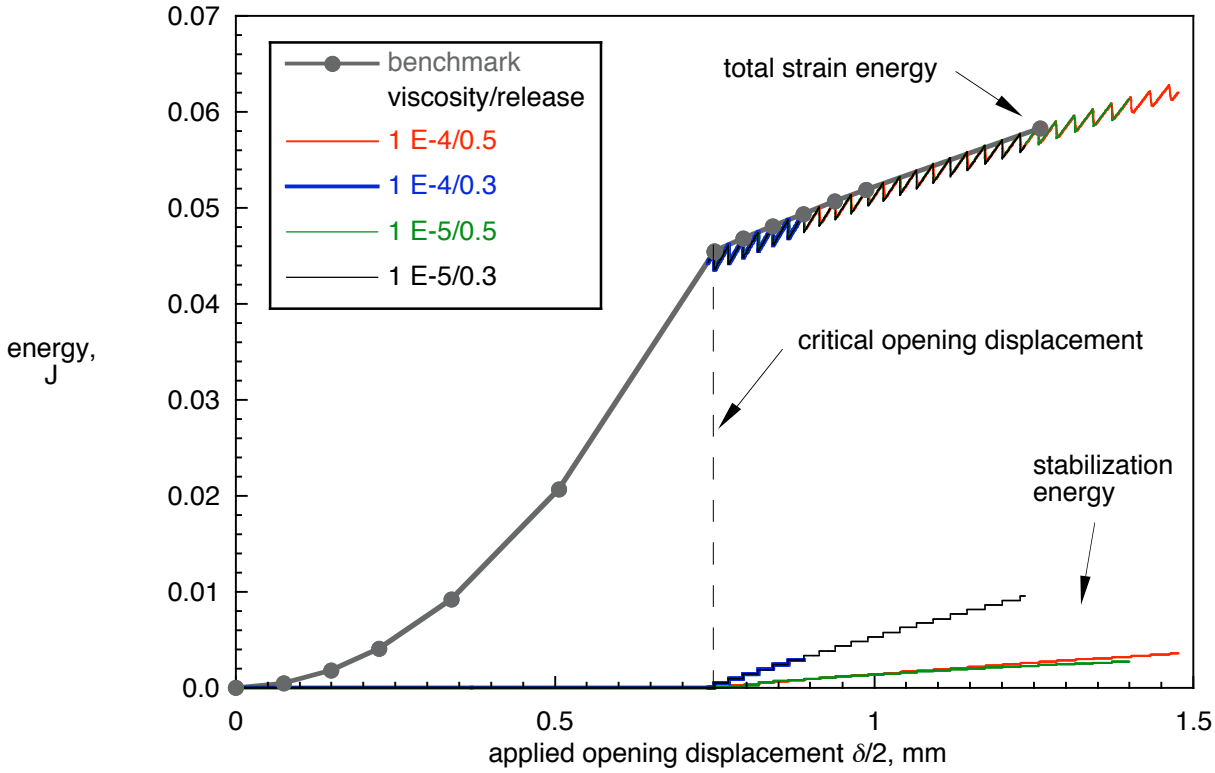

Figure 32. *Computed total strain energy and stabilization energy in the model of a DCB specimen obtained from results with viscous regularization.*

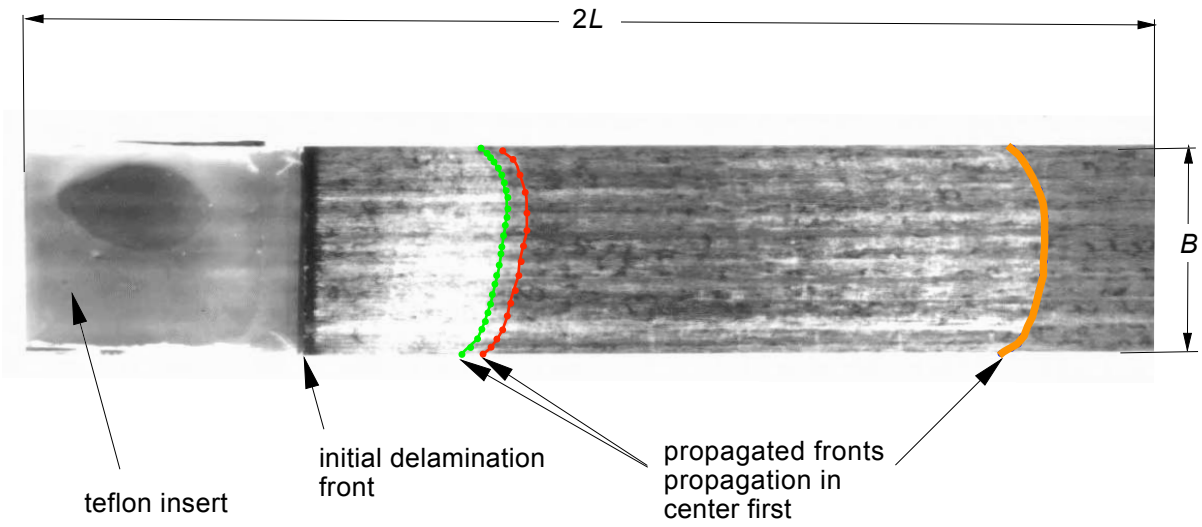

a. *Scan of fractured DCB specimen*

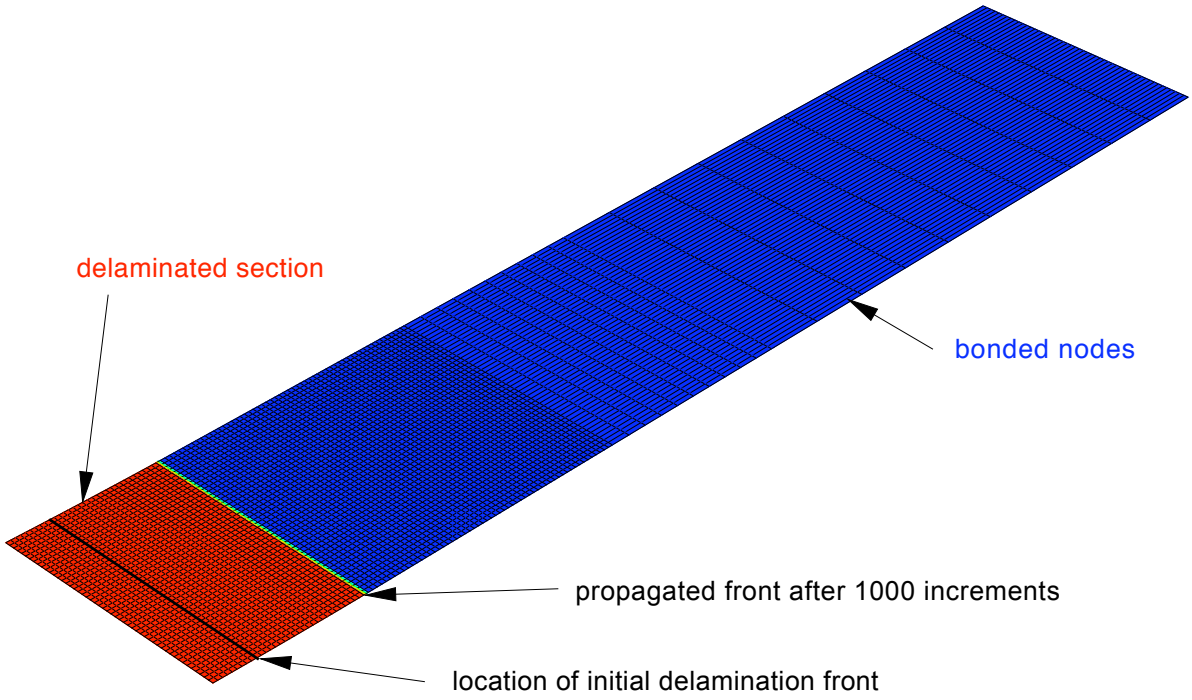

b. *Delamination front after 1000 increments (Bottom surface of FE model in Figure 4b)*

Figure 33. *Delamination front shape for a DCB specimen.*

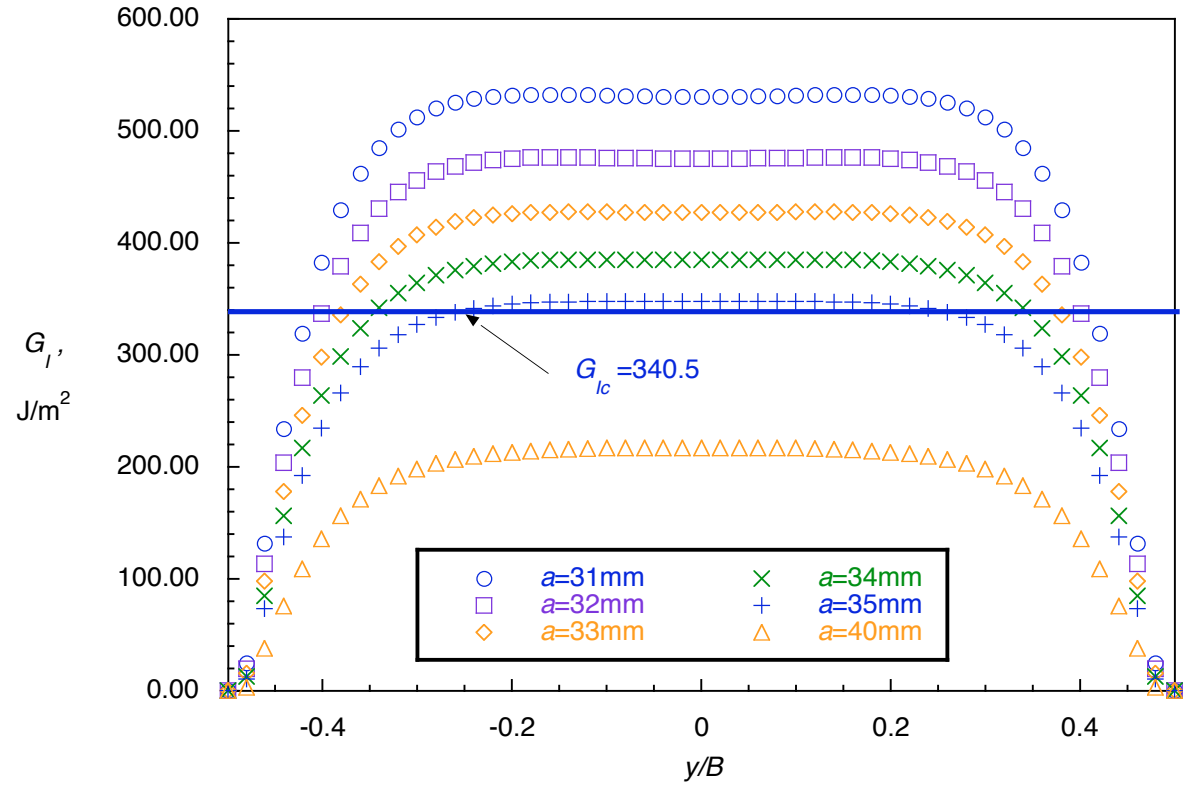

Figure 34. *Computed strain energy release rate distribution across the width of a multidirectional DCB specimen.*

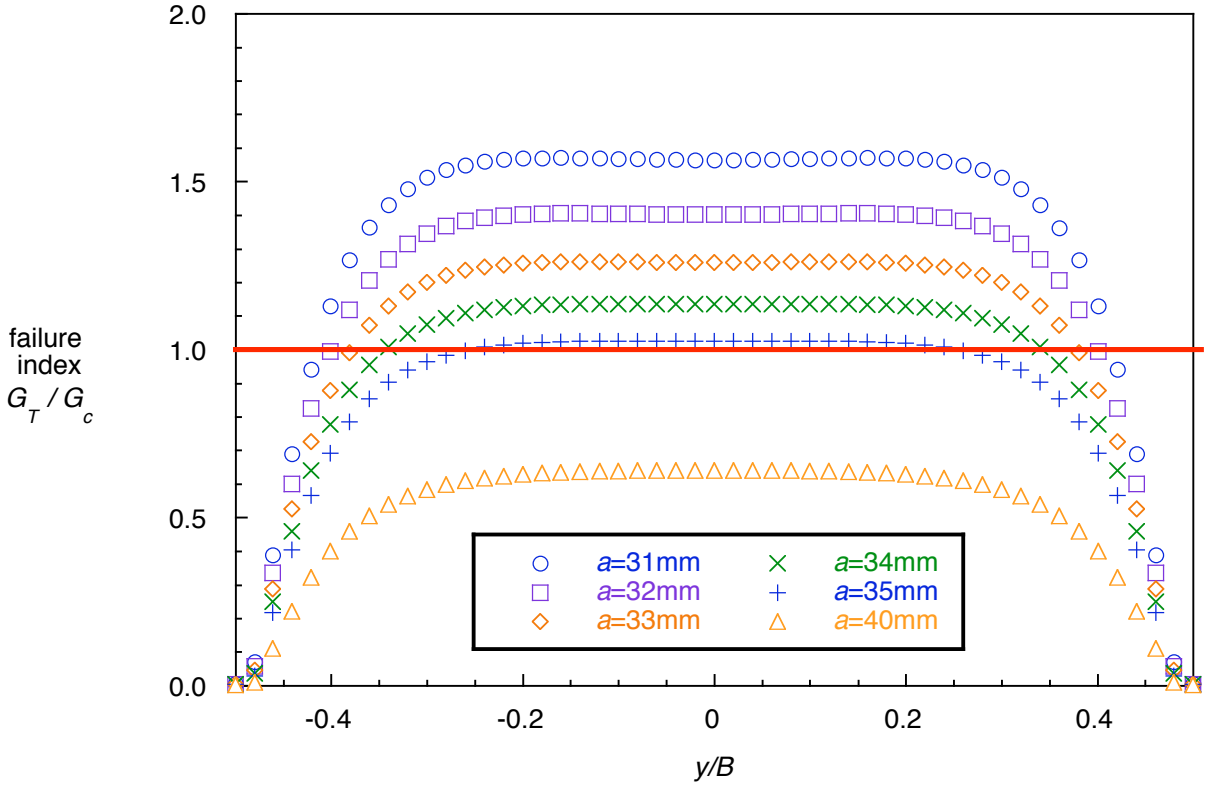

Figure 35. *Failure index distribution across the width of a multidirectinal DCB specimen.*

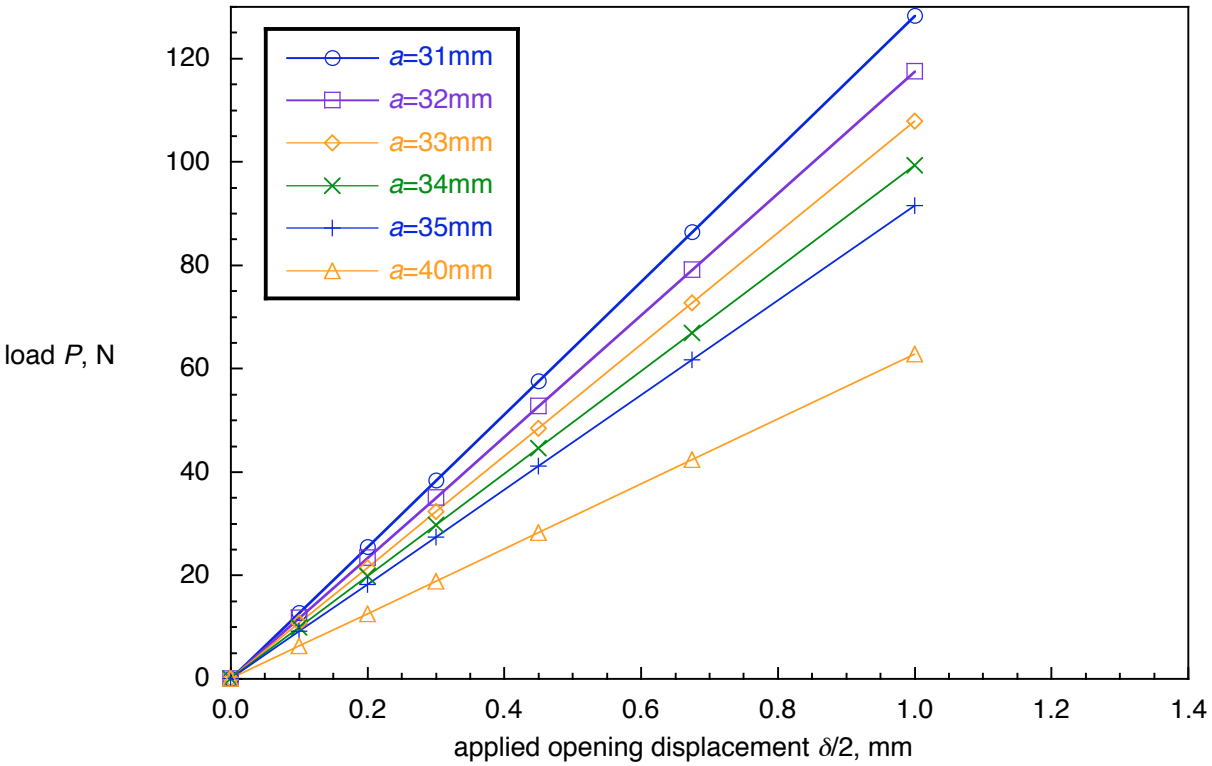

Figure 36. *Load-displacement behavior of multidirectional DCB specimens with different delamination lengths a*

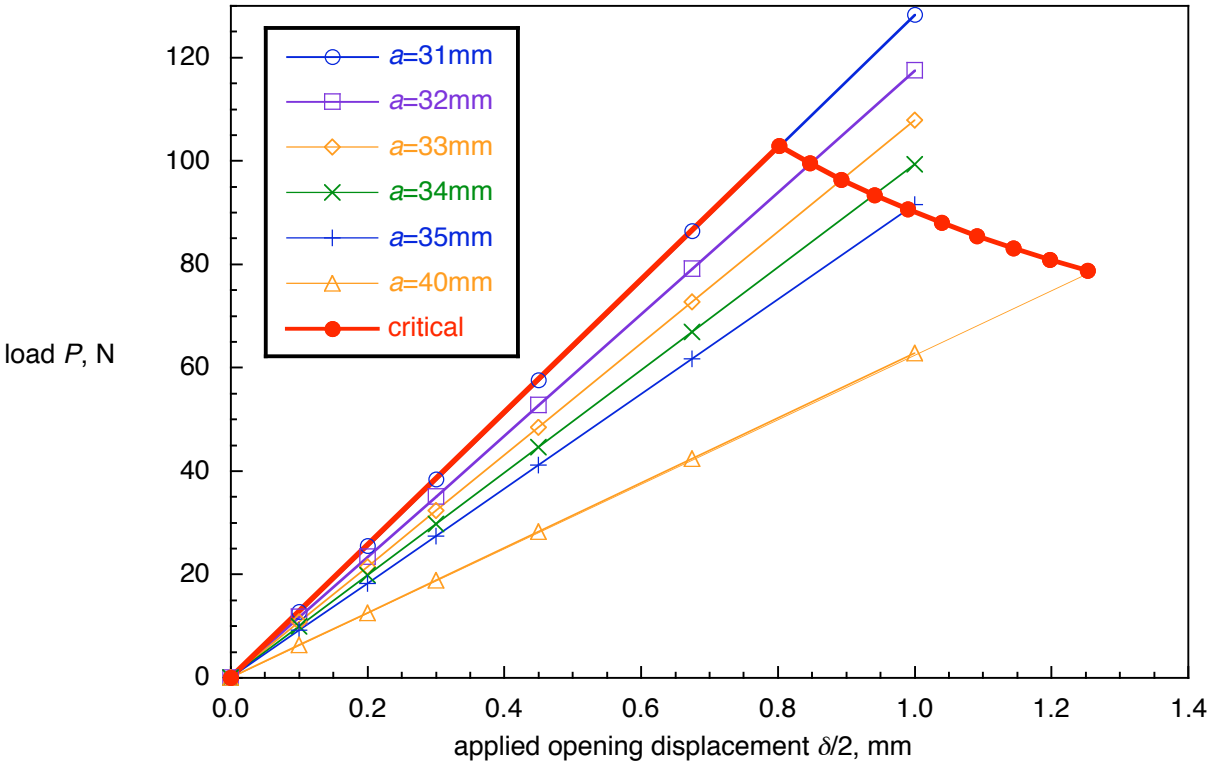

Figure 37. *Benchmark: Critical load-displacement behavior for a multidirectional DCB specimen.*

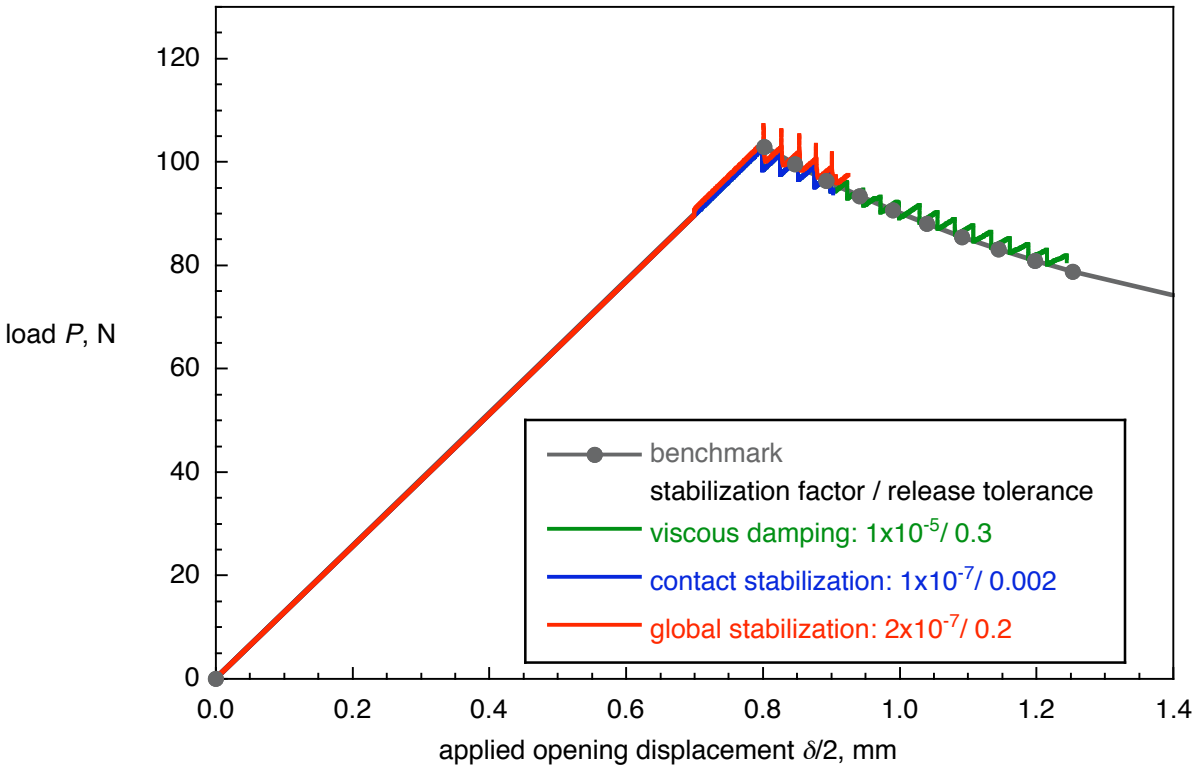

Figure 38. *VCCT for ABAQUS: Computed critical load-displacement behavior for DCB specimen obtained from results with global stabilization.*

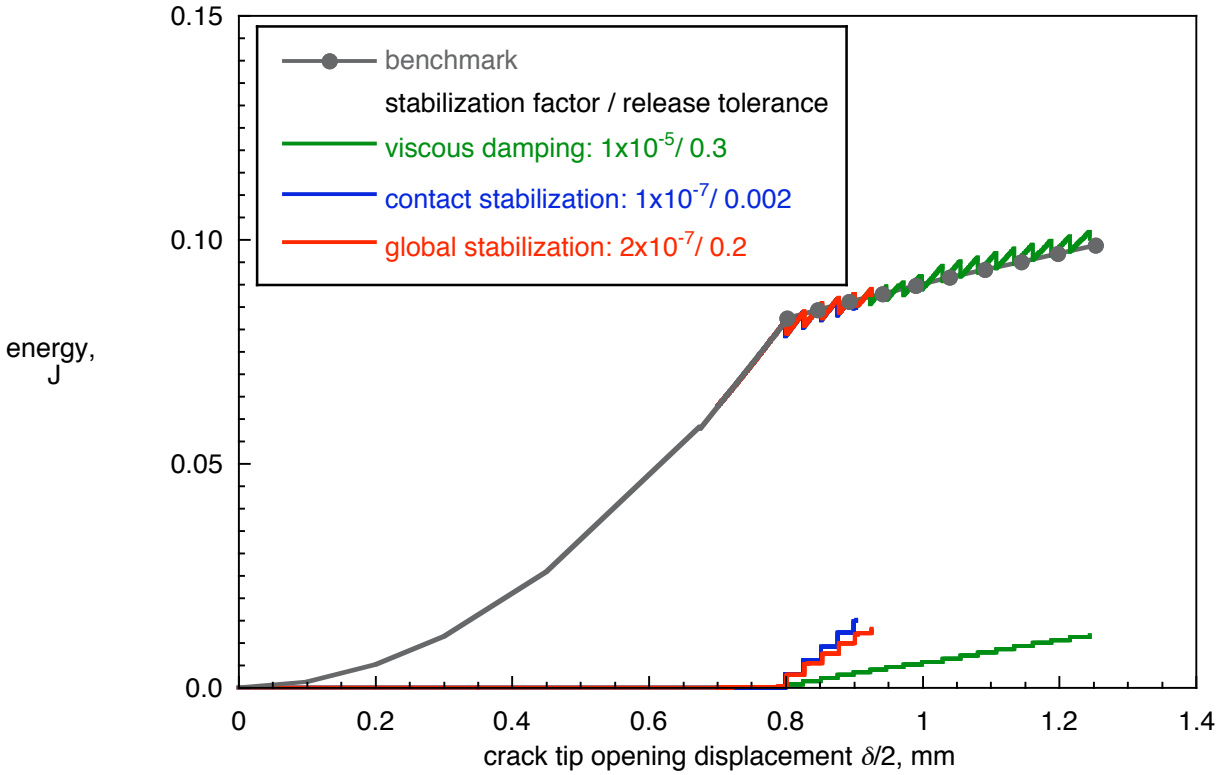

Figure 39. *Computed total strain energy and stabilization energy in the model of a multidirectional DCB specimen.*

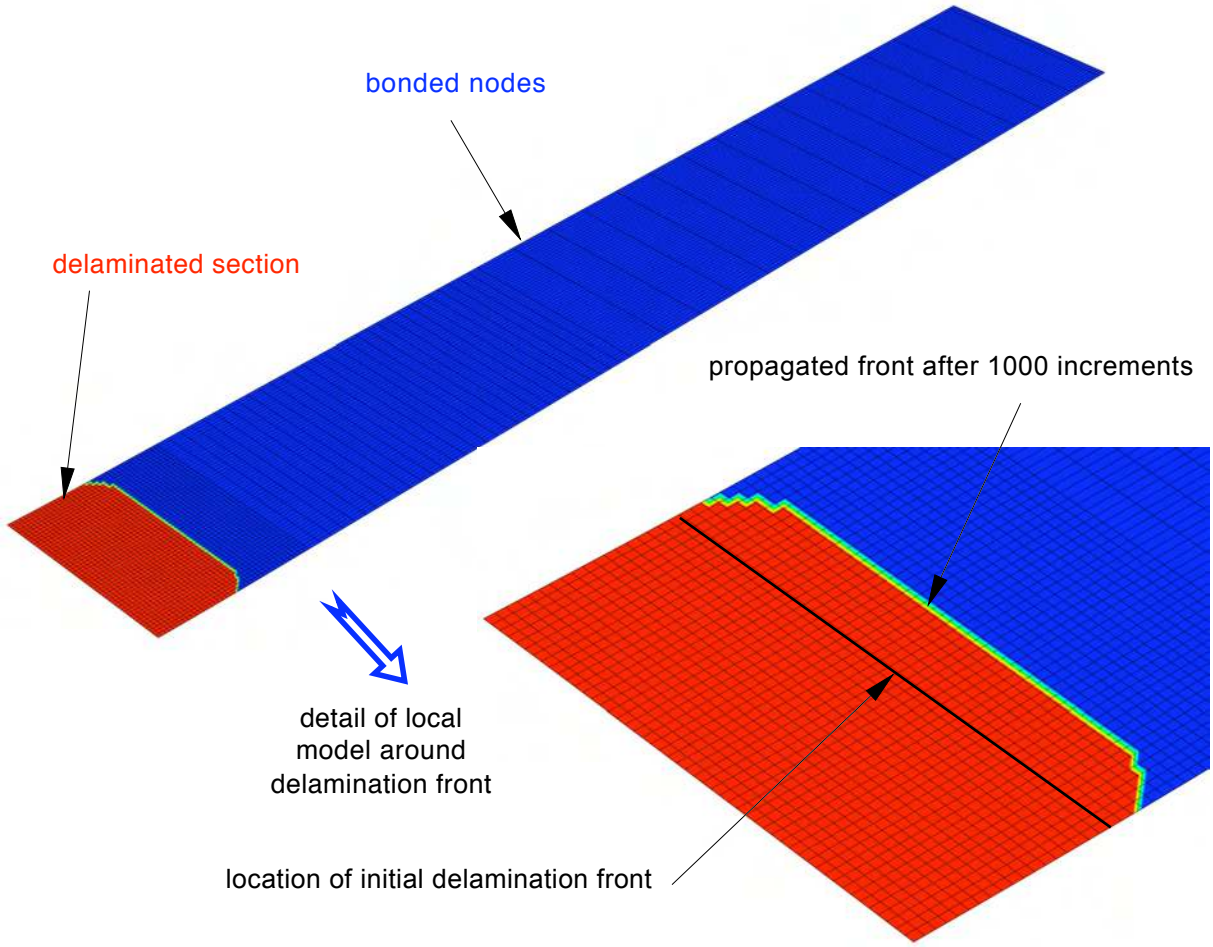

a. *Delamination front obtained with contact stabilization (Bottom surface of model in Figure 8)*

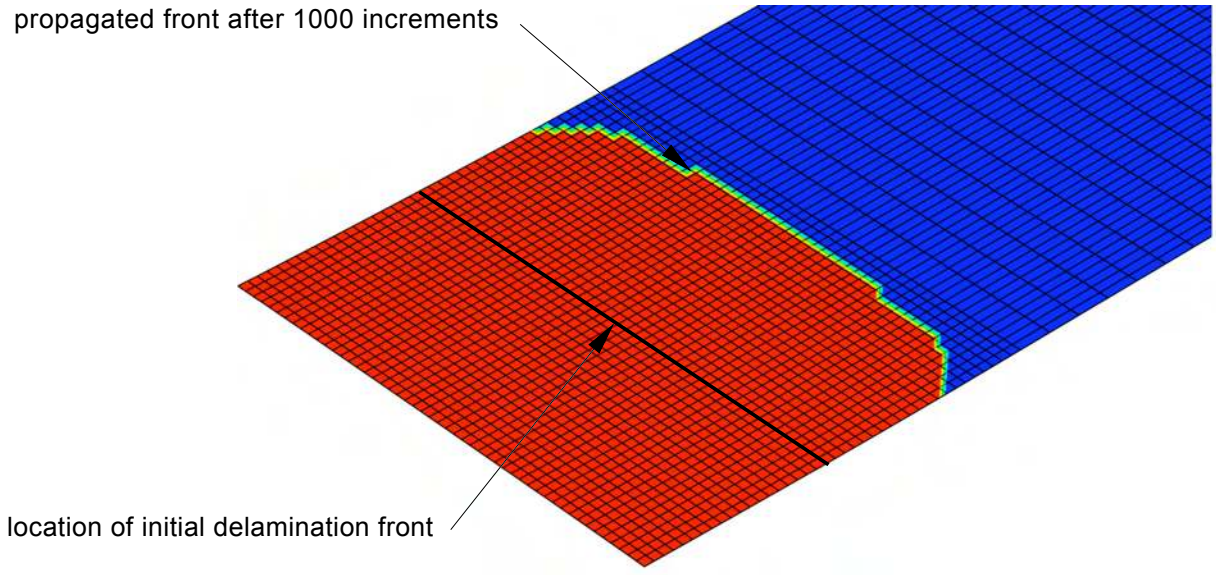

b. *Detail of delamination front obtained with viscous regularization*

Figure 40. *Delamination front shape for a multidirectional DCB specimen.*

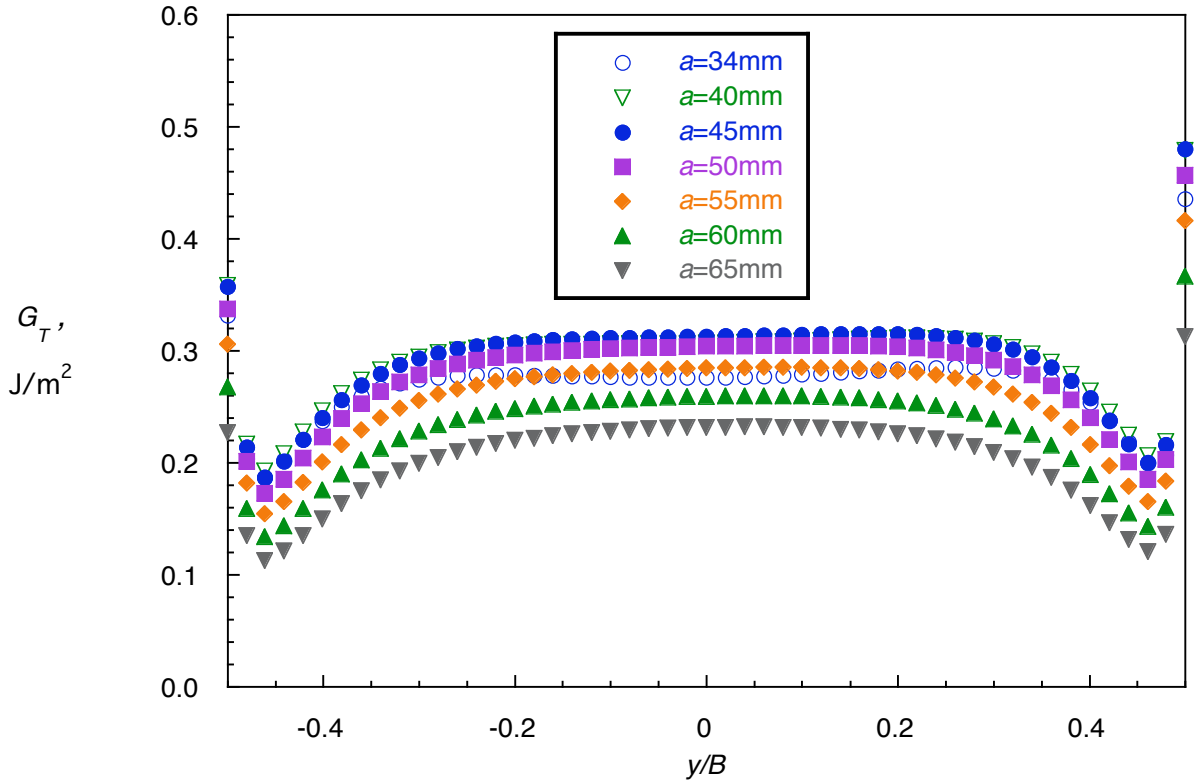

Figure 41. *Computed strain energy release rate distribution across the width of a SLB specimen.*

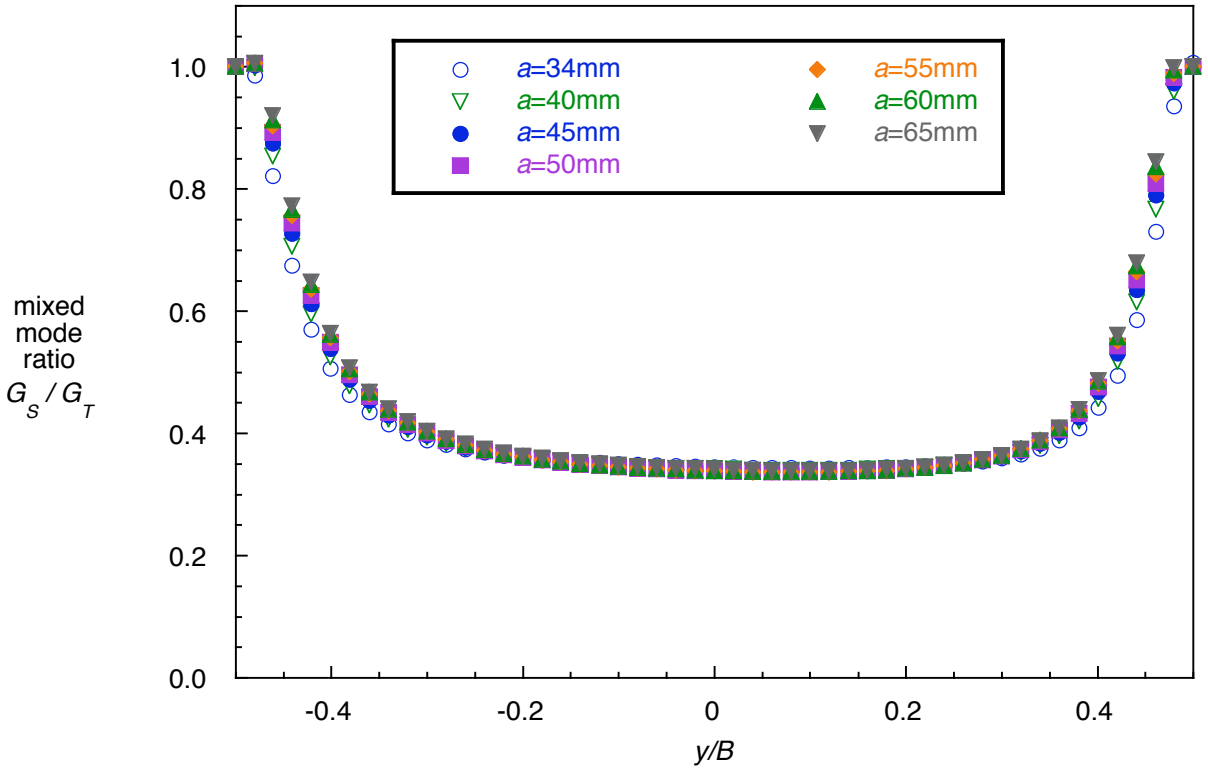

Figure 42. *Distribution of mixed-mode ratio across the width of a SLB specimen.*

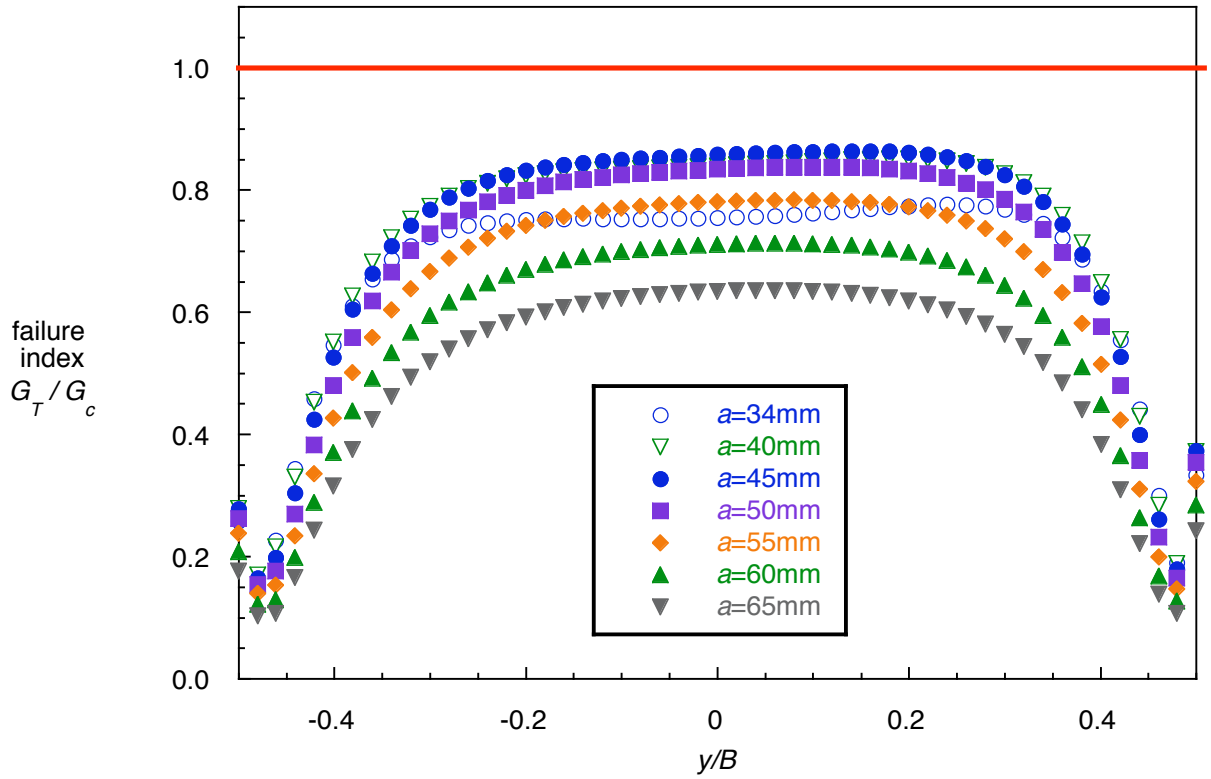

Figure 43. *Failure index distribution across the width of a SLB specimen.*

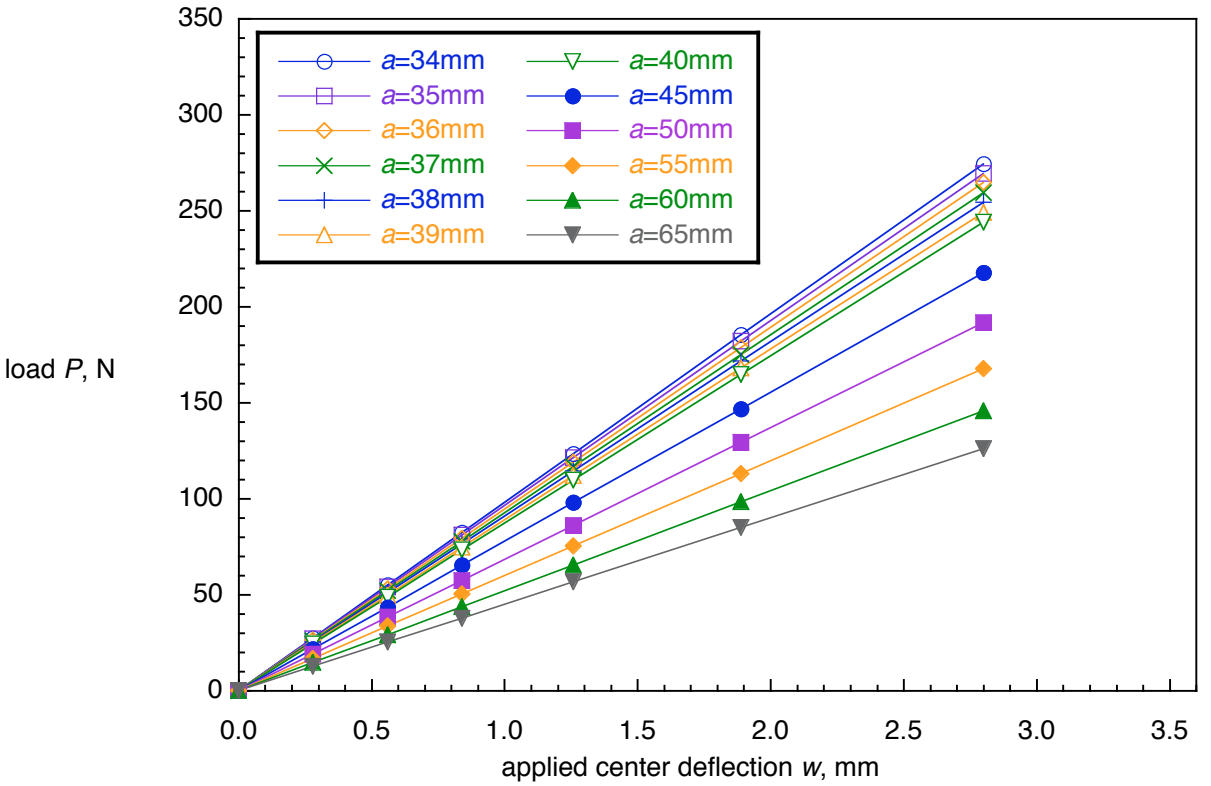

Figure 44. *Critical load-displacement behavior for SLB specimen.*

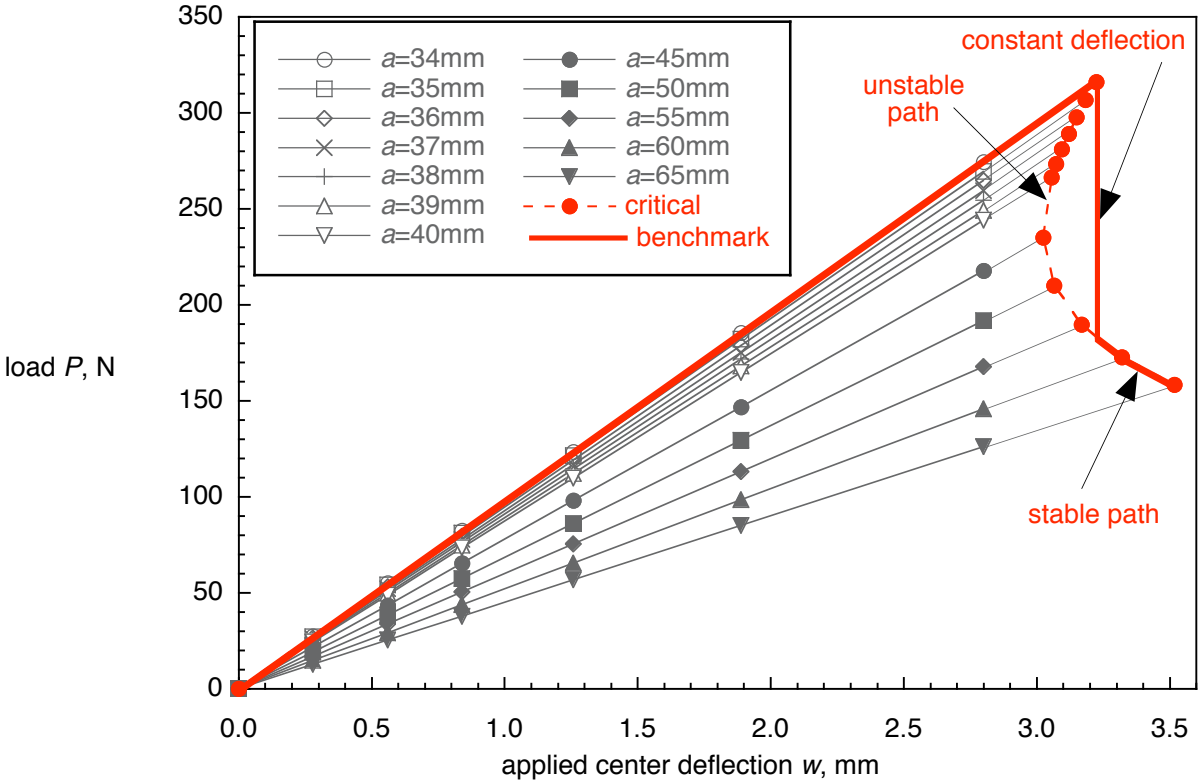

Figure 45. *Critical load-displacement behavior for SLB specimen.*

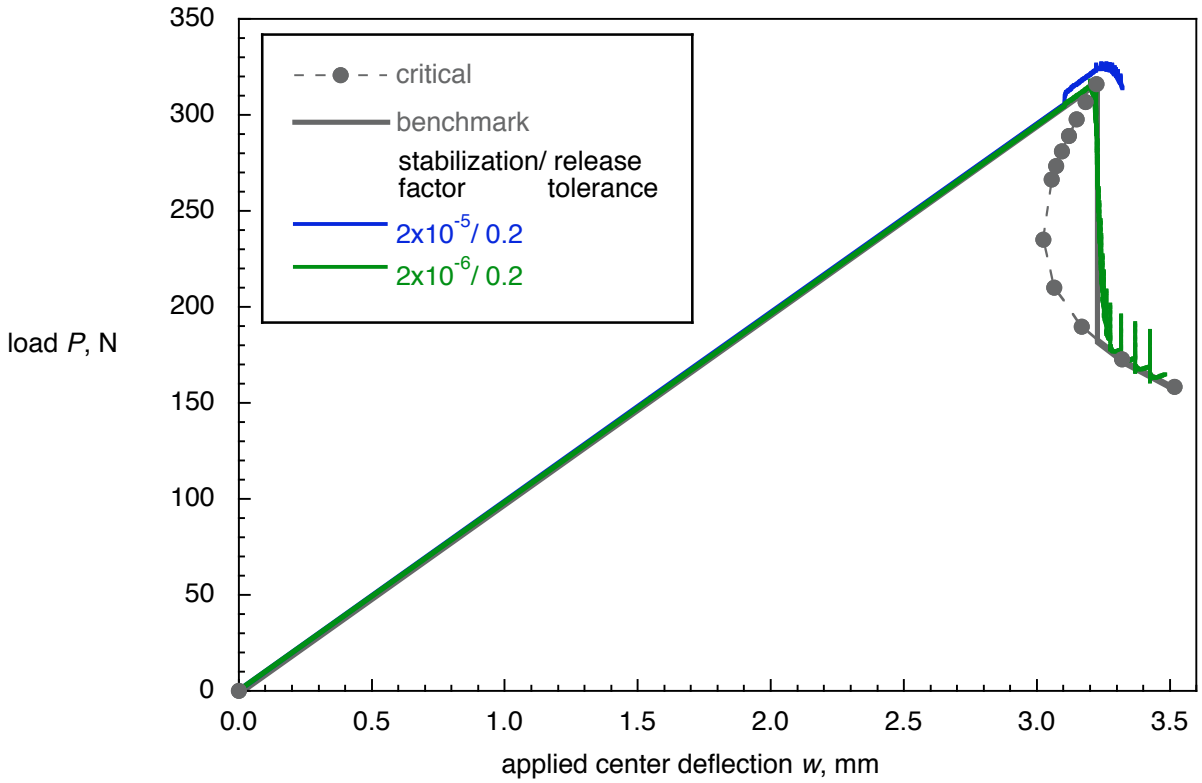

Figure 46. *Computed critical load-displacement behavior for SLB specimen obtained from results with global stabilization.*

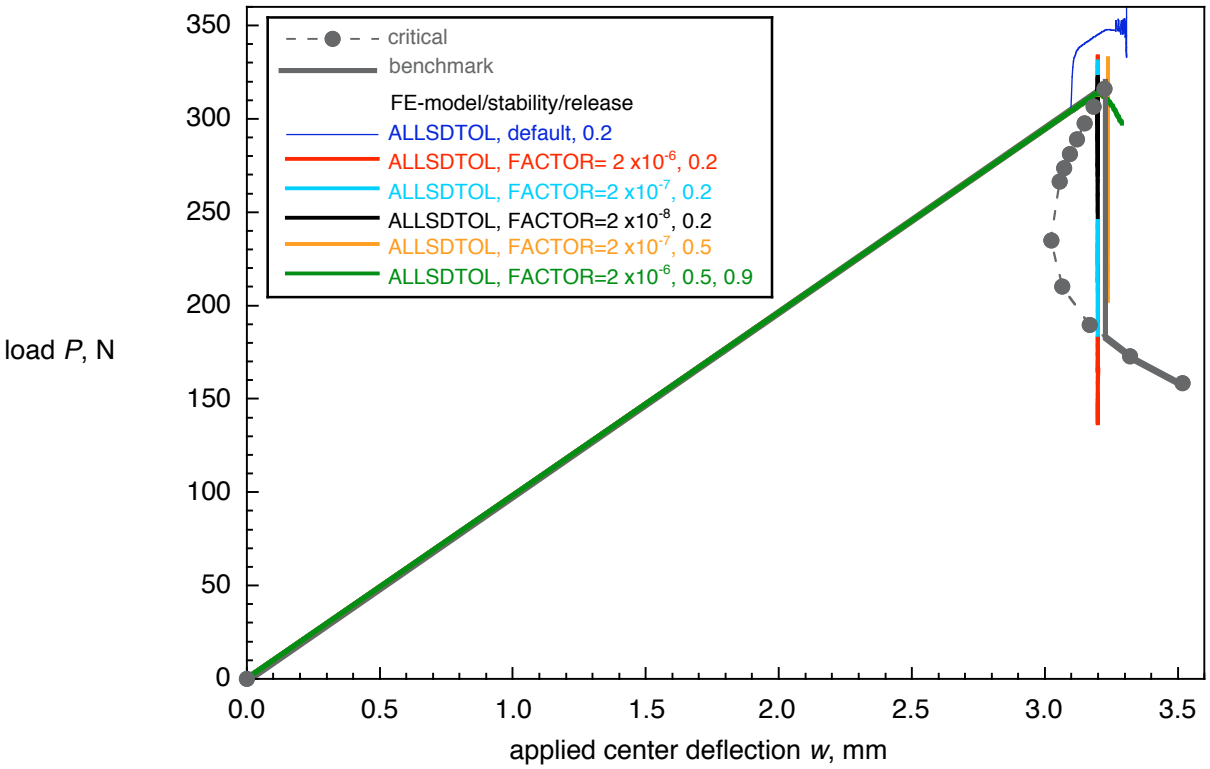

Figure 47. *Computed critical load-displacement behavior for SLB specimen obtained from results with automatic global stabilization.*

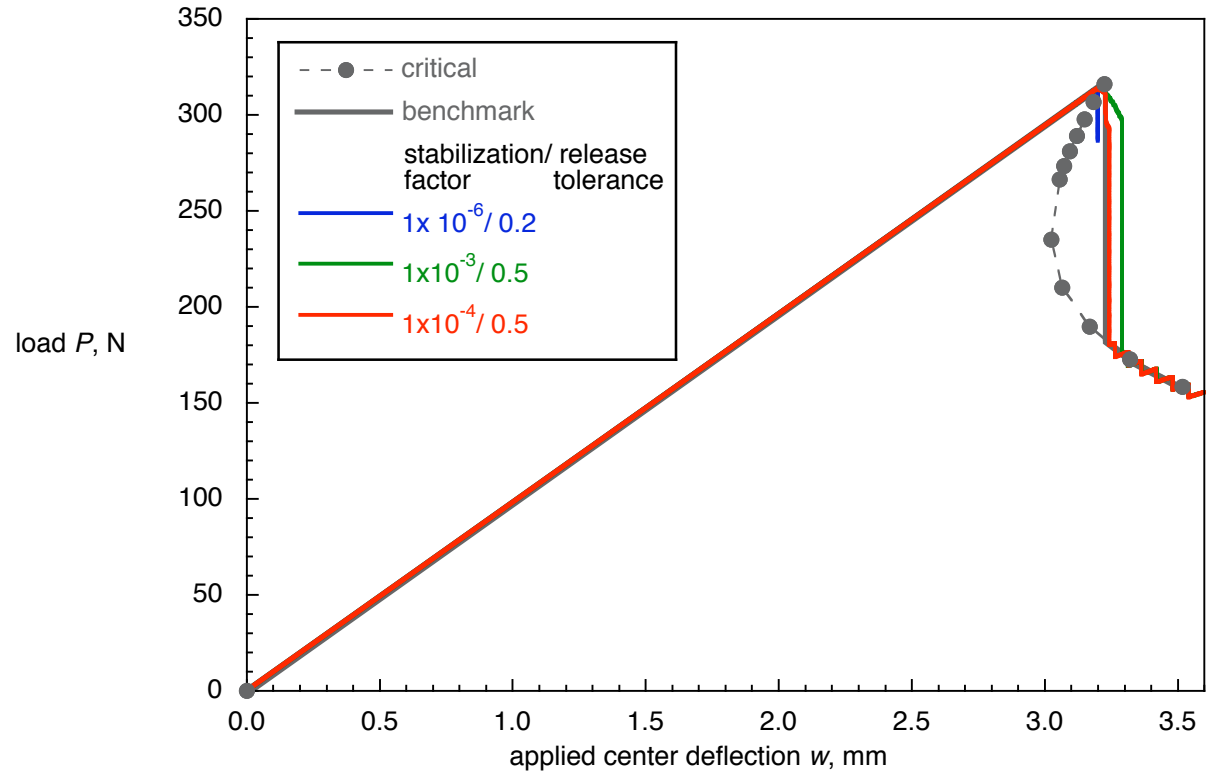

Figure 48. *Computed critical load-displacement behavior for SLB specimen obtained from results with contact stabilization.*

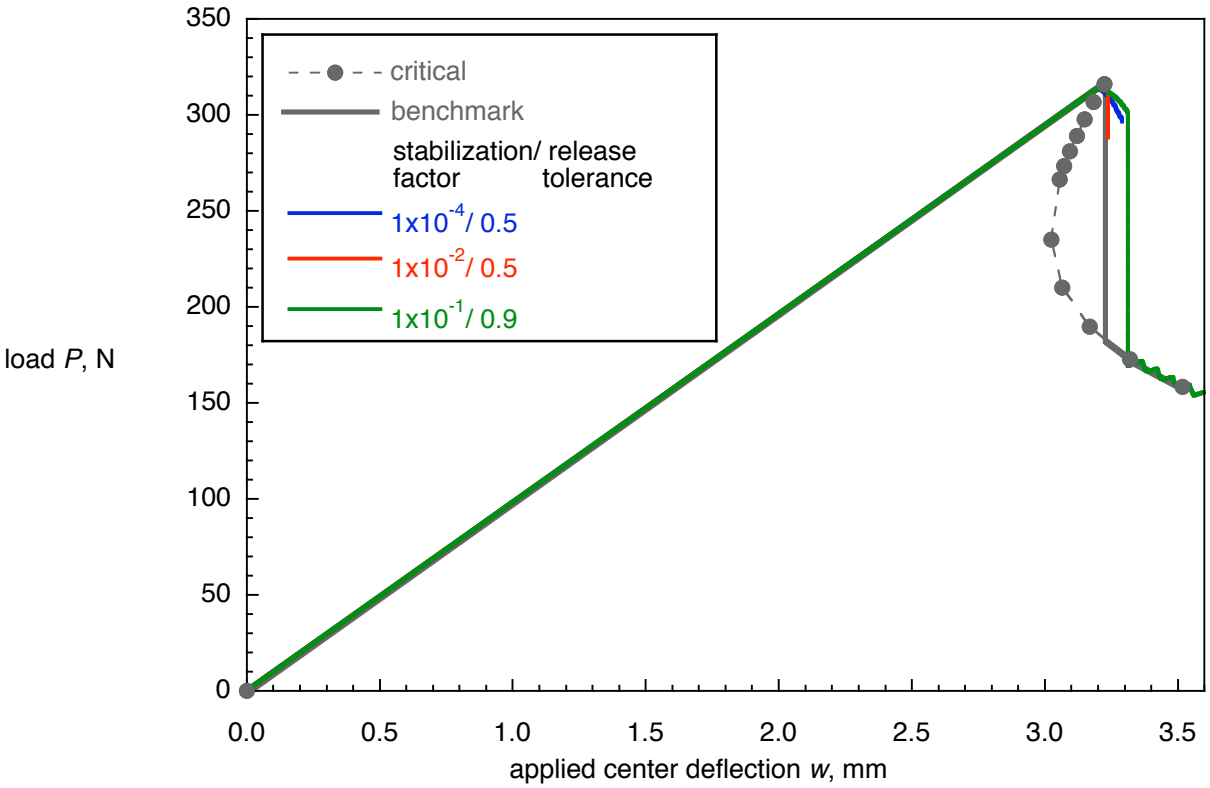

Figure 49. *Computed critical load-displacement behavior for SLB specimen obtained from results with viscous regularization.*

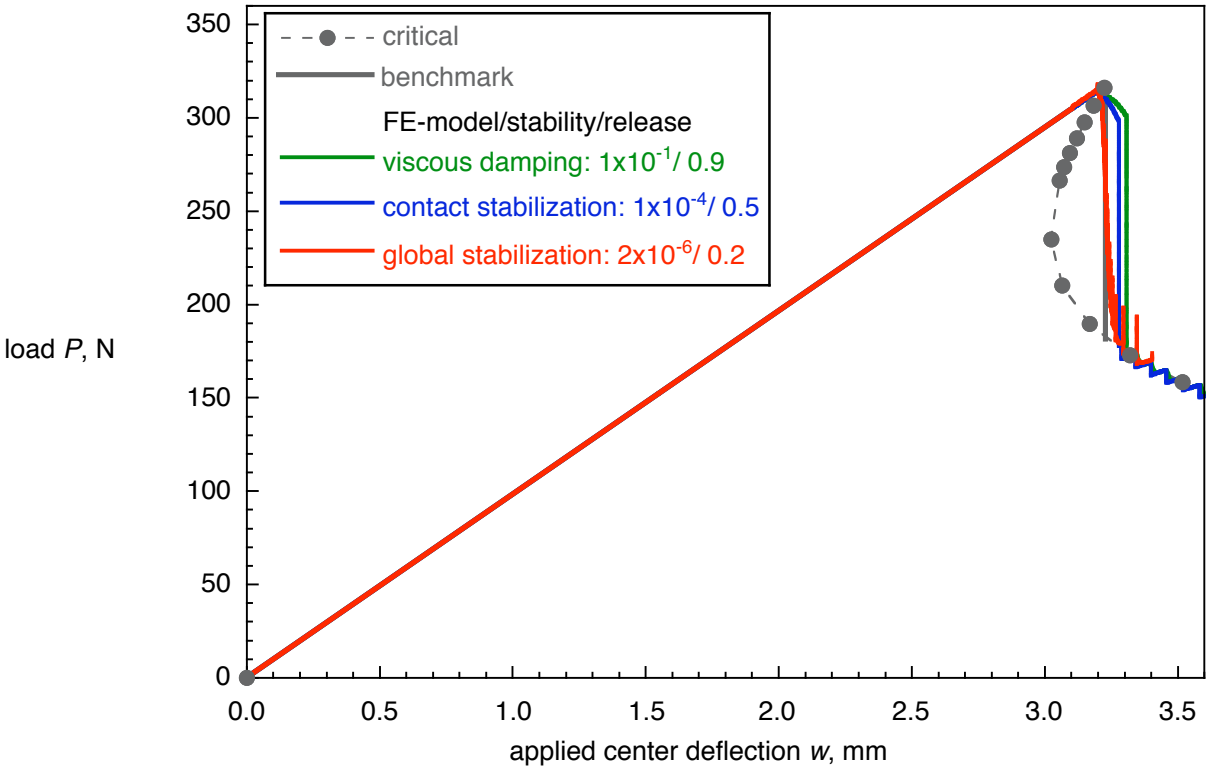

Figure 50. *Computed critical load-displacement behavior for SLB specimen obtained from results with stabilization.*

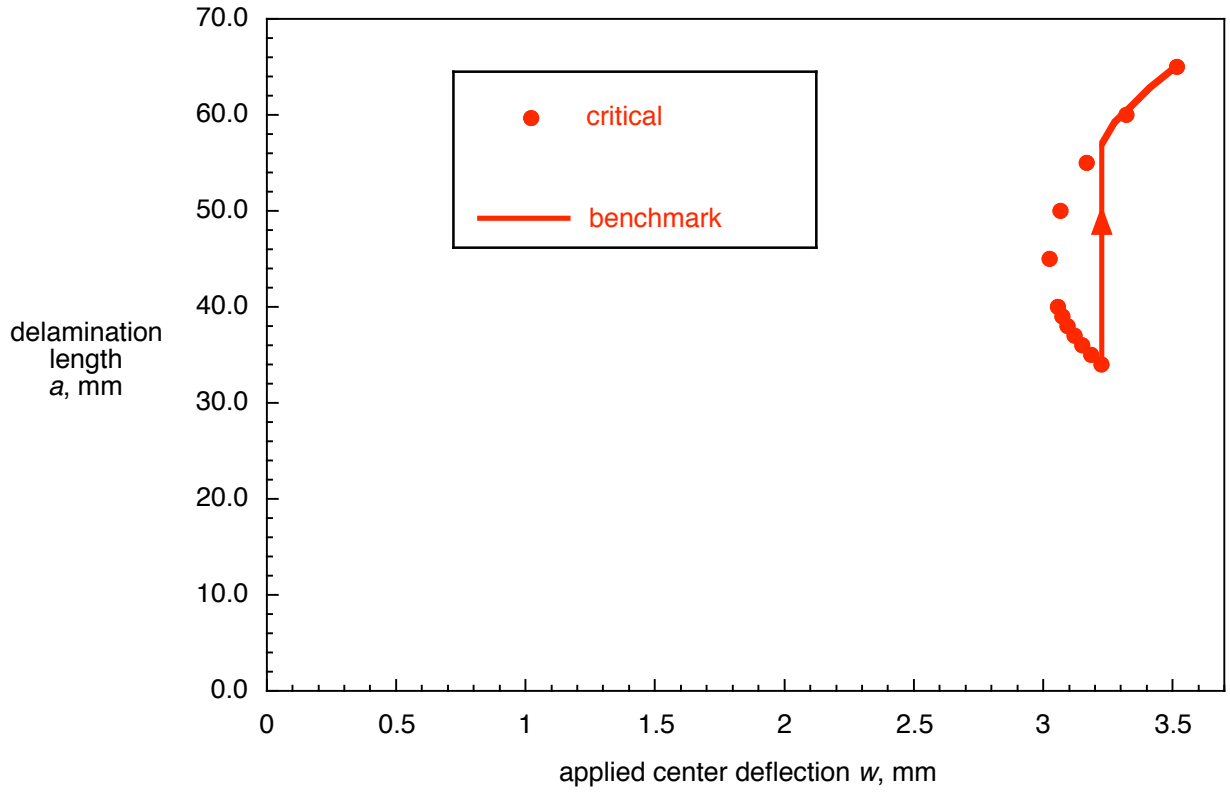

Figure 51. *Critical delamination length-displacement behavior for SLB specimen.*

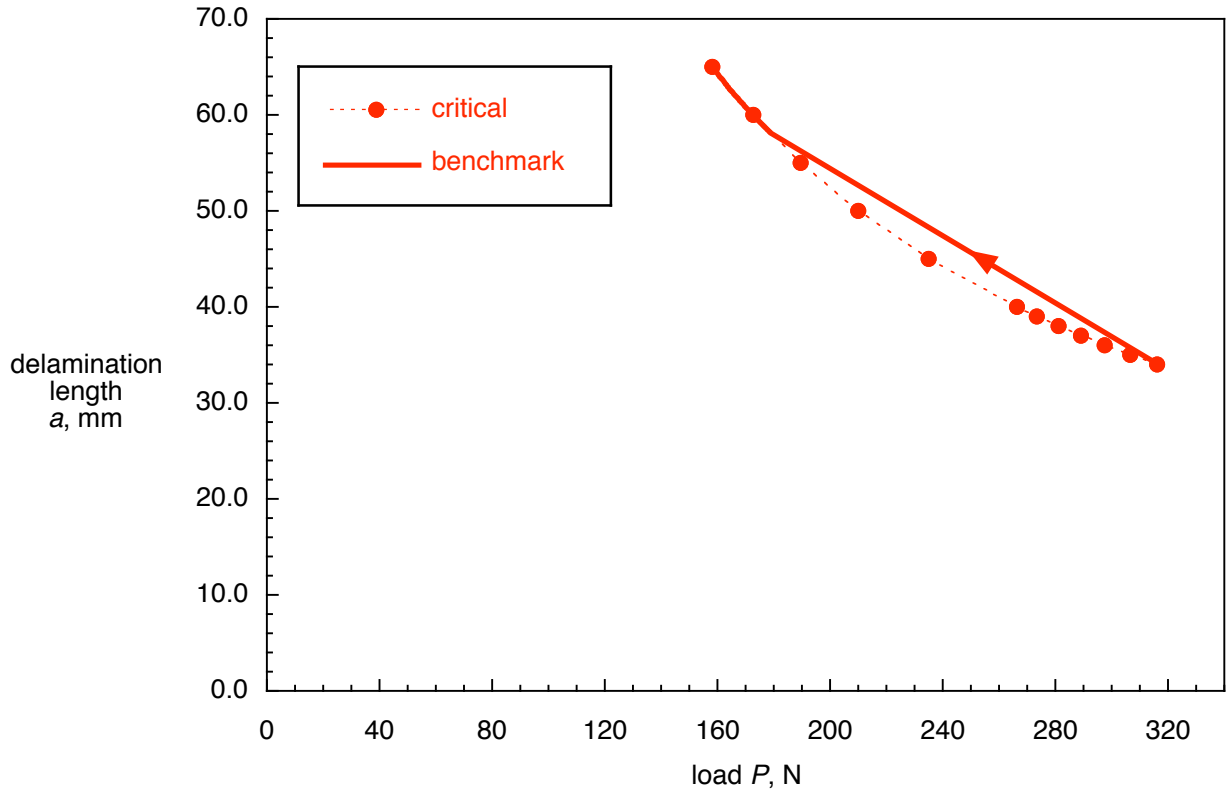

Figure 52. *Computed critical delamination length-load behavior for SLB specimen.*

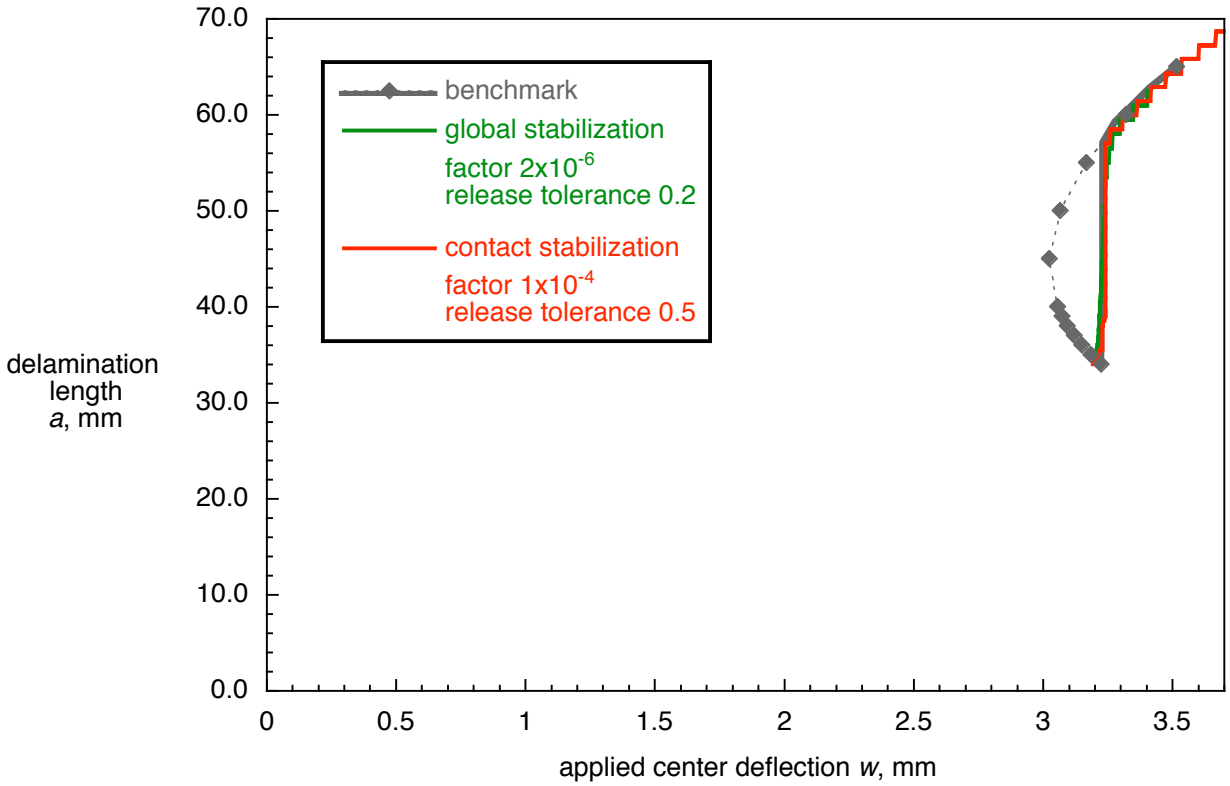

Figure 53. *Computed critical delamination length-displacement behavior for SLB specimen.*

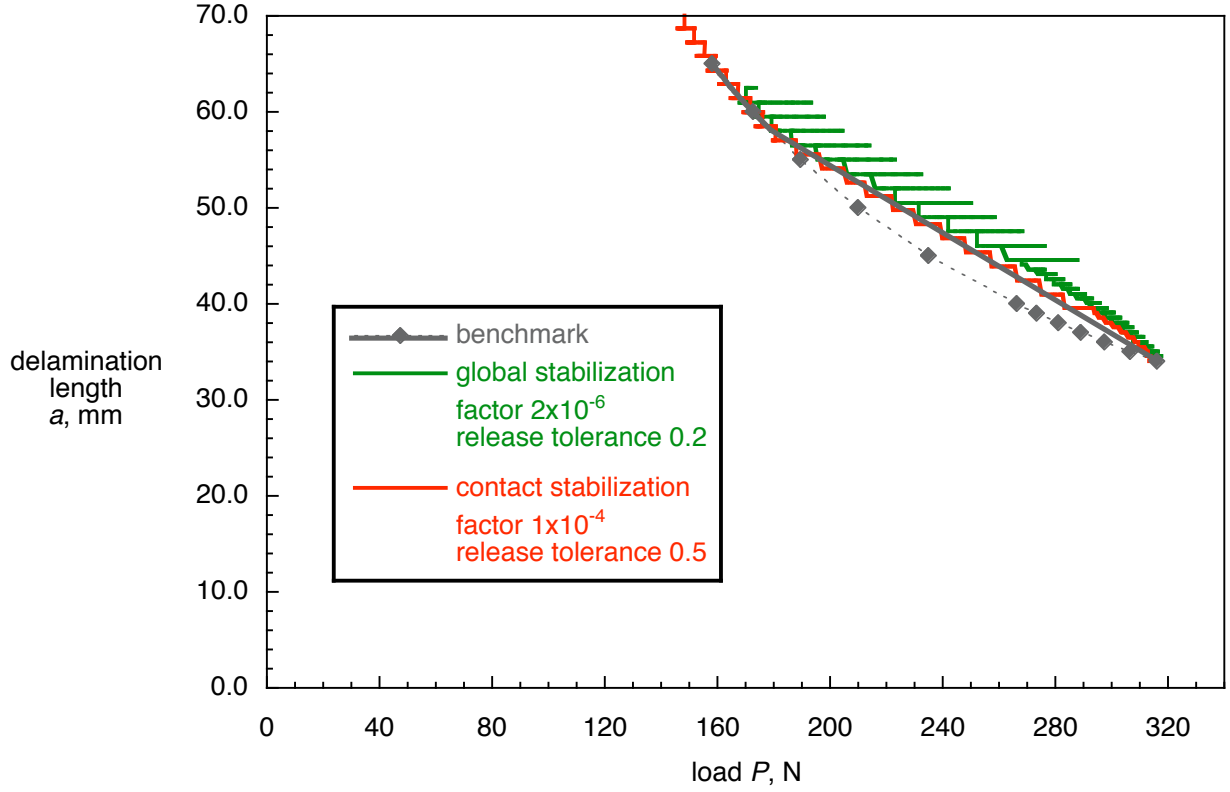

Figure 54. *Computed critical delamination length-displacement behavior for SLB specimen.*

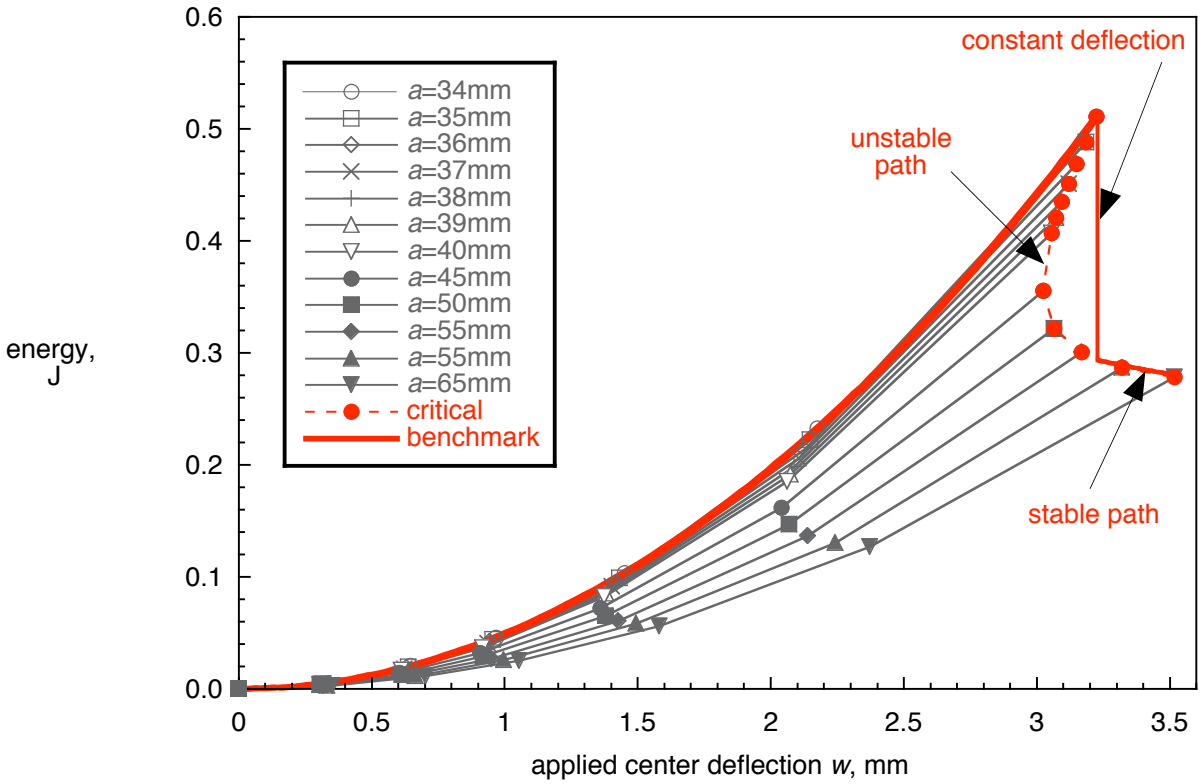

Figure 55. *Calculated total strain energy in the model of a SLB specimen (model in Figure 9).*

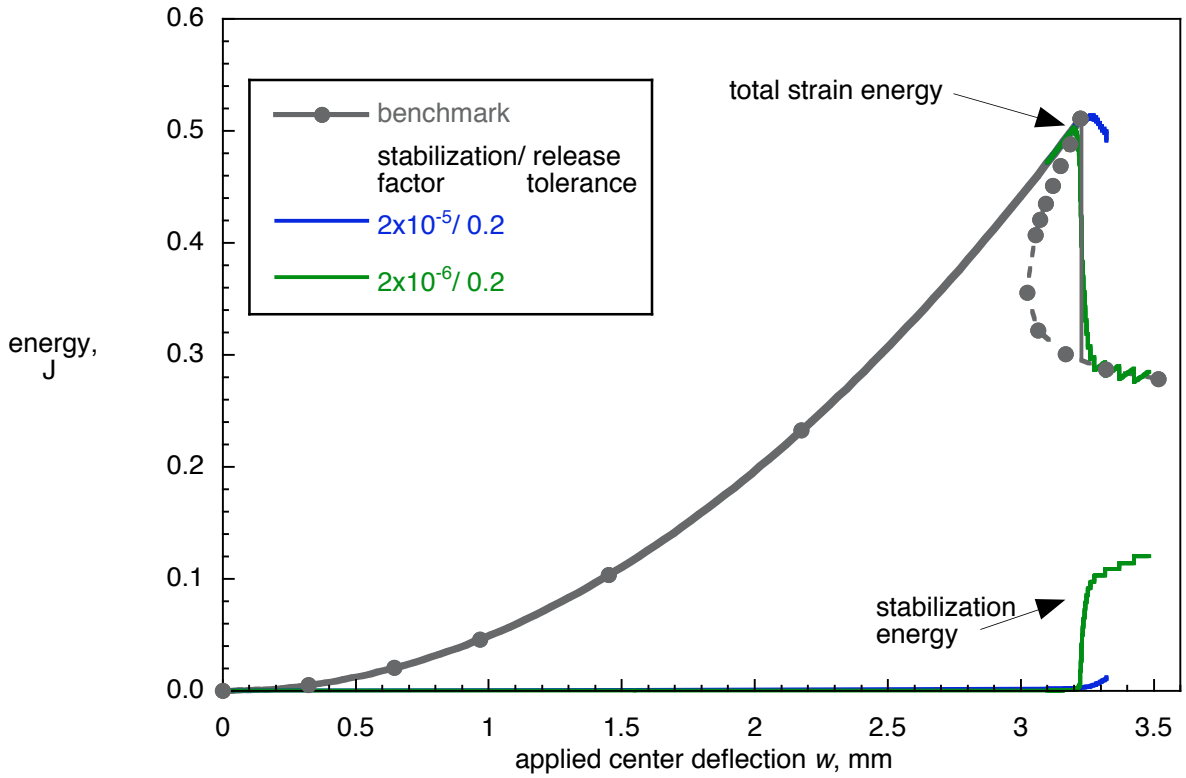

Figure 56. *Computed total strain energy and stabilization energy in the model of a SLB specimen obtained from results with global stabilization.*

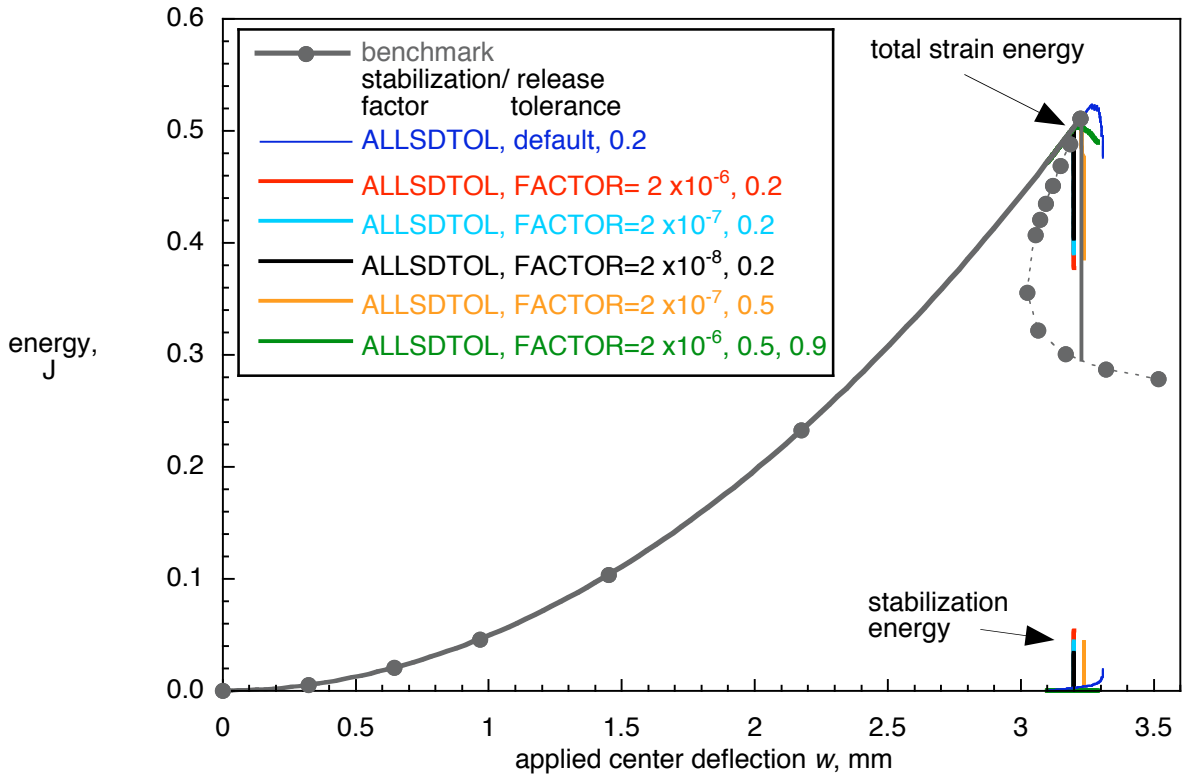

Figure 57. *Computed total strain energy and stabilization energy in the model of a SLB specimen obtained from results with automatic stabilization.*

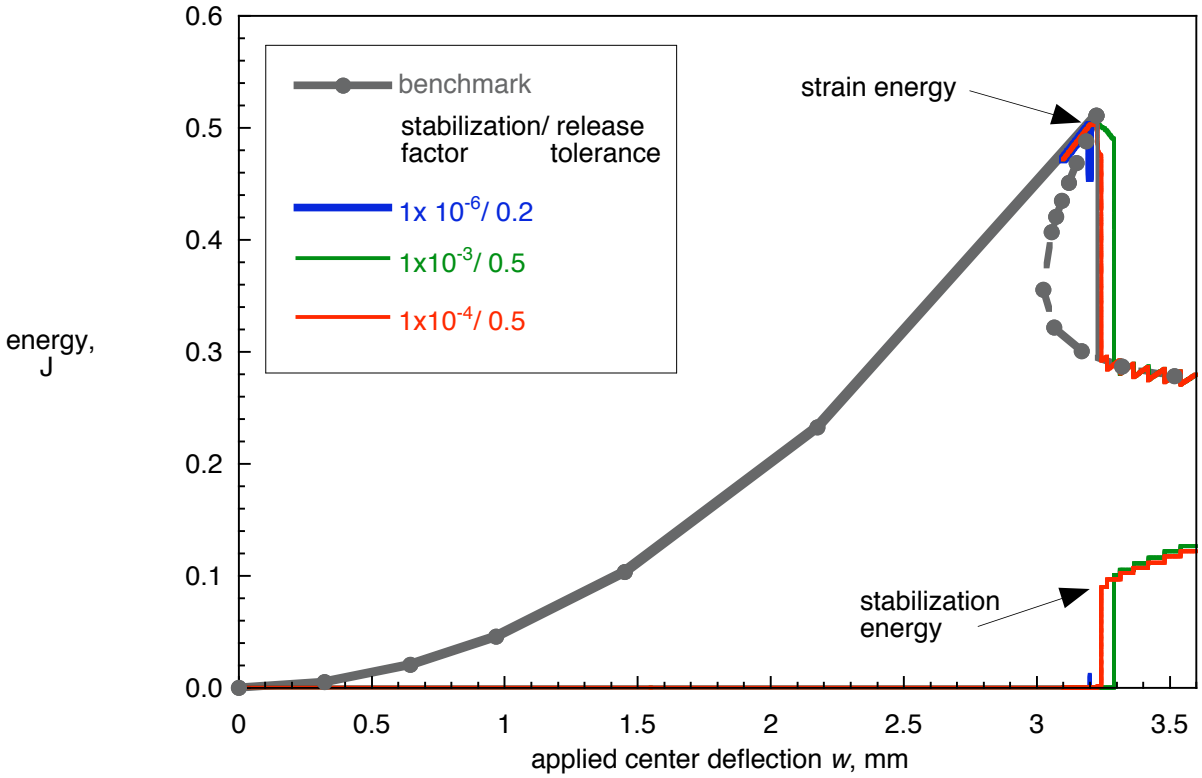

Figure 58. *Computed total strain energy and stabilization energy in the model of a SLB specimen obtained from results with contact stabilization.*

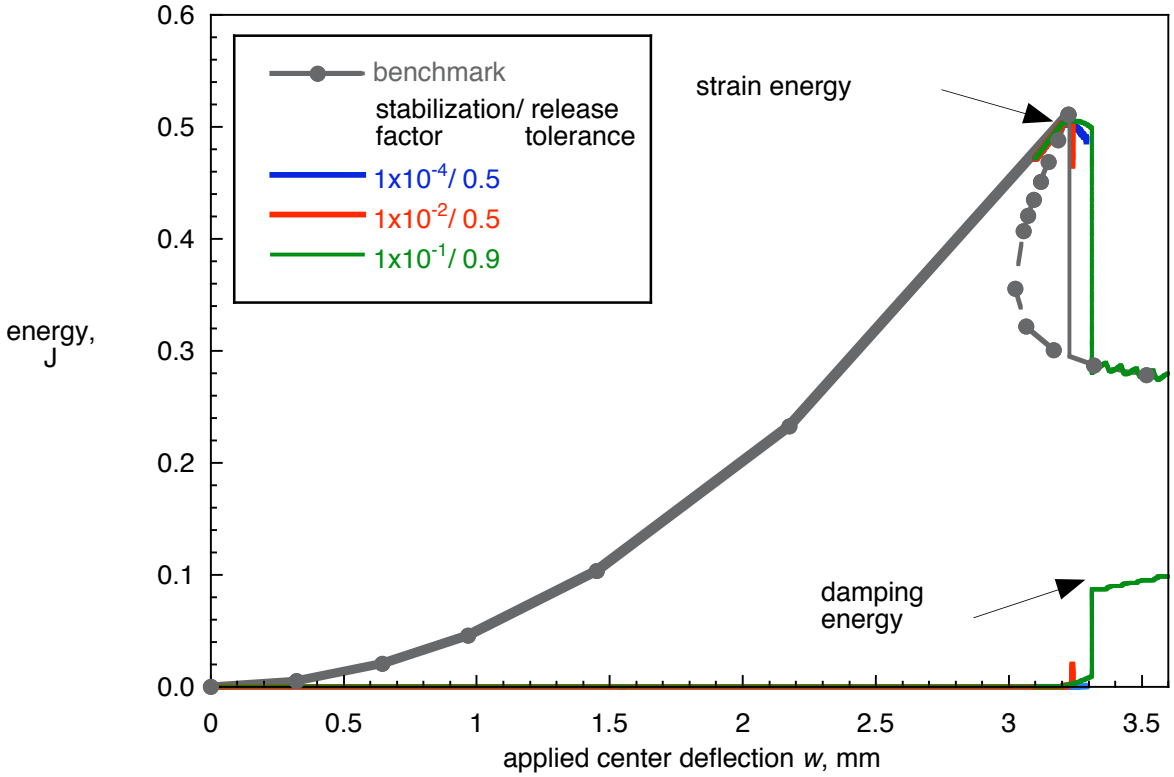

Figure 59. *Computed total strain energy and stabilization energy in the model of a SLB specimen obtained from results with viscous regularization.*

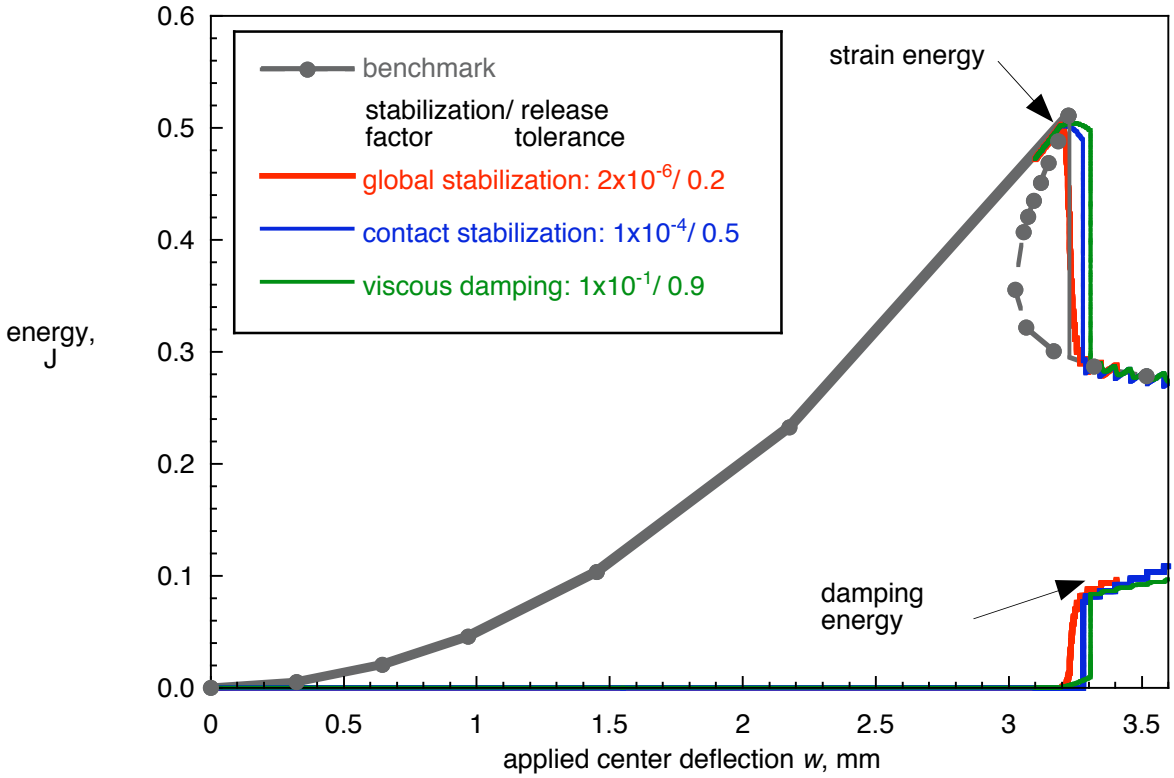

Figure 60. *Computed total strain energy and stabilization energy in the model of a SLB specimen obtained from results with stabilization.*

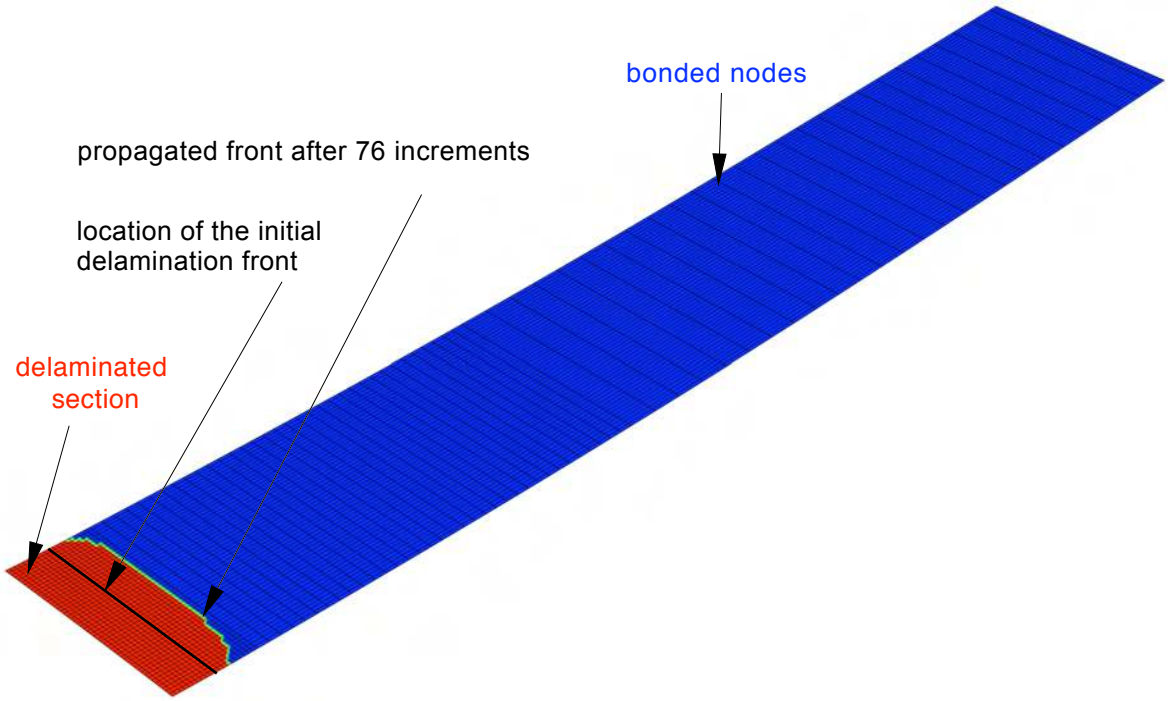

a. *Delamination front obtained with contact stabilization (increment 76)*

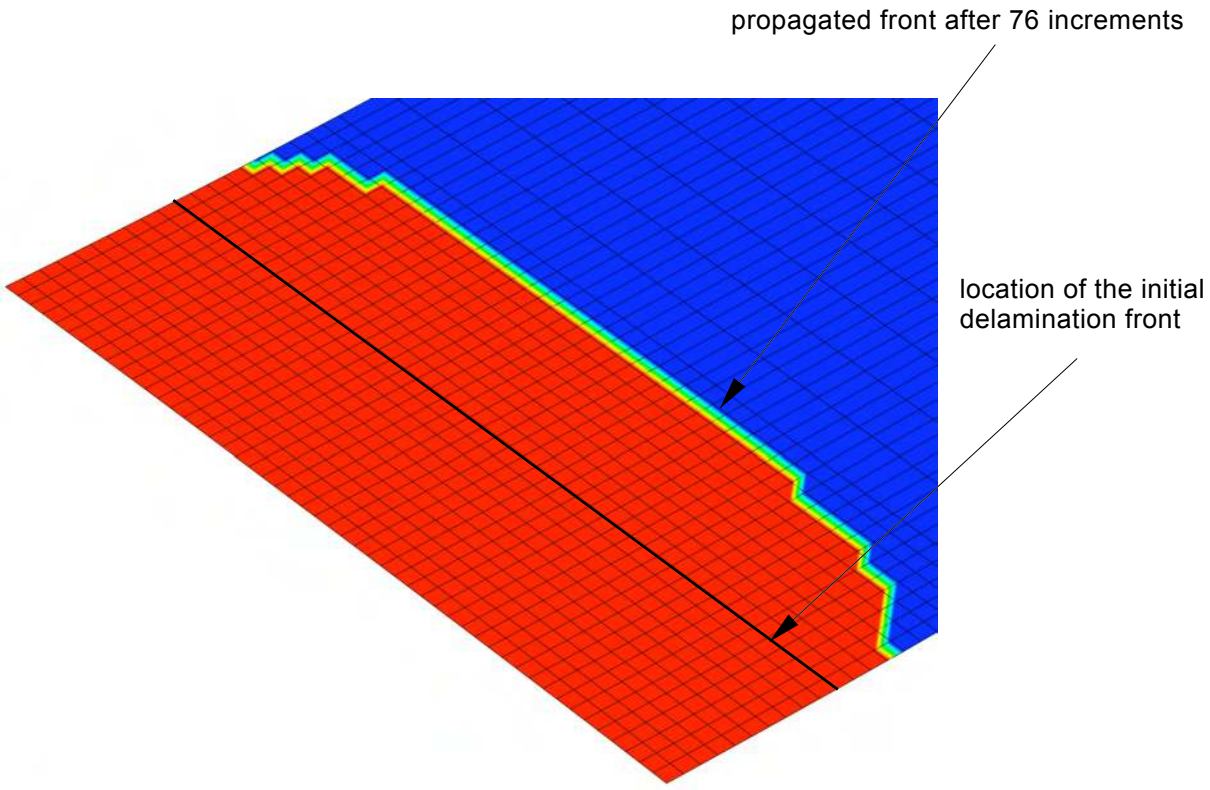

b. *Detail of delamination front obtained with contact stabilization (increment 76)*

Figure 61. *Computed delamination front shape for a SLB specimen (model in Figure 9).*

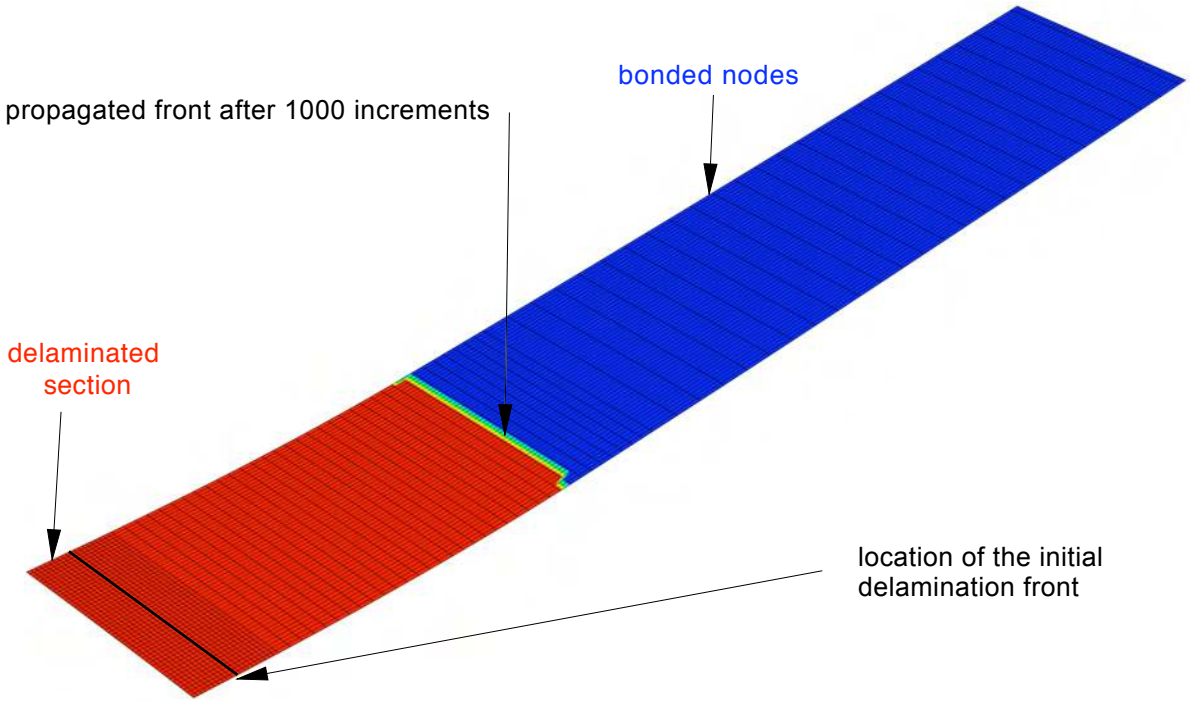

a. *Delamination front obtained with contact stabilization (increment 1000)*

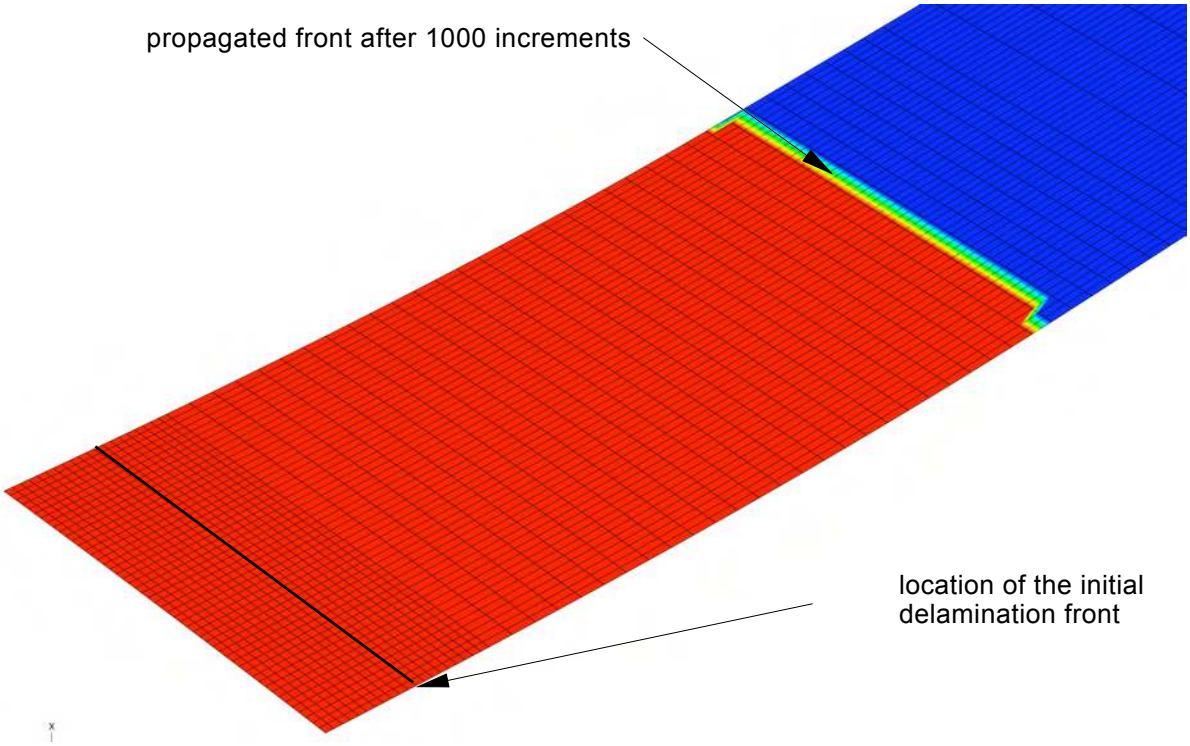

b. *Detail of delamination front obtained with contact stabilization (increment 1000)*

Figure 62. *Computed delamination front shape for a SLB specimen (model in Figure 9).*

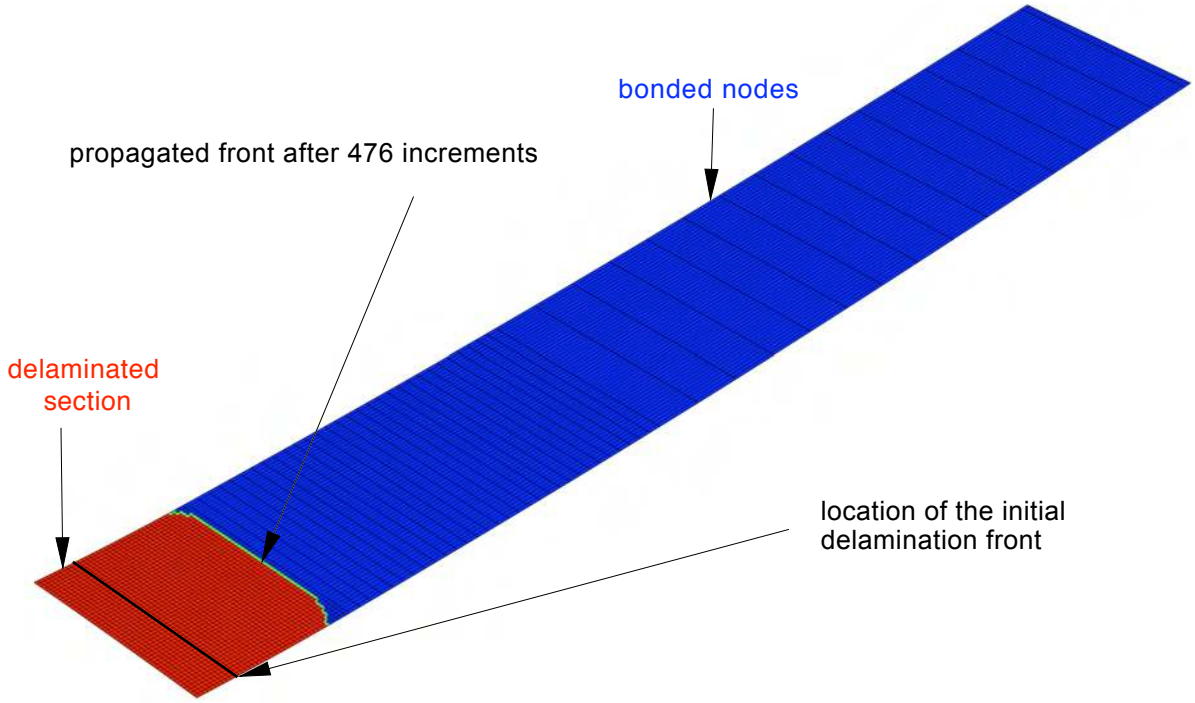

a. *Delamination front obtained with global stabilization (increment 476)*

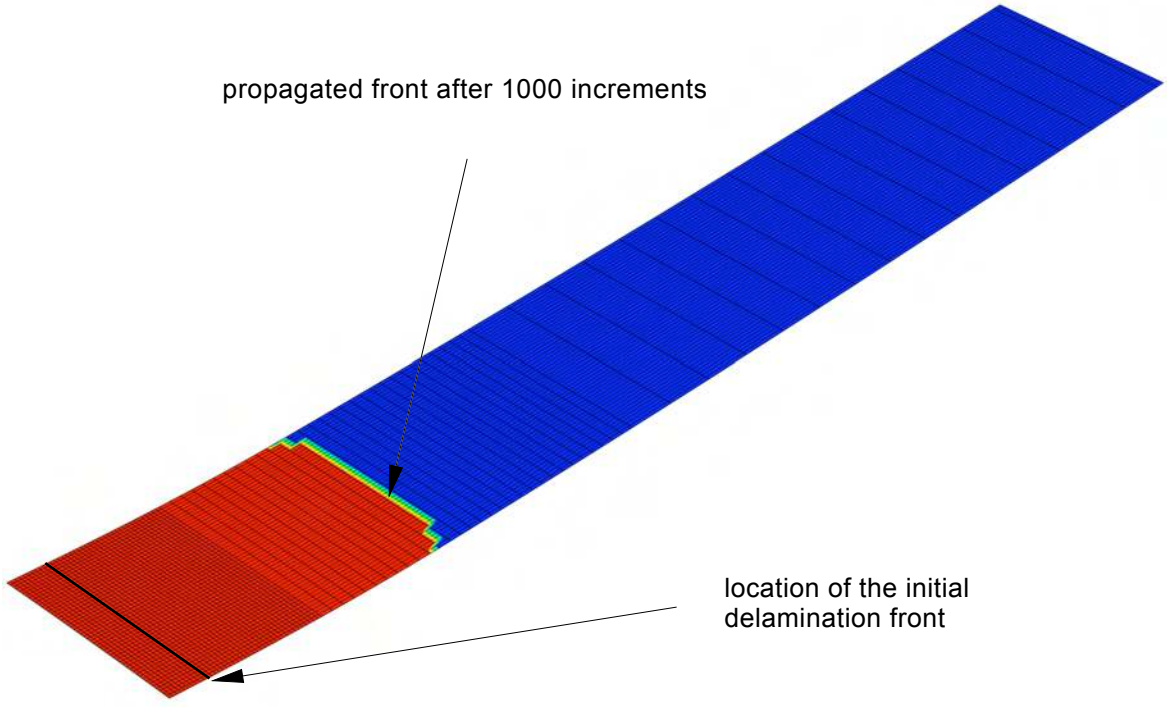

b. *Detail of delamination front obtained with global stabilization (increment 1000)*

Figure 63. *Computed delamination front shape for a SLB specimen (model in Figure 10).*

REPORT DOCUMENTATION PAGE

Form Approved
OMB No. 0704-0188

1. REPORT DATE *(DD-MM-YYYY)*	2. REPORT TYPE	3. DATES COVERED *(From - To)*
01- 04 - 2008	Technical Memorandum	

4. TITLE AND SUBTITLE
An Approach to Assess Delamination Propagation Simulation Capabilities in Commercial Finite Element Codes

5a. CONTRACT NUMBER

5b. GRANT NUMBER

5c. PROGRAM ELEMENT NUMBER

6. AUTHOR(S)
Krueger, Ronald

5d. PROJECT NUMBER

5e. TASK NUMBER

5f. WORK UNIT NUMBER
698259.02.07.07.03.03

7. PERFORMING ORGANIZATION NAME(S) AND ADDRESS(ES)
NASA Langley Research Center
Hampton, VA 23681-2199

8. PERFORMING ORGANIZATION REPORT NUMBER
L-19452

9. SPONSORING/MONITORING AGENCY NAME(S) AND ADDRESS(ES)
National Aeronautics and Space Administration
Washington, DC 20546-0001

10. SPONSOR/MONITOR'S ACRONYM(S)
NASA

11. SPONSOR/MONITOR'S REPORT NUMBER(S)
NASA/TM-2008-215123

12. DISTRIBUTION/AVAILABILITY STATEMENT
Unclassified - Unlimited
Subject Category 24
Availability: NASA CASI (301) 621-0390

13. SUPPLEMENTARY NOTES
Krueger: National Institute of Aerospace, Hampton, VA
An electronic version can be found at http://ntrs.nasa.gov

14. ABSTRACT

An approach for assessing the delamination propagation simulation capabilities in commercial finite element codes is presented and demonstrated. For this investigation, the Double Cantilever Beam (DCB) specimen and the Single Leg Bending (SLB) specimen were chosen for full three-dimensional finite element simulations. First, benchmark results were created for both specimens. Second, starting from an initially straight front, the delamination was allowed to propagate. The load-displacement relationship and the total strain energy obtained from the propagation analysis results and the benchmark results were compared and good agreements could be achieved by selecting the appropriate input parameters. Selecting the appropriate input parameters, however, was not straightforward and often required an iterative procedure. Qualitatively, the delamination front computed for the DCB specimen did not take the shape of a curved front as expected. However, the analysis of the SLB specimen yielded a curved front as was expected from the distribution of the energy release rate and the failure index across the width of the specimen. Overall, the results are encouraging but further assessment on a structural level is required.

15. SUBJECT TERMS
Composites; Delamination propagation; Finite element analysis; Fracture mechanics; Virtual crack closure technique

16. SECURITY CLASSIFICATION OF:			17. LIMITATION OF ABSTRACT	18. NUMBER OF PAGES	19a. NAME OF RESPONSIBLE PERSON
a. REPORT	b. ABSTRACT	c. THIS PAGE			STI Help Desk (email: help@sti.nasa.gov)
					19b. TELEPHONE NUMBER *(Include area code)*
U	U	U	UU	71	(301) 621-0390